Technische Universität München
TUM School of Natural Sciences

Advances in grating fabrication and data processing for X-ray grating interferometry

Simon Johannes Pinzek

Vollständiger Abdruck der von der TUM School of Natural Sciences der Technischen Universität München zur Erlangung des akademischen Grades eines

Doktors der Naturwissenschaften (Dr. rer. nat.)

genehmigten Dissertation.

Vorsitzender: Prof. Dr. Michael Knap

Prüfer*innen der Dissertation: 1. Prof. Dr. Franz Pfeiffer

2. Prof. Dr. Oliver Hayden

Die Dissertation wurde am 22.06.2023 bei der Technischen Universität München eingereicht und durch die TUM School of Natural Sciences am 31.10.2023 angenommen.

Abstract

Conventional X-ray imaging takes advantage of the fact that X-rays are absorbed to different extents in different materials. In addition to this so-called absorption contrast, methods were developed to transfer the phase contrast known from microscopy with visible light to X-ray imaging. In the past two decades, these efforts have been intensified, among other methods, with the so-called X-ray grating interferometry. In addition to phase contrast, which is sensitive to phase shifts, this method also provides the dark field signal, which is sensitive to small-angle scattering. The quality of the images obtained with an X-ray grating interferometer depends strongly on the used absorption and phase-shifting X-ray gratings. Especially the fabrication of the absorption gratings is still a challenge since they require large aspect ratios. In order to meet these requirements, various manufacturing processes have been established: on the one hand, processes based on silicon etching, on the other hand, processes based on deep X-ray lithography performed at synchrotron sources.

The results of this work are divided into two parts: The first part addresses the further development of the fabrication of X-ray absorption gratings. For this purpose, the filling process of silicon-etched grating structures with absorbing particles was improved. On the one hand, tungsten particles of different sizes were mixed to increase the particle density in the grating structures. On the other hand, it was shown that the fabrication of large gratings is feasible with a centrifugation process used to densify the particles. Thus, particle gratings were produced that are larger and comparable in their absorption properties to conventional gratings produced by X-ray lithography. In addition, the deep X-ray lithographic process was adapted in order to be performed at conventional X-ray tubes, since these are more widely available than synchrotron sources. First, suitable parameters for the exposure were determined. Then, methods were developed to produce large-area gratings. It was shown that bending the mask and substrate during exposure at conventional X-ray tubes is necessary for uniform grating structures. The second part of the results focuses on adapted data processing for grating-based X-ray interferometry setups where the intensity modulation deviates from a sinusoidal shape. To account for a variety of different intensity modulations, a piecewise-defined function consisting of zero- to second-order polynomials was introduced. This function is able to describe symmetric and asymmetric intensity modulations. Thus, sampling related artifacts caused by non-sinusoidal intensity modulations can be reduced in the processed images.

Zusammenfassung

Konventionelle Röntgenbildgebung nutzt aus, dass Röntgenstrahlung in verschiedenen Materialien unterschiedlich stark absorbiert wird. Neben diesem sogenannten Absorptionskontrast wurden bereits Mitte des 19. Jahrhunderts Methoden entwickelt um den aus der Mikroskopie mit sichtbarem Licht bekannten Phasenkontrast auf die Röntgenbildgebung zu übertragen. In den vergangen zwei Jahrzehnten wurden diese Bemühungen unter anderem verstärkt mit der sogenannten Röntgen-Gitter-Interferometrie verfolgt. Diese liefert neben dem auf Phasenschübe sensitiven Phasenkontrast auch das auf klein-Winkel-Streuung sensitive Dunkelfeld Signal. Die Qualität der mit einem Röntgen-Gitter-Interferometer aufgenommen Bilder hängt dabei stark von den verwendeten absorptions- und phasen-schiebenden Röntgengittern ab. Dabei stellt speziell die Herstellung der Absorptionsgitter nach wie vor eine Herausforderung dar, da diese große Aspektverhältnisse benötigen. Um diese Anforderungen zu erfüllen haben sich verschiedene Herstellprozesse etabliert: zum einen Prozesse die auf dem Ätzen von Silizium basieren, zum andern Prozesse die auf der am Synchrotronquellen durchgeführten Röntgen-Tiefen-Lithographie basieren.

Die Ergebnisse dieser Arbeit sind in zwei Teile gegliedert: Der erste Teil beschäftigt sich mit der Weiterentwicklung der Herstellung von Röntgenabsorptionsgittern. Dazu wurde der Abfüllprozess von silizium-geätzten Gitterstrukturen mit absorbierenden Partikeln weiter entwickelt. Hierzu wurden zum einen Wolframpartikel verschiedener Größen gemischt um die Partikeldichte in den Gitterstrukturen zu erhöhen. Zum anderen wurde gezeigt, dass die Herstellung großer Gitter mit einem Zentrifugationsprozess, der zur Verdichtung der Partikel genutzt wird, realisierbar ist. So wurden Partikelgitter hergestellt, die größer und im Absorptionsverahlten vergleichbar zu herkömmlichen, lithographisch hergestellten Gittern sind. Außerdem wurde der Röntgen-tiefen-lithographische Prozess angepasst, damit dieser an konventionellen Röntgenröhren durchgeführt werden kann, da diese besser verfügbar sind als Synchrotronquellen. Zuerst wurden geeignete Parameter für die Belichtung bestimmt. Danach wurden Methoden entwickelt, um großflächige Gitter herzustellen. Dabei hat sich gezeigt, dass das Biegen von Maske und Substrat während der Belichtung an konventionellen Röntgenröhren für gleichmäßige Gittrstrukturen nötig ist. Der zweite Teil der Ergebnisse beschäftigt sich mit einer angepassten Datenprozessierung für gitterbasierte röntgeninterferometrische Aufbauten, bei denen die Intensiätsmodulation von einer Sinusform abweicht. Um eine Vielzahl verschieder Intensitätsmodulationen berücksichtigen zu können, wurde eine stückweise definierte Funktion eingeführt, die aus Polynomen nullter bis zweiter Ordnung besteht. Diese so definierte Funktion ist in der Lage symmetrische und asymmetrische Intensitätsmodulationen zu beschreiben. Dadurch können Artefakte, die durch das diskrete Abtasten der Intensitätsmodulation entstehen, in den berechneten Bildern reduziert werden.

Contents

1 Introduction

The discovery of X-rays by W. C. Röntgen in 1895 was the starting point for the wide field of X-ray physics [Röntgen, 1895]. Since then, their ability to penetrate matter enabled many nondestructive applications in the field of material sciences and medical imaging. For example, X-ray fluorescence spectroscopy takes advantage of the fact that atoms emit characteristic fluorescence radiation after X-rays interacted with their electron shell. Thus, by measuring the fluorescence spectrum, the chemical composition of a sample can be determined. In contrast, crystallography records diffraction patterns of crystals produced by the diffraction of X-rays at the electron shells of the lattice atoms. Afterwards, the arrangement of the lattice atoms in the crystal can be determined from these diffraction patterns. For X-ray imaging, initially it was exploited that X-rays are attenuated to different degrees when passing through objects made of different materials. This allows to capture a shadow images behind objects, revealing details from their inside. However, the measurable contrast depends strongly on the imaged materials, since only absorption differences within an object are measured. For example, bones (high calcium content) absorb X-rays much stronger than soft tissue (especially carbon and hydrogen). This allows to visualize bone fractures in a everyday clinical routine. However, different tissue types are difficult or even impossible to distinguish in the absorption images due to their similar chemical composition. For this reason, various methods have been developed to apply phase contrast, known from visible light imaging, to X-rays. Among the first were Bonse und Hart, using three monocrystalline silicon beam splitters to seperate the X-ray beam into two individual beams which they then recombined again [Bonse, 1965]. An object placed in one of the X-ray paths induces a phase shift which, upon recombination of the two ray paths, produces an interference pattern from which the phase shift can be extracted. Thereafter, further methods for X-ray phase contrast imaging have been developed, including grating-based phase contrast imaging [Ingal, 1995; Snigirev, 1995; Wilkins, 1996; Momose, 2003; Weitkamp, 2005; Pfeiffer, 2006a; Pfeiffer, 2006b; Grünzweig, 2008; Munro, 2012; Zanette, 2014].

In grating-based phase contrast imaging usually the Talbot effect is exploited to generate a periodic intensity modulation, using a so-called reference grating G_1. Since these intensity modulations cannot be resolved by typical detector pixels, they are usually sampled with an additional analyzer grating G_2 [Momose, 2003; Weitkamp, 2005]. This allows to determine changes and position shifts of the intensity modulation, which are caused by an object. As all phase contrast imaging methods have high coherence requirements, an additional so-called source grating G_0 is introduced to allow the use of low coherent sources such as X-ray tubes [Pfeiffer, 2006a]. Since this source grating has to follow the requirements of the Lau effect, such three grating interferometers are also called Talbot–Lau interferometers. Besides ab-

sorption and phase contrast, grating-based imaging provides access to a third image modality: the so-called dark-field contrast [Pfeiffer, 2008]. Therefore, the amount of small-angle scattering induced by an object is measured. This allows conclusions about the microstructure of an object, which cannot be directly resolved with the detector. Small animal studies have demonstrated that this can be employed in lung imaging, for example, to detect changes in the alveoli [Schleede, 2012; Yaroshenko, 2015; Hellbach, 2016; Scherer, 2017; Hellbach, 2018]. Recently, the method has been successfully adapted for human thorax imaging and initial diagnostic capabilities have been reported [Willer, 2021].

As the name grating-based imaging suggests, the gratings used are core components of this method. Thus, the gratings have a strong influence on the image quality of a setup. However, the availability of high quality gratings is still a limiting factor in the design of the imaging setups. Especially absorption gratings pose a problem since they require high aspect ratio (ratio of width to height of the structures) structures in the µm-range that periodically absorb the X-ray radiation. The so-called direct deep X-ray LIGA-process (germ. Lithographie, Galvanik, Abformung) is one suitable method to fabricate such absorption gratings. At first, a thick resist layer is coated on a conductive substrate and exposed to a masked X-ray beam (deep X-ray lithography). Then, the structure is chemically developed and filled with gold by electroplating [Reznikova, 2008; Noda, 2008; Goettert, 2012; Meyer, 2010]. To achieve high aspect ratios the steep resist structures have to be connected with supporting structures (‘bridges’) which reduce the grating performance. The X-ray lithography step is usually performed at synchrotron facilities since it requires a certain degree of beam coherence, adaptable energy, and bandwidth as well as high intensity. This limits the availability of the method for development and high volume production.
Several other fabrication methods for high aspect ratio grating structures are based on silicon etching. Thereby, a grating structure is transferred into a silicon wafer by anisotropic wet etching [David, 2007; Finnegan, 2019], plasma etching [Romano, 2017b; VilaComamala, 2018; Hollowell, 2019; Shi, 2020], photo-assisted electrochemical etching [Lei, 2014; Lei, 2016], or metal-assisted chemical etching [Romano, 2017b; Romano, 2020a; Romano, 2020b]. Afterwards, the resulting structures can be filled with highly absorbing materials using electroplating [David, 2007; Hollowell, 2019; Romano, 2020b; Josell, 2020; Jefimovs, 2021], atomic layer deposition [VilaComamala, 2018], metal casting [Lei, 2014; Lei, 2016], hot embossing [Romano, 2017a; Romano, 2017b], or deposition of particles [Gustschin, 2018; Lei, 2019a; Lei, 2019b; Hojo, 2019]. While etching the grating template is straight forward due to wide process availability in the semiconductor industry, a homogeneous filling of such deep structures introduces various challenges. Electroplating, the most applied metalization technique, requires plating contacts at the bottom of the trenches [David, 2007] or other modifications [Jefimovs, 2021] to avoid voids in the filling.

Despite this variety of fabrication methods, the availability of gratings remains a bottleneck of grating-based imaging. For this reason, this work deals with improving individual process steps of already known fabrication methods. To overcome the dependence of the LIGA process on synchrotron sources, the deep X-ray lithography step is adapted to be performed with widely available conventional X-ray tubes. In addition, the manufacturing process based on the deposition of particles in etched silicon wafers is further improved to optimize both the

particle filling and the grating area. Furthermore, an adapted processing method is developed to account for non-sinusoidal intensity modulations that can be caused by different grating configurations in grating-based imaging.

Outline

Chapters 2 and 3 describe the theoretical background of this work. In this context, chapter 2 gives an overview on the generation of X-rays and their interactions with matter, as well as the basics of grating-based phase and dark-field imaging. Several methods for fabricating gratings needed in grating-based imaging and materials suitable for this purpose are provided in chapter 3. Chapter 4 addresses particle-based absorber filling for grating structures etched in silicon. For this purpose, tungsten particles are filled into the trenches of etched silicon grating templates by applying centrifugation. It is shown that by mixing particles of different sizes, the filling ratio can be increased. Finally, a large-area grating is successfully filled with tungsten particles and characterized afterwards. In chapter 5 the fabrication of X-ray gratings by deep X-ray lithography at a conventional X-ray tube is described. In this context, differences between an X-ray tube and the commonly employed synchrotron sources are discussed. After various exposure tests, it is described how a grating is successfully exposed and thereafter characterized. An alternative processing algorithm for grating-based imaging is presented in chapter 6. Therefore, a polynomial piece-wise defined function is used to model the natural formation process of the measured intensity modulations. This algorithm is then analyzed using simulated and experimental data. Finally, the conclusion and outlook are discussed in chapter 7.

2 Physics of X-ray imaging

X-rays are electromagnetic waves with wavelengths in the range of a few Ångström (1 Å = 10^{-10} m) and are located between the ultraviolet and gamma ray regimes as visualized in Figure 2.1. Although there is no clear distinction between these regimes, the transition between them is in the range of a few 100 eV between ultraviolet and X-rays and a few 100 keV between X-rays and gamma radiation. Like all other radiations in the electromagnetic spectrum, X-rays travel in vacuum with the speed of light $c = 2.998 \times 10^8\,\mathrm{m\,s^{-1}}$ and their energy E_p is given by:

$$E_p = \frac{hc}{\lambda} = \hbar\omega, \tag{2.1}$$

with Planck's constant h ($\hbar = h/(2\pi)$), the wavelength λ, and angular frequency of the radiation $\omega = 2\pi f$, where f is the radiation's frequency. [Attwood, 1999; AlsNielsen, 2011; Willmott, 2011]

2.1 Generation of X-rays

X-rays can be generated in a number of ways. The following section will focus on conventional X-ray tubes and synchrotron sources, since these are often used X-ray sources.

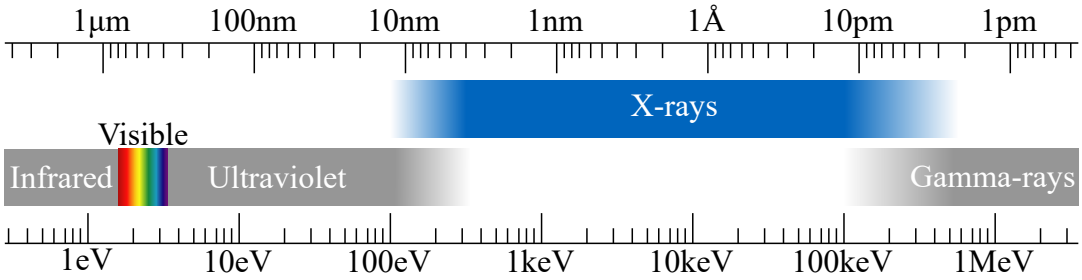

Figure 2.1: Part of the electromagnetic spectrum in the energy range from 1 eV to 1 MeV including infrared, visible light, ultraviolet, X-rays and gamma-rays. The X-ray regime covers the range from a few 100 eV up to a several 100 keV (figure adapted from [Attwood, 1999; Cerrito, 2017; Andrejewski, 2021]).

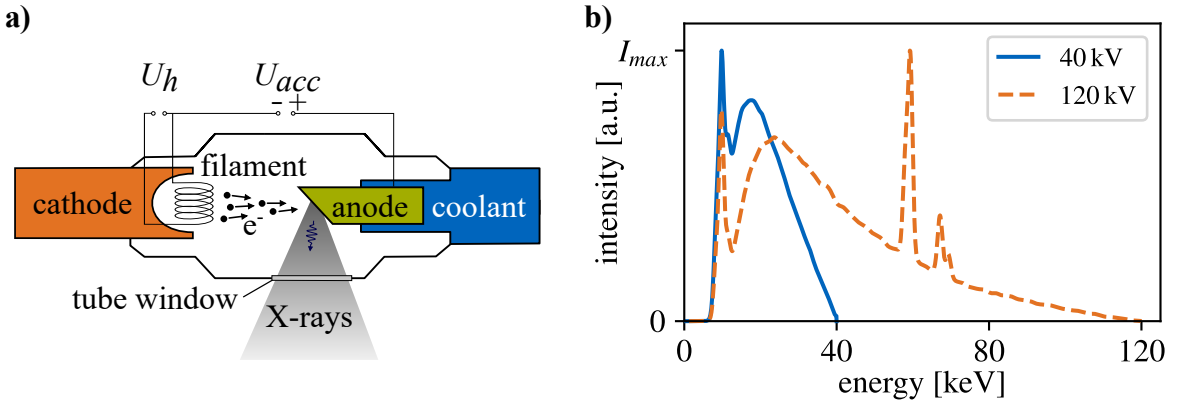

Figure 2.2: **a)** Typical design of a conventional X-ray tube. Electrons are thermaly emitted from a filament by applying a heating voltage U_h. An acceleration voltage U_{acc} accelerates these electrons from the cathode towards the anode. Since most of the electron's energy is converted into heat, a coolant removes the heat from the anode. Only a small fraction of the energy is converted to X-rays (figure adapted from [Gustschin, 2016]).
b) Two spectra simulated for a tungsten anode X-ray tube with 40 kV and 120 kV acceleration voltage. For both spectra the continuous bremsstrahlung spectrum and characteristic tungsten lines are visible. (simulated by [NEA, 2012]).

2.1.1 Conventional X-ray tubes

The basic principle behind conventional X-ray tubes is to collide high-energy electrons with a target material. Due to interactions between the electrons and the target material photons in the X-ray regime are generated.

In common X-ray tubes, as schematically illustrated in Figure 2.2 **a)**, electrons are thermally emitted from a metal conductor by applying a heating voltage U_h. An acceleration voltage U_{acc}, applied between the metal conductor (cathode) and a metal anode, accelerates these electrons until they reach the anode. Thus, the electrons receive a kinetic energy given by

$$E_e = q_e U_{acc}, \tag{2.2}$$

where q_e is the elementary charge of an individual electron and U_{acc} is typically chosen between 5 kV and 200 kV. In addition, a high vacuum must be present in the tube to prevent the electrons from colliding with gas molecules, which would result in energy losses. The electrons then interact with the anode material, transforming a large part of their energy into heat. Therefore, metals with high thermal conductivity and high melting point (e.g. tungsten, or molybdenum) are usually applied as anode material. In addition, the anode is usually actively cooled to allow operation of the X-ray tube at higher power. Except of heat, about one percent of the energy is converted into X-rays, whose spectrum is composed of two different components. The first component, namely bremsstrahlung (from the German *bremsen* for brake), has a continuous spectrum and is generated by the deceleration of electrons in the Coulomb field of the anode atoms. The maximum energy of this spectrum is limited by

the energy of the initial electrons. The second component is a fluorescence spectrum which superimposes the continues spectrum with its sharp lines. In a collision with an atom, an incident electron with sufficient energy can remove an electron from one of the inner atom shells. The resulting vacancy is then filled by an electron from an energetically higher shell, emitting a photon with an energy characteristic of the anode material. Figure 2.2 **b)** shows simulated spectra of an X-ray tube with a tungsten anode operated at 40 kV and 120 kV. Following equation (2.2), for both spectra the maximum energy is determined by the accelerating voltage U_{acc} and characteristic emission lines only are present below this energy. The total energy E_{tot} of an X-ray spectrum can be calculated by:

$$E_{tot} = \int_0^{E_{max}} E\, I(E)\, dE = \sum_{i=1}^{N} E_i\, I(E_i), \tag{2.3}$$

where E_{max} is the maximum energy of the spectrum given by equation (2.2), and $I(E)$ is the energy dependent intensity. In case of an energy binned spectrum with N bins, the integral transforms to a finite sum over the bin index i with the corresponding energy E_i. [AlsNielsen, 2011]

A major advantage of X-ray tubes is their simple design and the resulting high availability for all kinds of laboratory-based experiments and imaging setups. Additionally, large opening angles of the radiation allow large field of view applications at relatively short setup lengths. However, simple X-ray tubes are limited in their maximum X-ray flux, since most of the energy is converted into heat. One solution to this problem is the introduction of rotating anodes. By rotating the anode beneath the electron beam, the heat is distributed over a larger area, which significantly increases the power of X-ray tubes. Especially for high-resolution X-ray imaging a small source spot size is of crucial importance. By using electron optics, the incident electron beam can be focused to a small spot on the anode, reducing the size of the source spot. However, the source power has to be reduced caused by increased heat load on the small spot. Further improvements in source spot size can be achieved by using transmission mode tubes based on thin or liquid metal jet anodes.

2.1.2 Synchrotron sources

Another source of X-rays are synchrotron facilities. At these facilities charged particles (typically electrons) are accelerated to relativistic speed and are subsequently transferred into a storage ring, where they are kept at constant energy. Thereby, electromagnetic radiation is emitted when the charged particles are forced onto a curved trajectory. This is comparable to the previously discussed bremsstrahlung, where electrons are decelerated. While bremsstrahlung in an X-ray tube is emitted isotropically, synchrotron radiation is emitted in a narrow cone in forward direction due to relativistic effects. The width of the emitted cone is proportional to the relativistic Lorentz factor ($\gamma = 1/\sqrt{1-(v/c)^2}$). Usually, three different structures are used for the generation of X-rays at synchrotron: bending magnets, wigglers, and undulators.

Bending magnets are a fundamental part of the storage ring to keep the charged particles on a circular path. By inducing a magnetic field they cause a curved trajectory of the charged particles. The radiation emitted in this process is characterized by a continuous spectrum with a critical energy E_c given by [AlsNielsen, 2011]

$$E_c[\mathrm{keV}] = 0.665 \times E_e^2[\mathrm{GeV}] \times B[\mathrm{T}], \tag{2.4}$$

where E_e is the electron energy and B the magnetic field strength. E_c divides the spectrum into two equal parts of radiated power, whereby the intensity decreases rapidly for energies larger than E_c. Since the charged particle emits radiation at any point along its curved trajectory, the emitted cone has a larger opening angle in the storage ring plane than perpendicular to it (Note that this opening angle is much smaller than for X-ray tubes).

To increase the emitted intensity, wigglers consisting of multiple magnets with alternating magnetic field direction can be used. The alternating magnetic field forces the charged particles on a series of curved trajectories with large oscillation amplitude leading to a "wiggling angle" which is larger than the opening angle of the emitted radiation. Compared to bending magnet radiation, the emitted spectrum has a higher critical energy E_c and a $2N$-times higher intensity, where N is the number of wiggling periods.

Similar to wigglers, undulators are also constructed from magnets with alternating magnetic field direction. Unlike wigglers, the charged particles oscillate only slightly, keeping the wiggling angle small compared to the emitted radiation. Thus, for certain wavelengths, the emitted radiation at one oscillation is in phase with the radiation of the following oscillation. This results in constructive interference for these wavelengths and thus in a quasi-monochromatic (due to the finite number of oscillations N) spectrum with higher harmonics. Since the amplitudes of the radiation add up coherently, the obtained intensity can be N^2 times larger than for a single magnet and the opening angle is even narrower than for wigglers.

Regardless of whether a bending magnet, a wiggler, or an undulator is used, the emitted radiation is then guided to the experimental stations through beamlines arranged tangentially to the storage ring. The radiation can be further manipulated by monochromators, filters, or optics to meet the requirements of the particular experiment.

2.2 Properties of X-rays

Depending on the application, the X-ray radiation must fulfill different requirements. In X-ray absorption imaging, for example, the energy of the radiation influences the transmission of objects, while the photon flux has an effect on the exposure time. In X-ray diffraction imaging and interferometry the beam coherence and brilliance are further crucial beam properties.

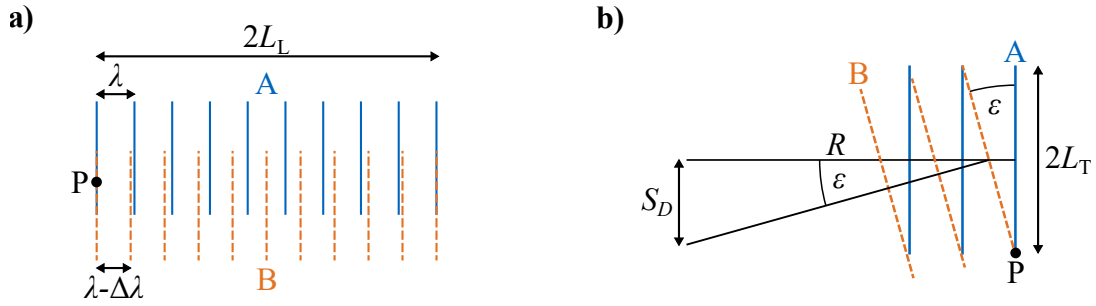

Figure 2.3: Longitudinal and transverse coherence lengths (L_L and L_T). **a)** Two plane waves with a small difference in their wavelength $\Delta\lambda$ propagate in the same direction. After a propagation distance of L_L they are completely out of phase by a factor of π. **b)** A finite sized source of height S_D emits two plane waves with identical wavelength. At distance R both waves meet under an angle ε and are in phase at point P. After a distance of L_T along the wave front they are completely out of phase by a factor of π (figure adapted from [AlsNielsen, 2011]).

2.2.1 Coherence

For simplicity, X-rays are often considered as an ideal plane wave emitted from a point source. In some cases, it is additionally considered to be monochromatic. However, in reality, an X-ray beam cannot be assumed to be perfectly monochromatic, nor is it emitted from a perfect point source. The concept of coherence length addresses these two deviations from an ideal X-ray beam.

The case of a non perfectly monochromatic X-ray beam is illustrated in Figure 2.3 **a)**. Two waves A and B propagate in the same direction, where as the wavelength of wave B is $\Delta\lambda$ smaller than the wavelength λ of wave A. At point P, both waves are in phase. With increasing propagation distance, both waves get more and more out of phase and after propagation of the longitudinal coherence length L_L they are completely out of phase. By a further propagation of L_L both waves are again in phase. L_L is thereby given by:

$$L_L = \frac{1}{2}\frac{\lambda^2}{\Delta\lambda}. \tag{2.5}$$

A schematic for the case of an extended source is given in Figure 2.3 **b)**. The sources of two plane waves A and B with the same wavelength λ are separated by a distance S_D. As a consequence, at point P after a propagation distance of R both waves have a slightly different propagation direction and meet under an angle of ε. Again at point P both waves are in phase, but after a distance of L_T (the so called transverse coherence length) along the wavefront of A both waves are completely out of phase. By proceeding to a distance of $2L_T$ both waves are again in phase. L_T is thereby given by:

$$L_T = \frac{1}{2}\frac{\lambda}{\varepsilon} = \frac{\lambda}{2}\frac{R}{S_D}, \tag{2.6}$$

using that ε is given by $\varepsilon = S_D/R$ using the small-angle approximation. [AlsNielsen, 2011]

2.2.2 Brilliance

A parameter used to compare the quality of X-ray sources is the brilliance. It combines different properties of X-ray radiation into a single parameter. The brilliance includes the source size [mm] and the spectral distribution (both important for the coherence), but also the emitted photon flux [photons/s] and the beam divergence [mrad^2], and is defined by:

$$\text{Brilliance} = \left[\frac{\text{photons}/s}{(\text{mm}) \cdot (\text{mrad}^2) \cdot (0.1\%BW)} \right], \tag{2.7}$$

where $(0.1\%BW)$ is the photon energy range within a fixed relative energy bandwidth (BW) of 0.1%. Due to their continuous spectrum, their large source spots and the large beam divergence, conventional X-ray tubes have comparably low brilliance. The brilliance of modern undulators, in contrast, is up to 10 orders of magnitude higher compared to rotating anode tubes. [AlsNielsen, 2011]

2.3 X-ray interactions with matter

Once X-ray radiation is generated, it propagates through space in the form of electromagnetic waves. If this space is not a vacuum, but is filled with matter, interactions between X-rays and matter occur. Since the energy of X-rays is usually in the range of the binding energy of the inner shell electrons, these interactions happen mainly with the electrons of the matter.

2.3.1 Atomic level interaction

The three basic interactions of X-rays with matter are photoelectric absorption, coherent scattering, and incoherent scattering, which are depicted in Figure 2.4. Apart from these three interactions, there is amongst others also pair production. However, since pair production is only possible at energies above 1022 keV and is therefore not relevant for medical imaging and lithographic applications, it will not be discussed further here.

All these interactions have their own interaction cross-section σ describing the probability of interaction between photon and matter. All individual interaction cross-sections add up to the total cross-section σ_{tot}, which describes the entire interaction probability:

$$\sigma_{tot} = \sigma_{ph} + \sigma_{coh} + \sigma_{incoh}, \tag{2.8}$$

where σ_{ph}, σ_{coh}, and σ_{incoh} are the cross-sections of the photoelectric absorption, coherent scattering, and incoherent scattering, which are the three most relevant interactions for this thesis. The total cross-section is typically expressed as mass attenuation coefficient $\frac{\mu}{\rho}$:

$$\frac{\mu}{\rho} = \frac{\sigma_{tot}}{uA}, \tag{2.9}$$

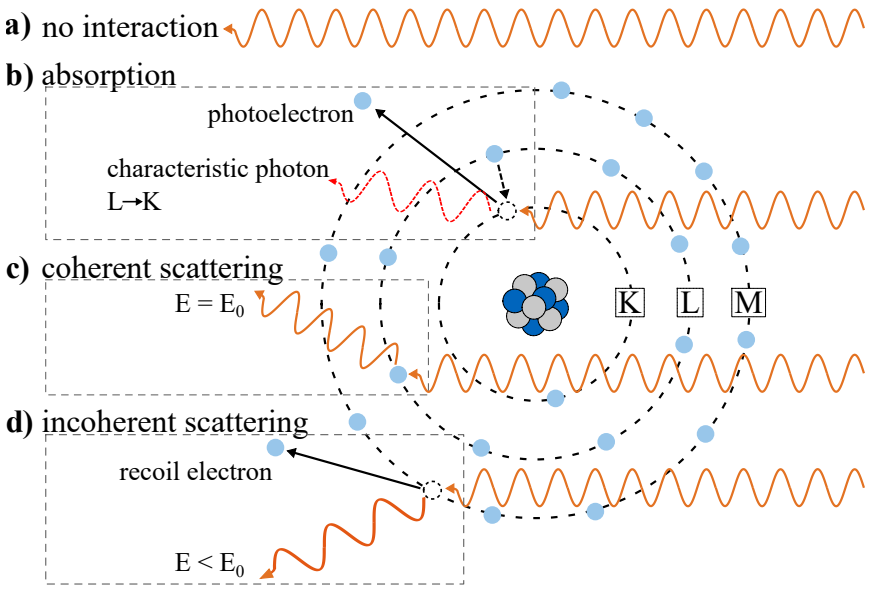

Figure 2.4: Illustration of the X-ray interactions with matter, which are relevant for medical X-ray imaging and X-ray lithography. **a)** In the simplest case no interaction takes place and the photon energy and direction remain unchanged. **b)** In case of photoelectric absorption the photon transfers its entire energy to an electron of the atom shell, which is kicked out of the atom. Subsequently, the vacancy can be filled with an electron from one of the outer shells by emitting an characteristic photon. **c)** In coherent scattering the energy of incident photon and of the electron remain unchanged. Only the propagation direction of the photon is changed. **d)** In incoherent scattering the photon kicks out an electron from the atomic shell by transferring a portion of its energy. At the same time the propagation direction of the photon is changed (figure adapted from [Seibert, 2005]).

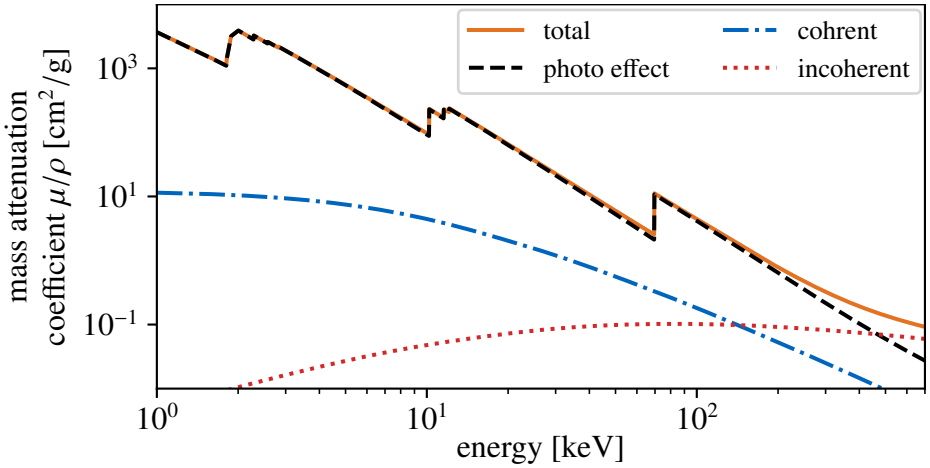

Figure 2.5: Total mass attenuation coefficient μ/ρ of tungsten and contributions of the photoelectric effect, coherent scattering, and to incoherent scattering in a double logarithmic plot. With increasing energy μ/ρ decreases continuously and is only interrupted by the abrupt increase when the binding energy of another electron shell is reached (data from [Schoonjans, 2011]; figure adapted from [Pinzek, 2018]).

where ρ is the material density, u the atomic mass unit, and A the relative atomic mass of the element. Figure 2.5 shows the energy depended mass attenuation coefficient of tungsten and the different contributions of the individual interactions. In the following part these interactions are examined in further detail. [White, 1977; Willmott, 2011]

Photoelectric absorption

If a photon's energy E is higher than the binding energy E_b of an electron in an atom, the photon can transfer its entire energy to this electron. The electron thereby overcomes the binding energy and leaves the atom with a kinetic energy $E_{kin} = E - E_b$. This process is called photoelectric absorption. In the further course, the resulting vacancy in the atomic shell can be filled by an electron from one of the outer shells. Hereby, either a fluorescent photon characteristic for the atom (as depicted in Figure 2.4 **b)**), or an so called auger electron from a outer shell is emitted. In the case of the auger electron, the binding energy of the auger electron must be smaller than the excess energy remaining in the atom.

The higher the energy of the photon, the more electrons can be removed from the atomic shell. With each additional electron that can be removed, the photoelectric cross-section σ_{ph} increases rapidly. This can be seen in Figure 2.5 in form of steps with increased mass attenuation coefficient μ/ρ, which is correlated to σ_{ph} via equations (2.8) and (2.9). Besides these so-called absorption edges, σ_{ph} depends strongly on the energy and the atomic number Z of the element:

$$\sigma_{ph} = \propto \frac{Z^m}{E^3}, \tag{2.10}$$

where m is a value between 4 and 5. [White, 1977; AlsNielsen, 2011; Podgorsak, 2016]

Coherent scattering

In coherent scattering an elastic interaction between incident X-ray and electron takes place. The periodic electromagnetic field of the X-ray causes the electron to oscillate leading to a re-emission of an electromagnetic wave due to dipole radiation. The original and the re-emitted electromagnetic waves differ only in their direction of propagation, while energy and wavelength remain the same as displayed in Figure 2.4 **c)**. After the coherent scattering process, the electron remains in the same state as before, which implies that no energy is transferred to the electron.

The cross-section of coherent scattering σ_{coh} for a single bound electron can be derived from the scattering cross-section (a measure for the scattering power of an electron) and the equation of motion of the oscillating electron, resulting in:

$$\sigma_{coh} = \frac{8\pi}{3} r_e^2 \frac{\omega^4}{(\omega^2 - \omega_r^2)^2 + (\gamma\omega)^2}, \tag{2.11}$$

where r_e is the electron radius, ω the angular frequency of the wave, ω_r is the angular resonanze frequency, and γ is a result of the dissipative force term in the electrons equation of motion (it can be assumed that $\gamma/\omega \ll 1$). This result can be further simplified by assuming that ω is either much smaller ($\omega \ll \omega_r$) or much larger ($\omega \gg \omega_r$) than the resonance frequency of the electron. In the first case, the cross-section simplifies to

$$\sigma_R = \frac{8\pi}{3} r_e^2 \left(\frac{\omega}{\omega_r}\right)^4, \tag{2.12}$$

which has a strong frequency and therefore energy dependence and is called Rayleigh cross-section. In the latter case, the energy of the X-rays is much larger than the binding energy of the electron, so that the electron can be considered as a weakly bound or quasi-free electron. This simplifies the cross section to

$$\sigma_{Th} = \frac{8\pi}{3} r_e^2, \tag{2.13}$$

which is independent of the X-ray frequency and is called Thomson cross-section. [Attwood, 1999; AlsNielsen, 2011; Podgorsak, 2016]

Incoherent scattering

In contrast to coherent scattering, a considerable part of the X-ray photon's energy is transferred to the electron in incoherent scattering. Therefore, the so called Compton effect changes not only the propagation direction but also the wavelength of the incident X-rays

(see Figure 2.4 **d**)). The change in wavelength between incident and scattered X-rays depends on the scattering angle θ:

$$\Delta\lambda = \lambda' - \lambda = \lambda_C(1 - \cos\theta), \tag{2.14}$$

where λ and λ' are the wavelengths of the incident and the scattered X-rays, respectively, and $\lambda_C = h/m_e c$, with the mass of an electron m_e, is the so called Compton wavelength. The energy depended incoherent scattering cross-section of a single electron $\sigma_{KN}(E)$ can be derived from the *Klein-Nishina* formula. The corresponding atomic interaction cross-section is given by multiplying σ_{KN} with the number of electrons in one atom Z:

$$\sigma_{incoh} = Z\sigma_{KN}(E). \tag{2.15}$$

With increasing energy σ_{incoh} increases while σ_{ph} and σ_{coh} decrease. Therefore, Compton scattering becomes the dominant interaction for higher energies. [Attwood, 1999; Willmott, 2011; Podgorsak, 2016]

2.3.2 Wave formalism and complex refractive index

Further, macroscopic phenomena such as absorption, diffraction, and reflection can be described with the help of the complex refractive index n:

$$n = 1 - \delta + \mathrm{i}\beta, \tag{2.16}$$

where δ is the refractive index decrement, and β is the absorption index. The real part $1 - \delta$ describes the elastic interaction of photons with matter (e.g. diffraction), while the imaginary part β describes inelastic interactions (e.g. absorption). For further discussion, we now consider a monochromatic plane wave Ψ given by:

$$\Psi(r,t) = \Psi_0 \cdot e^{-\mathrm{i}(\omega t - k_0 \cdot r)}, \tag{2.17}$$

where r is the propagation distance, t the time, Ψ_0 the initial amplitude of the wave, ω is the angular frequency, and $k_0 = 2\pi/\lambda_0$ the wave vector in vacuum. Since the wave vector k is connected to n via $k = nk_0$, for a wave in matter equation (2.17) changes to:

$$\begin{aligned}
\Psi(r,t) &= \Psi_0 \cdot e^{-\mathrm{i}(\omega t - k \cdot r)} && (2.18)\\
&= \Psi_0 \cdot e^{-\mathrm{i}(\omega t - nk_0 \cdot r)} && (2.19)\\
&= \underbrace{\Psi_0 \cdot e^{-\mathrm{i}(\omega t - k_0 \cdot r)}}_{\text{vacuum propagation}} \cdot \underbrace{e^{-\mathrm{i}\delta k_0 \cdot r}}_{\text{phase-shift}} \cdot \underbrace{e^{-\beta k_0 \cdot r}}_{\text{decay}}. && (2.20)
\end{aligned}$$

The first term represents the vacuum propagation of the wave ($n = 1$) as given in equation (2.17). The second term describes the phase shift and the third term the decay of amplitude of the wave induced by the matter compared to a wave propagating through vacuum. [AlsNielsen, 2011; Willmott, 2011]

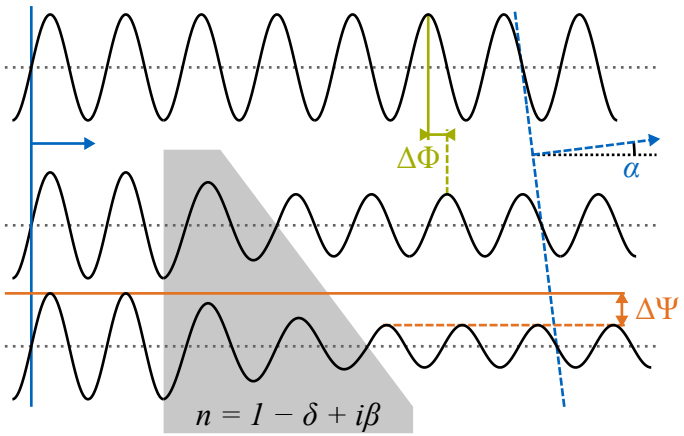

Figure 2.6: Illustration of attenuation and phase shift in an object using the wave formalism. The amplitude of the wave decays exponentially with the propagation distance in an object with complex refraction index $n = 1 - \delta - i\beta$, leading to an amplitude reduction of $\Delta\Psi$. Furthermore, the wavelength changes, resulting in a phase-shift $\Delta\Phi$ compared to a wave propagating through vacuum. In case of a wedge shaped object this phase-shift leads to a refraction angle α (Figure from [Andrejewski, 2021]).

Attenuation

The decay of the wave amplitude for different propagation distances in matter is depicted in Figure 2.6. The amplitude decays exponentially with the propagation distance in matter, causing an change of the amplitude $\Delta\Psi$. However, the wave amplitude is not directly accessible for physical measurements. It is only possible to measure the intensity I of the wave, which can be calculated by the product of complex wave with its complex conjugate Ψ^*:

$$
\begin{aligned}
I(r,t) &= \Psi(r,t) \cdot \Psi^*(r,t) && (2.21)\\
&= \left(\Psi_0 \cdot e^{-\mathrm{i}(\omega t - k_0 \cdot r)} \cdot e^{-\mathrm{i}\delta k_0 \cdot r} \cdot e^{-\beta k_0 \cdot r}\right) \cdot \left(\Psi_0 \cdot e^{+\mathrm{i}(\omega t - k_0 \cdot r)} \cdot e^{+\mathrm{i}\delta k_0 \cdot r} \cdot e^{-\beta k_0 \cdot r}\right) && (2.22)\\
&= \Psi_0^2 \cdot e^{-\mathrm{i}(\omega t - k_0 \cdot r) + \mathrm{i}(\omega t - k_0 \cdot r)} \cdot e^{-\mathrm{i}\delta k_0 \cdot r + \mathrm{i}\delta k_0 \cdot r} \cdot e^{-\beta k_0 \cdot r - \beta k_0 \cdot r} && (2.23)\\
&= \Psi_0^2 \cdot e^{-2\beta k_0 \cdot r}. && (2.24)
\end{aligned}
$$

Note that there is no time dependence in equation (2.24). Further, using the intensity of the incoming wave $I_0 = \Psi_0^2$ and the absorption coefficient $\mu = 2\beta k_0$ leads to the well known *Beer-Lambert* law:

$$I(r) = I_0 \cdot e^{-\mu r}. \tag{2.25}$$

The absorption coefficient μ depends strongly on the X-ray energy. [AlsNielsen, 2011; Willmott, 2011]

Phase-shift

As mentioned before, not only a decay of the wave amplitude takes place when the wave propagates through matter, but also a phase-shift $\Delta\Phi$ compared to the undisturbed wave arises as displayed in Figure 2.6. This phase shift is represented by the second term in equation (2.20) and can therefore be calculated as follows:

$$\Delta\Phi = \delta k_0 \cdot r = \delta \frac{2\pi}{\lambda_0} r. \tag{2.26}$$

For X-rays far from the absorption edges δ is given by:

$$\delta = \frac{2\pi\rho_e r_e}{k^2}, \tag{2.27}$$

where ρ_e is the electron density of the object. Typical values for δ are in the range of 10^{-6}. As already mentioned, only the intensity of an electromagnetic wave can be measured and the phase information is not directly accessible, as shown in equation (2.24). However, by interferometric superposition phase-shifts can be converted into intensity modulations which are measurable.

In the simple case of a incoming plane wave and wedge-shaped object, as shown in Figure 2.6, the phase-shifts lead to a deflection of the radiation by the angle α:

$$\alpha \approx \frac{1}{k} \frac{\partial\Phi(x)}{\partial x}, \tag{2.28}$$

where $\partial\Phi(x)/\partial x$ is the partial derivative of the phase shift perpendicular to the incident beam direction behind the object. This effect is commonly known as refraction of electromagnetic waves. Equation (2.28) holds also for more irregular shaped objects with e.g. a random shaped surface, or a porous inner structure. However, in these cases the incident beam is not refracted uniformly, but is deflected in a random direction due to multiple refraction at a multitude of material interfaces. Microscopically, this can be described as coherent scattering. One possibility to measure these refractive and scattering effects of X-rays is grating-based phase-contrast imaging, which will be described in more detail in the following. [Davis, 1995; Attwood, 1999; Willmott, 2011]

2.4 Grating-based phase-contrast and dark-field imaging

While conventional X-ray imaging is based on different absorption coefficients of materials, exploiting the wave properties of X-rays opens up additional complimentary contrast modalities like phase-contrast and dark-field contrast. To measure the small phase shifts induced

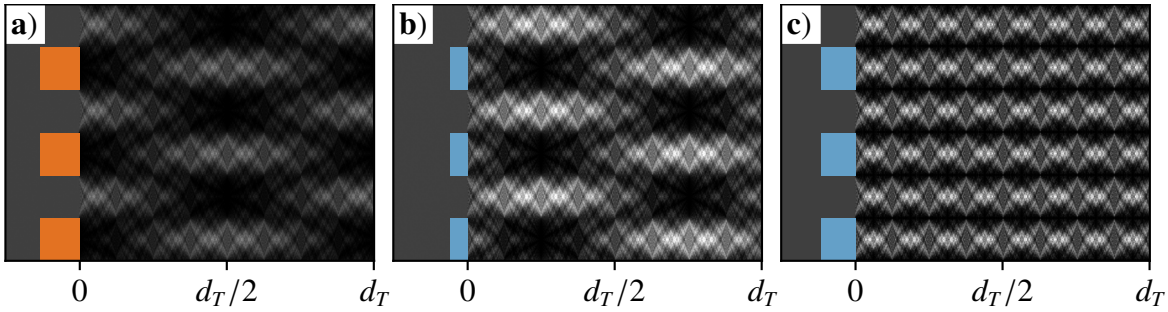

Figure 2.7: Intensity pattern (also called Talbot carpet) behind a periodic grating due to the Talbot effect for **a)** an absorption grating, **b)** a $\pi/2$-phase-shifting grating, and **c)** a π-phase-shifting grating for an incident X-ray beam with parallel geometry (figure adapted from [Weitkamp, 2006]).

by objects, different methods have been introduced in the past, namely crystal interferometry [Bonse, 1965], analyzer-based imaging [Ingal, 1995; Davis, 1995; Chapman, 1997], propagation-based imaging [Snigirev, 1995; Cloetens, 1996; Wilkins, 1996], grating-based imaging (GI) [Momose, 2003; Weitkamp, 2005], edge illumination [Olivo, 2001], single grid [Wen, 2010; Morgan, 2011], and speckle-based imaging [Morgan, 2012; Berujon, 2012]. The following section focuses on grating-based phase-contrast and dark-field imaging in more detail.

2.4.1 Talbot effect and reference grating

To determine the previously described deflection of the radiation caused by objects, a periodic reference pattern can be utilized. By recording this reference pattern and its distortions, the deflection of the radiation can be determined. This requires that the deflection of the radiation and the period of the reference pattern are of comparable length scale. As the deflection of X-rays is usually in the order of 1 µrad and the typical length of imaging setups is in the range of meters, it follows using the small angle approximation that the lateral displacement of the radiation is in the range of 1 µm. Accordingly, the period of the reference pattern must also be in the range of a several µm. One possible way to generate such a reference pattern in the X-ray regime is the so called Talbot effect. It is based on periodic gratings, which create an intensity modulation in the beam path of a sufficient coherent electromagnetic wave. Due to diffraction and interference effects, the wavefront behind the grating reproduces itself at multiples of the Talbot distance d_T given by:

$$d_T = \frac{2p_1^2}{\lambda}. \tag{2.29}$$

Here, p_1 is the period of the applied grating, which will be called reference grating G_1 in the following. However, the Talbot effect does not only occur with absorption gratings, but also with gratings that induce a periodic phase shift. The induced intensity pattern behind the reference grating, also called Talbot carpet, differs a lot, depending on the grating type.

Figure 2.7 displays three Talbot carpets of monochromatic X-ray beams between the reference grating and the first Talbot distance for an absorption grating, a $\pi/2$-phase-shifting grating, and a π-phase-shifting grating. For all three grating types, binary intensity modulations perpendicular to the beam path exist at different positions in the Talbot carpet. This is called fractional Talbot effect and differs quite clearly between the different grating types. For absorption gratings (see Figure 2.7 **a)**), a binary intensity modulation occurs at fractional Talbot distances d_n

$$d_n^{\text{absorption}} = n d_T/2, \tag{2.30}$$

with the fractional Talbot order $n \in \mathbb{N}_0$, but with a lateral shift of a half grating period for odd n. For phase-shifting gratings, no intensity modulation occurs at the Talbot distance, since the wavefront directly behind the grating has only a phase modulation. Nevertheless, factional Talbot distances with binary intensity modulations exist. For a $\pi/2$-phase grating (see Figure 2.7 **b)**), these can be observed for fractional Talbot distances

$$d_n^{\pi/2\text{-phase shift}} = (2n-1) d_T/4, \tag{2.31}$$

with $n \in \mathbb{N}$. Similar to absorption gratings, the intensity modulation is shifted by half a grating period between even and odd n. For π-phase-shifting gratings (see Figure 2.7 **c)**), binary intensity modulations are observable for fractional Talbot distances

$$d_n^{\pi\text{-phase shift}} = (2n-1) d_T/16, \tag{2.32}$$

with $n \in \mathbb{N}$. The period of the intensity modulations is reduced by half compared to the period of the reference grating. Besides the three grating types shown here, there are many other possible reference gratings, which can differ in their duty cycle (DC, ratio of absorbing/phase-shifting area to period), the amount of phase shift, or even their shape (e.g. triangular gratings) [Zhou, 1995; Suleski, 1997].

Modification of the Talbot carpet by objects

As mentioned before, the intensity modulations induced by the Talbot effect can be utilized to determine the influence of objects on the beam path. Usually, three different effects are distinguished: attenuation, refraction, and small-angle scattering. Attenuation describes the decay of the X-ray intensity due to photon-matter interactions. As shown in Figure 2.8 **a)**, a purely attenuating object reduces the intensity of the Talbot carpet. Refraction induces a change in the propagation direction with respect to the incident X-ray beam. This results in a lateral shift of the intensity pattern as shown in Figure 2.8 **b)**. Small-angle scattering leads to a random directional change of the radiation, reducing the amplitude of the intensity modulations in the Talbot carpet. Figure 2.8 **c)** shows the influence of a phase-shifting object with a highly irregular thickness on the Talbot carpet. The resulting differences in the electron density over a sufficiently short distance lead to small-angle scattering of the radiation. By recording the intensity modulation in one of the factional Talbot distances without and with object using a detector, conclusions can be drawn about the attenuation, refractive, and small-angle scattering properties of the object.

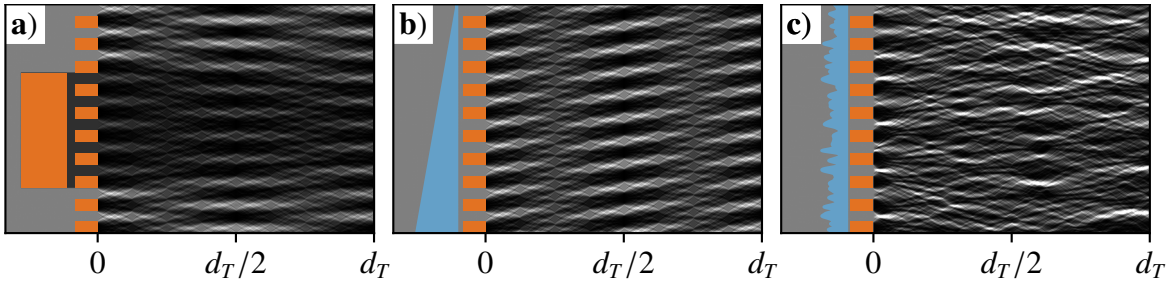

Figure 2.8: Effect of different objects on the Talbot carpet behind an absorption grating. **a)** A purely absorbing object reduces the over all intensity of the Talbot carpet. **b)** The beam is refracted by a purely phase-shifting wedge. As a consequence the intensity modulation behind the reference grating is shifted laterally. **c)** A object out of purely phase-shifting material with thickness variations on a very short length scale induces small-angle scattering. This partially disturbs the regular pattern of the Talbot carpet and reduces the contrast of the intensity modulation (figure adapted from [De Marco, 2021]).

The lateral intensity signal $S(x)$ recorded in the detector plane can be described mathematically with a convolution of the intensity profile $T_1(x)$, which describes a single period of the intensity modulation, and a shifted Dirac comb $\Delta_{p_T}(x) = \sum_{m=-\infty}^{\infty} \delta(x - mp_T)$:

$$S(x) = T_1(x) \otimes \Delta_{p_T}(x - x_d). \tag{2.33}$$

Here, x_d is the lateral displacement induced by a refractive object and p_T is the period of the intensity modulation. [Chabior, 2011]

2.4.2 Analyzer grating

To be able to record the intensity modulations of the Talbot carpet, one needs high-resolution detectors whose pixel size must be at least half as large as the period of the intensity modulation. Since detectors have a limited resolution, for real systems equation (2.33) is extended by another term that takes the point spread function (PSF) of the detector into account:

$$S(x) = T_1(x) \otimes \Delta_{p_T}(x - x_d) \otimes PSF(x). \tag{2.34}$$

This leads to a blurring of the recorded intensity modulation and for a large PSF even prevents measuring any intensity modulation. Although detectors exist that offer sufficient resolution, detectors with pixel sizes in the vicinity of a few 100 µm (and corresponding resolution) are more commonly used. Since these detectors cannot resolve the intensity modulations, an absorption grating, the so-called analyzer grating G_2, is required. The analyzer grating is placed in front of the detector in one of the factional Talbot distances and it's period p_2 is chosen in a way that it matches the period of the intensity modulation behind

the reference grating. The signal recorded in a single pixel can be described mathematically by a multiplication of intensity modulation behind the reference grating $T_1(x)$ with the transmission profile of the analyzer grating $T_2(x)$:

$$S(x, x_r) = \left[(T_1(x) \otimes \Delta_{p_T}(x - x_d)) \cdot T_2(x) \otimes \Delta_{p_2}(x - x_r)\right] \otimes PSF(x), \tag{2.35}$$

where x_r is the relative displacement between the intensity modulation and the analyzer grating. Since $p_T \approx p_2$ can be assumed, neighboring pixels observe similar x_r and thus similar $S(x, s_r)$, decoupling the measured signal from the PSF. The intensity modulations over the area of the detector caused by a slight mismatch between the two periods are called Moiré-fringes and can be easily resolved. By shifting (also called stepping) one of the two gratings laterally by x_r it is possible to sample the intensity modulation. For the following sections it is assumed that a continuous scan of the relative grating position x_r is performed. In this case, the recorded intensity modulation can be described as convolution of the intensity modulation T_1 with the transmission profile T_2. In the special case where T_1 and T_2 are binary functions with a DC of 0.5, a triangular intensity profile is obtained. [Momose, 2003; Chabior, 2011]

2.4.3 Source grating

So far, only plane waves have been considered. However, in reality, the finite extent of the X-ray source has to be accounted. For this purpose, each point of the source can be seen as individual point sources that create individual overlaying images. This results in a blurring of the image in the detector plane (also called source blurring), as illustrated in Figure 2.9 **a)**. The amount of blurring is given by the projected source size q in the detector/G_2 plane by:

$$q = \frac{d}{l} \cdot w. \tag{2.36}$$

Here, w is the lateral extend of the source, d the distance between reference grating and analyzer grating, and l the distance between source and reference grating. Note, that for $l \to \infty$ this includes the case of a plane wave. Mathematically, the effect of the source blurring in a plane can be calculated by a convolution of the lateral intensity distribution of the Talbot carpet $T_1(x)$ with the projected lateral source distribution $T_0(x)$ in this plane. Thus, one obtains for the recorded intensity signal:

$$S(x, x_r) = T_0(x) \otimes T_1(x) \otimes \Delta_{p_T}(x - x_d) \otimes T_2(x) \otimes \Delta_{p_2}(x - x_r) \otimes PSF(x). \tag{2.37}$$

As a result, the contrast of the recorded intensity signal disappears for large source sizes. To measure an intensity modulation in spite of source blurring, the source size must be chosen such small that the projected source size is at least smaller than half the period of the analyzer grating [Bech, 2009]. For example, this can be achieved by applying microfocus X-ray tubes. Another way is to insert a small aperture, which limits the source spot to an effectively smaller size, as shown in Figure 2.9 **b)**. However, in both cases the X-ray flux is strongly reduced compared to high power X-ray sources with large source sizes. To overcome this, an

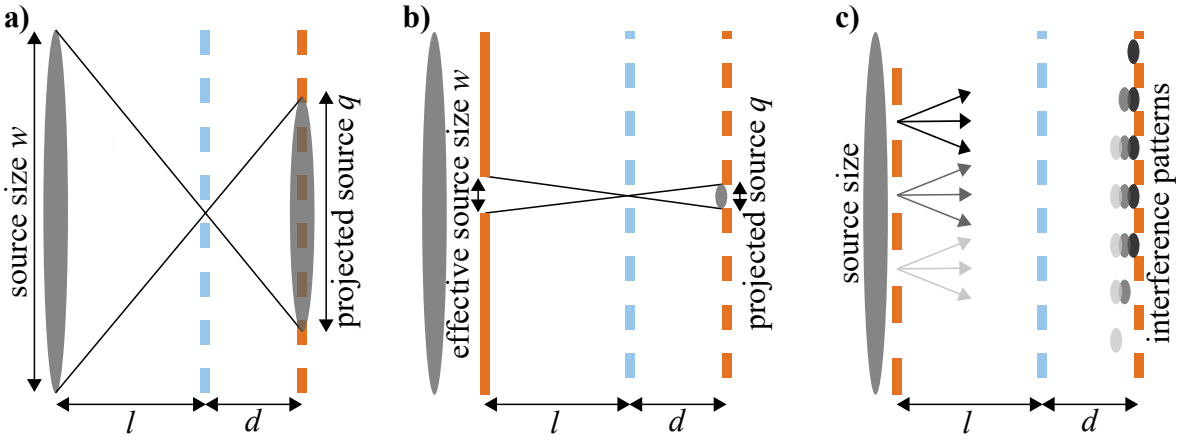

Figure 2.9: Illustration of the source influence in a grating interferometer. An extended source blurs out the intensity modulation in the G_2 plane by the amount of its projected lateral size q. **a)** For large source sizes, the contrast of the intensity modulation will vanish completely. **b)** By introducing a slit aperture the source size is effectively decreased which limits the blurring to a tolerable level. **c)** To increase the photon flux it is possible to exploit the Lau effect and apply an array of many such apertures. When the individual apertures are arranged with the period given by equation (2.38), an overlay of the individual images occurs in the G_2 plane (figure adapted from [Chabior, 2011]).

array of many apertures can be used instead of a single aperture resulting in a third so called source grating G_0. This source grating creates a multitude of sufficiently small line sources, each generating its own image. If the distance/period p_0 between the individual apertures is chosen correctly, these images overlap in the G_2 plane, as indicated in Figure 2.9 **c)**. For this case applies:

$$p_0 = p_2 \frac{l}{d}, \tag{2.38}$$

where l is the distance between G_0 and G_1 and d is the distance between G_1 and G_2. This is known as the Lau effect, which is the reason why grating interferometers with a source grating are also called Talbot-Lau interferometers. [Pfeiffer, 2006a; Chabior, 2011]

2.4.4 Influence of cone-beam geometries

The previous considerations assumed a parallel beam path. However, this is only the case for very large distances between source and imaging experiment (in the range of 100 m), as for example at synchrotron beamlines. X-ray tubes, on the other hand, are usually operated at short distances (in the range of 1 m) due to their lower flux and divergent radiation. While this allows for large fields of view, additionally the geometric magnification of objects has to be considered. The geometric magnification factor M is given by:

$$M = \frac{l + d}{l}, \tag{2.39}$$

where l is the distance between source and the magnified object and d the distance between the object and the detection plane. Considering the reference grating as magnified object, the period of the lateral intensity modulation p_T and thus also the period of the analyzer grating p_2 is given by:

$$p_2 \approx p_T = p_1 \cdot \frac{M}{\eta}, \tag{2.40}$$

with $\eta = 1$ for absorbing and $\pi/2$-phase shifting, and $\eta = 2$ for π-phase shifting gratings. Further, the fractional Talbot distances (equations (2.30)-(2.32)) are changed and need to be corrected using the geometrical magnification factor:

$$d_{n,cone} = d_n \cdot M \tag{2.41}$$

Substituting equation (2.39) into equation (2.41) we obtain for the rescaled Talbot distance $d_{n,cone}$ [Weitkamp, 2006]:

$$d_{n,cone} = \frac{l \cdot d_n}{l - d_n}. \tag{2.42}$$

Therefore, no fractional talbot orders are observable for $d_n \geqslant l$, since $d_{n,cone}$ goes to infinity in these cases.

This raises the question which fractional Talbot orders are feasible in a cone beam setup with given length $s = l + d_{n,cone}$. Starting from the given total length s, equation (2.42) results in a quadratic equation for l, whose solutions are given by:

$$l_{\pm} = \frac{s}{2} \pm \sqrt{\frac{s^2}{4} - s d_n}, \tag{2.43}$$

where d_n is the fractional Talbot distance in a parallel beam geometry. From this solution three different cases can be identified. For $s < 4d_n$ no solution exists, since the discriminant is negative. In the second case for $s = 4d_n$ only a single solution exists. This is achieved with a symmetric configuration, where $l = d$ holds and thus $d = d_{n,cone} = d_n \cdot \frac{l+d}{l} = 2d_n = \frac{s}{2}$. The third case is given for $s > 4d_n$, where two solutions for l exist. Typically the solution for $l = l_+ > d$ is called conventional geometry, while the solution for $l = l_- < d$ is called inverse geometry [Donath, 2009].

Especially inverse geometry offers several advantages, which are relevant for the fabrication of the required gratings. The G_0 is the grating with the smallest period, which makes the fabrication difficult due to the high aspect ratio. However, since the G_0 is placed close to the source, only a small area is needed for it. Since the G_1 is placed closer to the source than in the conventional or symmetric geometry, a smaller area is required for this grating as well. Furthermore, the period of the G_2 (which requires the largest area) is significantly increased compared to the other two geometries, reducing the requirements for the fabrication of this grating.

2.4.5 Signal extraction

As described in equation (2.37), the recorded signal in a Talbot-Lau interferometer is given by convolutions of the three grating profiles and the detector PSF. For the following considerations all three grating profiles are assumed as rectangular functions and the PSF as an ideal box-like modulation transfer function whose maximum resolvable spatial frequency is given by the pixel period. Since the recorded intensity signal is periodic and repeats after shifting the grating by one grating period, it can be expressed by a Fourier series:

$$S(x, x_r) = a_0 \cdot \left[1 + \sum_{n=1}^{\infty} v_n \cos\left(2\pi(x + x_r - x_d)\frac{n}{p})\right)\right], \tag{2.44}$$

where a_0 is the mean of the recorded intensity signal and v_n is the amplitude of the n^{th} order oscillation. Chabior et al. [Chabior, 2012] pointed out that with commonly used grating parameters (DC between 0.25 and 0.75 for G_0 and a DC of 0.5 for G_1 and G_2) only an error in the range of 3% arises if the orders $n > 1$ are neglected. Hence, the signal recorded in a pixel at location x can be further simplified in good approximation:

$$S(x_r) = a_0 + a_1 \cdot \cos\left(2\pi\frac{x_r}{p} - \varphi\right), \tag{2.45}$$

where the amplitude is given by $a_1 = a_0 \cdot v_1$ and the phase-shift by $\varphi = 2\pi x_d/p - 2\pi x/p$ (where x_d is the influence of a refractive object). From the three parameters a_0, a_1, and φ, the three image modalities transmission, dark field, and differential phase can be determined in each pixel. As already mentioned, the parameter a_0 is the average intensity of the recorded intensity modulation and represents the attenuation signal as it is recorded in a classical radiography. The transmission signal T for an absorbing object is then determined from the ratio between a reference acquisition without an object in the beam path and an object acquisition (indicated by superscript ref or obj, respectively):

$$T = \frac{a_0^{\text{obj}}}{a_0^{\text{ref}}}. \tag{2.46}$$

As illustrated in Figure 2.10 **a)** an absorbing object decreases the overall intensity of the intensity modulation and therefore lead to a transmission value $T < 1$. The contrast between maximum and minimum intensity (I_{max} and I_{min}) of the intensity modulation is called visibility V [Pfeiffer, 2008]:

$$V = \frac{I_{max} - I_{min}}{I_{max} + I_{min}} = \frac{a_1}{a_0}. \tag{2.47}$$

Due to a scattering object in the beam path, the amplitude a_1 of the intensity modulation is reduced while it's mean a_0 remains unchanged (see Figure 2.10 **b)**). Therefore, the visibility is reduced by the object and by comparing it with the reference visibility one obtains the so called dark field signal D:

$$D = \frac{V^{\text{obj}}}{V^{\text{ref}}}, \tag{2.48}$$

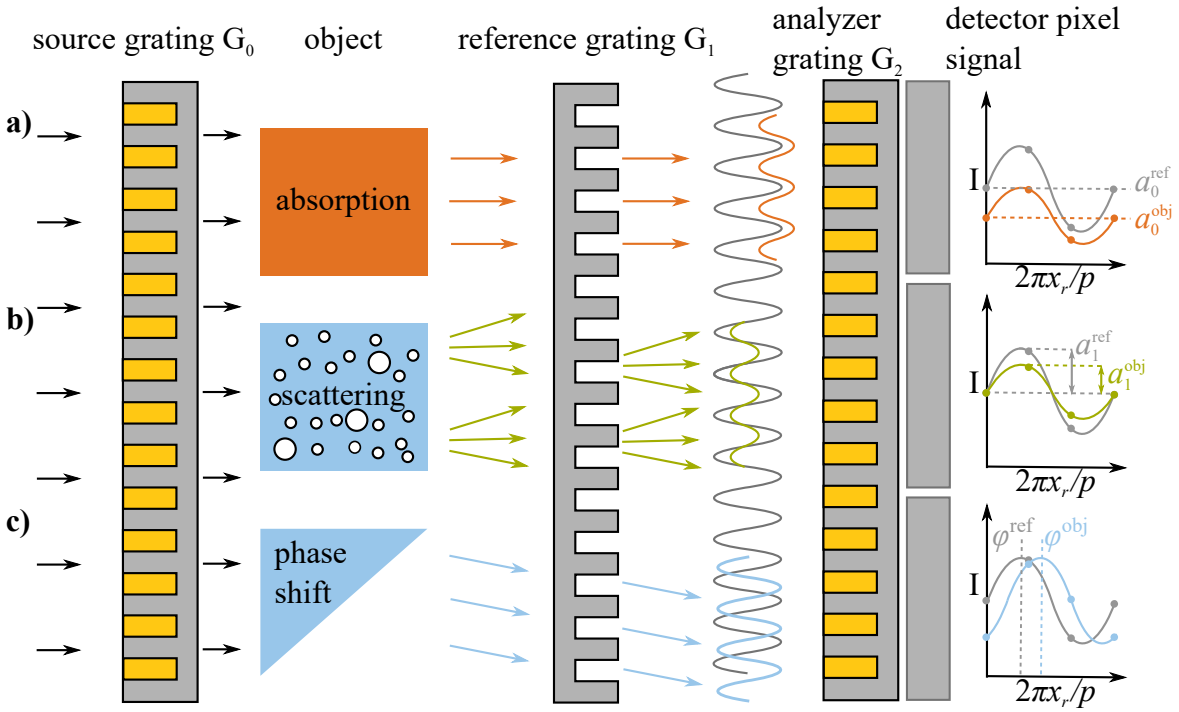

Figure 2.10: Visualization of the signal generation and extraction in a Talbot-Lau interferometer. The intensity modulation is acquired for each pixel by stepping one of the three gratings. By fitting equation (2.45) to the recorded sampling points the parameters a_0, a_1, and φ can be determined. **a)** A purely absorbing object leads to an overall reduction of the intensity and thus to an reduced a_0. At the same time the visibility V remains unchanged. **b)** Small-angle scattering reduces the amplitude a_1, but causes no change in the mean value a_0. **c)** A refractive object causes a lateral displacement of the intensity modulation and therefore to a shift in the recorded stepping curve (figure adapted from [Gustschin, 2016]).

which is a measure for the amount of small-angle scattering in an object. The third image modality is the differential phase, which is sensitive to refractive objects in the ray path. Due to the object related lateral displacement of the intensity modulation x_d, the phase-shift φ differs between reference and object acquisition, as indicated in Figure 2.10 **c)**. Thus, the differential phase $\Delta\varphi$ can be calculated from:

$$\Delta\varphi = \varphi^{\text{obj}} - \varphi^{\text{ref}}. \tag{2.49}$$

Up to this point, we have assumed that by continuously moving one of the grating we can record the entire intensity modulation. In a real experiment, however, this is not possible due to the limited photon flux and the resultant exposure times. Furthermore, it is technically infeasible to move the grating with arbitrary high precision. Therefore, the intensity modulation is sampled at finite grating displacements x_r (also called steps). To determine the parameters a_0, a_1 and φ and thus the three image modalities from the recorded sampling points, at least 3 sampling steps are required. By choosing equidistant steps between these points, a simple Fourier based reconstruction is possible. But also with irregular but known step widths a reconstruction is possible by using least square optimization. It was shown that hat imprecise phase-stepping ('jitter', deviation between assumed and actual grating positions during stepping due to vibrations in the system or due to inaccuracy of the stepper) can cause noise in all three image modalities [Revol, 2010]. Wang and Han [Wang, 2007] suggested an iterative expectation maximization (EM) algorithm to compensate noise induced by imprecise phase stepping , which was adapted for X-ray grating interferometry by Maschner et al. [Marschner, 2016]. Pelzer et al. [Pelzer, 2015] implemented another approach based on principal component analysis, which was proposed by Vargas et al. [Vargas, 2011]. However, many other modifications and combinations were discussed in literature [Seifert, 2016; Kaeppler, 2017; De Marco, 2018; Hashimoto, 2020]. All these approaches optimize the grating position x_r by considering all detector pixels.

3 X-ray gratings

In X-ray grating interferometry the employed gratings are crucial for signal formation. Their properties highly influence the quality of the acquired images. Therefore, the availability of high quality gratings is fundamental to ensure broad access to this technology. Especially the fabrication of absorption gratings is still a bottleneck of X-ray grating interferometry, as they require large structure heights to absorb X-rays sufficiently and at the same time small periods to achieve sufficient phase sensitivity. Moreover, the fabrication of large-area gratings (e.g. for the analyzer grating) is still a challenge.

This chapter presents an overview of the state of the art X-ray grating fabrication. These methods can be split up into LIGA-based (German Lithographie, Galvanik, Abformung) and silicon etching-based approaches. Afterwards, several methods for the characterization of gratings are introduced.

3.1 Grating materials

Gratings typically employed for grating interferometry consist of a carrier substrate and the periodic grating structure. The substrate has to be stable enough to handle the grating safely but also as transparent as possible to the used radiation. For imaging setups with a divergent beam geometry, the substrate should additionally be flexible enough to bend it with the source spot in focus. This is particularly relevant for source gratings, as these are usually placed close to the source and therefore require particularly small bending radii. The periodic grating structure itself must meet different requirements depending on the application. For phase gratings, materials are needed which introduce a strong phase shift and at the same time absorb as little radiation as possible. For absorption gratings, in contrast, the attenuation of the material is the decisive factor. In the following, an overview of common materials for substrate and grating structure is given.

3.1.1 Substrate materials

The grating substrate is necessary for handling the grating during the manufacturing process and in the later application. Thus, it requires high mechanical stability, which usually increases with the thickness of the substrate. At the same time, the substrate should be chosen as thin as possible to reduce absorption.

A frequently employed substrate material is silicon (Si). Since silicon is an important part of today's semiconductor industry, it is widely available and wafers are available in many different sizes and thicknesses. Many industrial methods for processing silicon wafers are available, such as etching processes for structuring the substrate or vapor deposition processes to modify the wafer surface. Another advantage is that silicon ($Z = 14$) absorbs X-rays only to a small extent compared to heavier elements. Since the absorption according to equation (2.10) is proportional to Z^m (where m is a value between 4 and 5), materials with a lower Z than silicon are particularly favorable. The elements with the lowest Z that satisfy the stability requirements are beryllium ($Z = 4$) and boron ($Z = 5$). However, beryllium, which is often used as the X-ray window of X-ray tubes, is impractical due to its toxicity. Nevertheless, it is used in some cases as a substrate for X-ray lithographic masks, where low absorption of the substrate is particularly important [Achenbach, 2003]. Also boron can be excluded as a substrate material due to its high cost and low availability. Carbon (C) ($Z = 6$) is therefore the first element that meets the requirements for stability, availability, and safety. Figure 3.1 **a)** shows that in the range from 10 keV to 100 keV the absorption index of carbon is up to a factor of 10 smaller then the absorption index of silicon. Stable carbon substrates can be made from diamond, graphite, and polymer materials. Although diamond is extremely hard, it is not an optimal substrate material due to its high cost. In contrast, graphite is cheap and widely available. Due to the lower atomic number Z, graphite substrates can be chosen more than 10 times thicker than silicon substrates while retaining comparable transmission [Koch, 2015]. At the same time, graphite substrates can be bent to radii of down to 70 mm without detachment of the grating structures [Richter, 2022]. Especially for grating fabrication processes involving electroplating, the intrinsic conductivity of graphite is advantageous. However, the grain structure of graphite causes X-ray scatter, reducing the system visibility when the reference grating is fabricated on a graphite substrate [Koch, 2015]. Various carbon-based polymers (e.g. polyimide (PI)) even have a lower density and thus a higher transmission than graphite. In addition, PI does not have micro structures causing X-ray scatter. Therefore, it can also be used as substrate material for reference gratings.

3.1.2 Grating structure materials

For the grating structure itself, different materials are suitable. Depending on whether it is a phase grating or an absorption grating, there are different requirements to the material. Materials for phase gratings should induce a strong phase shift while absorbing only slightly. For absorption gratings, a strong absorption of radiation is the most important factor. But also available deposition techniques into the grating structures are important.

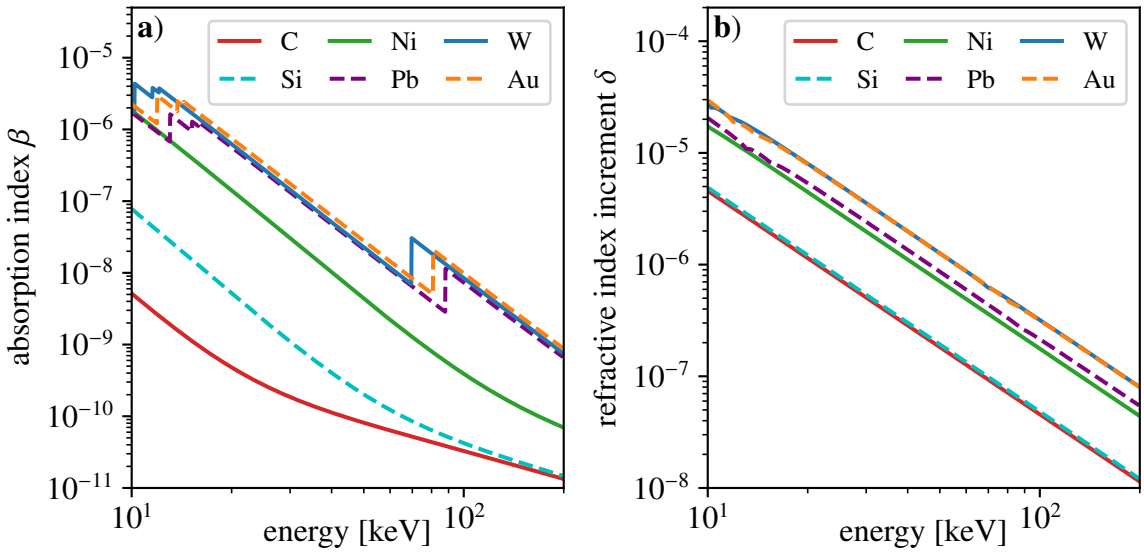

Figure 3.1: Comparison of the refractive index n (as defined in equation (2.16)) of carbon (C), silicon (Si), nickel (Ni), and gold (Au), which are commonly used materials in X-ray grating fabrication. In addition, lead (Pb) and tungsten (W) are shown which are often used as strongly absorbing materials in radiation shielding. **a)** The imaginary part of the refractive index is responsible for the attenuation of the intensity and is given by the absorption index β. **b)** The real part of the refractive index is responsible for the phase shifting properties of materials and is given by $1 - \delta$, where δ is the refractive index increment (data from [Schoonjans, 2011]).

phase shifting materials

For phase gratings, silicon is often used as a phase shifting material. Its advantage is that the silicon can be used as the substitute material at the same time and that it can be structured using various etching processes (see section 3.2.2). But also carbon in the shape of polymer compounds can be used as phase shifting material. For example, photosensitive polymers can be patterned using lithography (see section 3.2.1) and afterwards employed as phase grating. As Figure 3.1 **b)** shows, the refractive index increment responsible for the phase shift is comparable for both materials. As the refractive index increment decreases with increasing energy, the induced phase shift also decreases, requiring larger material heights. Therefore, especially for grating interferometers with higher design energies, it can be interesting to use materials with a higher refractive index increment to relax grating fabrication requirements. Nickel (Ni) or gold (Au) are often used for this purpose, since both materials have a refractive index increment significantly higher than silicon and carbon, and both materials can be deposited by electroplating in a pre-structured grating template. However, as shown by Figure 3.1 **a)**, these materials also have a higher absorption index. Therefore, for each application, it is necessary to consider which phase shifting material is most suitable.

Absorber materials

Since the height of the grating structures is limited, it is important that the used materials transmit as little X-ray radiation as possible at a give height. Therefore, materials with a high atomic number Z and a high density ρ are of particular interest. In addition, the energy of the absorption edges, especially the K-edge, influences the absorption performance. Since energies above the K-edge are absorbed stronger, a K-edge is advantageous at lower energies. At the same time, the amount of secondary radiation due to fluorescence in the absorber material is higher for lower K-edges, which can cause problems in analyzer gratings especially in low dose imaging applications.

The most commonly used material for absorption gratings is gold. Its high absorption index β following its high atomic number $Z = 79$ combined with its high density of $\rho = 19.3\,\mathrm{g\,cm^{-1}}$ yield good absorption properties. Its K-edge is located relatively high at 80.7 keV. This has the disadvantage that the increased absorption above the K-edge is not exploited at energies up to 80 keV, which is typical for X-ray grating interferometry. At the same time, fluorescence of the K-shell can only occur above the K-edge, keeping the amount of secondary radiation caused by the grating at a low level. Further, it possesses many beneficial physical and chemical properties that make it a suitable absorber material for X-ray gratings. These include the feasibility of electroplating gold into grating templates, allowing the fabrication of gold heights up to 300 µm at small periods in the range of a few µm.

Another often used absorption material is lead (Pb) with an atomic number of $Z = 82$. Compared to gold it has a lower density $\rho = 11.3\,\mathrm{g\,cm^{-1}}$ and a higher K-edge at 88.0 keV. Due to its good workability and its low price it is often used in radiation shielding. For

the fabrication of X-ray gratings, one can exploit its relatively low melting point of 327 °C, which is lower than that of the often used substrate material silicon.

Tungsten (W) is often used as absorbing material in collimators since its atomic number Z and density are comparable to gold but at the same time it is considerably cheaper. Its K-edge is located at 69.5 keV, which is about 10 keV lower than the K-edge of gold. In total, tungsten absorbs only slightly less than gold (see Figure 3.1 **a)**), which makes it suitable as an absorber material for X-ray gratings. So far, it has not been reported that tungsten was filled into X-ray gratings by electroplating, and because of its high melting point (which is why it is also used as a filament in light bulbs), it cannot be filled in liquid form like lead, for example. Nevertheless, X-ray absorption gratings can be produced on the basis of tungsten particles (see section 3.2.2 and chapter 4).

In addition to these three materials, there are other materials with good absorption properties, such as bismuth, which has properties comparable to lead. However, due to its low density, which is even lower than that of lead, significantly higher structure heights are required than with gold. In contrast, osmium is the pure metal with the highest density and a comparatively low K-edge of 73.9 keV, making it an excellent absorber material. However, no fabrication methods have yet been reported for the fabrication of high aspect ratio structures based on osmium. Also first high aspect ratio structures based on tantalum [Rinnerbauer, 2013], and iridium [VilaComamala, 2018] (both metals with strong X-ray attenuation) have been reported. Platinum would be a suitable alternative to gold, as it has been extensively researched and similar deposition methods for high aspect ratio structures exist, but there would be no improvement in terms of fabrication. Also, platinum, as well as osmium and iridium, would not provide any advantages in terms of material cost.

3.2 Grating fabrication methods

In the past two decades, various methods for fabricating X-ray gratings have been developed. Here, the so-called LIGA-process and methods based on silicon etching can be distinguished. Although both approaches involve lithography and partly similar methods for the deposition of phase shifting or absorbing materials, they differ in essential manufacturing steps. This section describes the basics of both fabrication processes and discusses their advantages and disadvantages.

3.2.1 LIGA process

In the so called "direct" deep X-ray LIGA-process (germ. **Li**thographie, **G**alvanik, **A**bformung) high aspect ratio structures are produced by deep X-ray lithography (DXRL). The “direct” means that the process ends after the electroplating step (germ. Galvanik) and no replication by molding (germ. Abformung) is performed. An overview of the process is

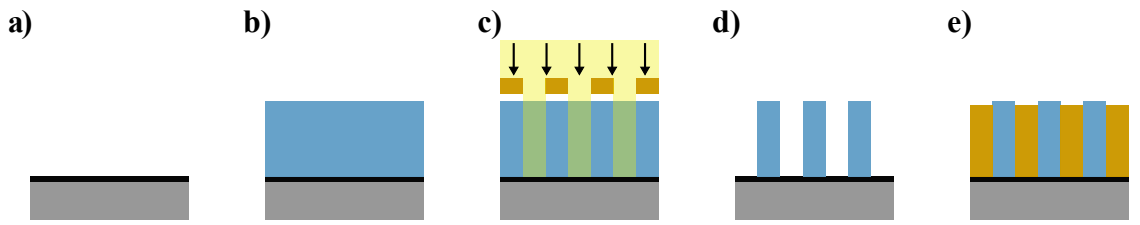

Figure 3.2: For the grating fabrication based on the LIGA process **a)** first a conductive seed layer is applied to the grating substrate. In case the substrate is conductive by itself (e.g. graphite substrates) this step can be skipped. **b)** Then a layer of a photosensitive resist is coated onto the substrate followed by a softbake to evaporate the solvent. **c)** Afterwards the resist is exposed to X-ray radiation using an absorbing mask. **d)** For a negative resist, the exposed regions are then chemically cross-linked in a post-exposure-bake and the non-cross-linked resist is dissolved with a solvent. **e)** Finally, the resulting structure is filled with a phase shifting or highly absorbing material like gold via electroplating (figure adapted from [Pinzek, 2018]).

given in Figure 3.2.

The LIGA process starts with a flat substrate. If the substrate is not electrically conductive itself (e.g. silicon), a conductive seed layer (e.g. titanium oxide) is applied first by sputtering or evaporation (Figure 3.2 **a)**). A photosensitive resist layer is then applied onto the substrate (Figure 3.2 **b)**), where positive and negative resits have to be distinguished. An example of the former is polymethylmetacrylate (PMMA) in which radiation leads to damage of the polymer structure and thus to a reduction of the molar mass. This allows to dissolve the illuminated areas of the polymer in a developer, leaving the non-illuminated structure in place. In the case of negative resists, radiation causes cross-linking of the polymer structure, which increases the molar mass. The most commonly employed negative resist in X-ray lithography is the epoxy resin based SU-8 resist. Its advantage over PMMA is its high sensitivity, which allows to reduce exposure times by a factor of 100. Since only SU-8 based resists are used in this thesis, the process will be described here only for this resist. For the SU-8 the resist deposition can be performed by spin coating followed by a softbake to evaporate the solvent. After the coating step, substrate and resist are exposed to synchrotron X-ray radiation with energies in the range of several keV up to 10 keV (Figure 3.2 **c)**). Synchrotron radiation is used for exposure since it delivers a parallel beam with adaptable energy, bandwidth, and high intensity. The exposure involves absorbing masks, which cover parts of the resist. An initial mask can be written directly using laser or electron-beam lithography, followed by electroplating of gold as absorber. If thick resist layers are to be exposed, these directly written masks can be used as intermediate masks to generate a mask with sufficiently high absorbing structures using the LIGA-process at low X-ray energies. The exposure time depends strongly on the used X-ray source (e.g. flux, spectrum, used filters) and is usually chosen in such a way that a resist specific bottom dose is achieved. Subsequently, a post-exposure-bake (PEB) is performed to complete the cross-linking process in the exposed resist. After completion of the PEB, the non-cross-linked resist can be dis-

solved with a developer chemically, resulting in a negative image of the mask (note that in the case of a positive resist, the remaining structures represent a positive image of the mask) (Figure 3.2 **d)**). The resist structured in this way can already be used as a phase shifting grating in grating interferometers designed for low energy X-rays. However, if the grating is used in a grating interferometer with higher X-ray energies or as an absorption grating, the trenches in the resist structure have to be metalized afterwards (Figure 3.2 **e)**). For this purpose, metals such as gold or nickel can be deposited by electroplating until the required material height is obtained. As an optional step, after electroplating, the cross-linked resist can be removed via dry chemical etching to avoid deformation and unwanted stress during a radiation exposure. [Meyer, 2010]

The LIGA Processes can produce structures with heights of several hundred micrometers or even millimeters, while at the same time the sidewalls of the structures are very smooth (typical local roughness in the order of 10 nm) [Meyer, 2010]. The lateral resolution is limited in the range of micrometers due to the extended range of high-energy secondary electrons released during the X-ray interactions with the resist. As a result, it is possible to fabricate structures with micrometer periods and heights that are multiple times higher at the same time. Thus, absorption gratings with an aspect ratio of 100 have already been demonstrated [Kenntner, 2013]. Due to the large capillary forces acting on free-standing polymer structures with such high aspect ratios during the development step, the designs for X-ray gratings are usually planned with additional support structures called bridges. These bridges ensure that the individual grating lamellae do not collapse and that a uniform period can be maintained over the entire grating area. However, since the bridges are located in the trenches of the absorbing matrix, this causes transparent areas in the phase shifting or absorbing grating lines, which reduce the performance of the grating. One approach to solve this problem is the so-called sunray design. For this purpose, a first exposure is performed with a mask without bridges. Then, a second mask with a regular dot design can be used for a second (and even third) exposure before the developing step. During those additional exposures mask and substrate are tilted by a certain angle so that the subsequently exposed support bars fill only a small portion of the total grating height at each location, reducing the negative impact on the performance of the grating [Mohr, 2012b]. Another advantage of the LIGA process for the production of X-ray gratings is the possibility to choose carbon, polyimide or silicon as substrate material. This offers an additional possibility to adapt the grating to the requirements of the imaging setup [Koch, 2015].

The area of the produced gratings is mainly determined by the beamline geometry and is currently limited to 100 mm. However, the gratings commonly fabricated have an area of 50 mm $\times$ 50 mm [Meiser, 2016]. For imaging the field of view should be in the same range as the imaged object, to allow fast image acquisition without later image stitching. For example, to image a whole human torso a field of view in the range of 400 mm $\times$ 400 mm is required. To fabricate the necessary grating areas, several smaller gratings are nowadays stitched together to form one large grating. For example, several gratings can be stitched in series to form a long grating slot whose length covers the entire width of the field of view, but which is only a few centimeters wide at the same time [Schröter, 2017a]. Such a grating slot is sufficient to cover the entire field of view when it is used with a scanning acquisition

procedure [Kottler, 2007]. However, also 2D grating stitching has been demonstrated with an resulting grating area up to 200 mm × 200 mm using 16 individual grating tiles [Meiser, 2016; Schröter, 2017b]. Another method to increase the exposed grating area is the dynamic exposure [Schröter, 2017c]. In this process, a mask is positioned stationary in the synchrotron beam and the substrate with the resist is moved slowly along the mask. The velocity of the substrate is selected in such a way that each point of the substrate is exposed for a sufficiently long time. Thus, the size of the grating can theoretically be increased arbitrarily in at least one dimension, while at the same time only a small mask area is required.

3.2.2 Silicon-based grating fabrication

The second commonly employed group of fabrication methods for X-ray gratings is based on silicon etching. Here, a variety of different methods is available for etching the required structures, as well as different methods for filling the resulting trenches with absorbing materials. This section provides an overview of the current state of the art in silicon-based grating fabrication methods.

Silicon etching

Anisotropic wet etching of silicon takes advantage of the fact that the different crystal planes of silicon are affected to different degrees by an etching solution such as potassium hydroxide (KOH). For instance, the etch rate in the <110> direction of the silicon crystal is about 80× faster in KOH etching than in the <111> direction [David, 2007]. This allows etching of almost perpendicular trenches in silicon wafers with a <110> orientation of the crystal perpendicular to the surface. By precisely alignment of a silicon oxide mask perpendicular to the <111> direction of the crystal, grating structures with high aspect ratios up to 1:80 can be fabricated in this way [Finnegan, 2019].

Another widely used method for etching silicon wafers is reactive ion etching (RIE). In this process, a plasma of reactive ions is accelerated in an electric field and bombarded onto a wafer's surface. A combination of mechanical impact and chemical etching of the ions ablates the surface of the wafer. Using a mask of photo-resist or silicon oxide, precise grating designs can be etched. By repetitively applying this etching process followed by a passivization step, it is possible to etch with high anisotropy, creating deep trenches for X-ray gratings [Romano, 2017b; VilaComamala, 2018; Shi, 2020]. In this case, the process is called deep reactive ion etching (DRIE). The effective height of the grating can be additionally doubled by a second etching process on the backside of the silicon wafer, which is aligned to the front side [Hollowell, 2019]. Moreover, it is possible to etch inclined gratings by distorting the applied acceleration field through field modulators, thus avoiding bending of gratings to prevent shadowing in imaging setups with cone beam geometry [Shi, 2022].

In photo-assisted electrochemical etching, a mask is lithographically applied to an n-type

silicon wafer with <100> orientation. Subsequently, an inverse pyramid structure is created by anistropic wet etching with KOH. The wafer prepared in this way is then placed in a hydrofluoric acid (HF) solution and a low voltage bias is applied via a platinum electrode. By illumination of the wafer backside with visible light (e.g. by a halogen lamp) electron holes are generated in the wafer. Due to the applied voltage bias, these holes start to drift towards the surface of the wafer. In this process, the electron holes first reach the indentations of the inverse pyramid structures and start the HF etching process there. If the voltage bias is chosen small enough, in simplified view all electron holes are consumed there, while the HF concentration in the trenches remains approximately constant [Linnros, 2006]. This results in a selective etching process where the existing trenches become deeper and deeper while the surface of the wafer is not etched. This allows to fabricate grating structures with high aspect ratios [Lei, 2014; Lei, 2016].

In metal-assisted chemical etching, the etching process also takes place in an HF solution containing an additional oxidizing agent. However, the holes required for the etching process are not provided by applying a voltage, but by a metal catalyst that reduces the oxidizing agent. The catalyst is not consumed and sinks deeper into the wafer as the etching process continues, forming deep linear trenches [Han, 2014]. Since the etching process only takes place in the area of the metal catalyst, a large number of structural designs such as X-ray grating, but also zone plates can be produced by patterned deposition of the metal catalyst [Romano, 2017b; Romano, 2020a; Romano, 2020b]. In addition, the metal catalyst left at the bottom of the trenches after etching can be used as a plating contact for eventual metallization of the trenches by electroplating.

Absorber filling

Electroplating

The most commonly used method for the metalization of grating trenches is gold electroplating. In this process, the grating is operated as anode in a gold electrolyte bath. By applying an electrical current via a cathode (usually made of platinum), gold atoms are deposited in the grating structure. However, since silicon itself is not conductive, first plating contacts have to be deposited in the grating structure. If the etching process was performed with metal-assisted chemical etching, the metal catalyst that remains in the trenches after etching can be used for this purpose. If the grating structure was etched with one of the remaining etch methods, various methods are available to selectively deposit gold as plating contacts in the grating trenches.

One method illustrated in Figure 3.3 **a)** first applies a protective cap to the top of the silicon bars by evaporating aluminum onto the substrate at an angle of about 45 °. In a second step, gold is vapor-deposited perpendicularly to the substrate. Afterwards, the aluminum protective cap together with the gold layer on it is removed by phosphoric acid. This ensures that only the gold layer at the bottom of the trenches remains, which can then be used as a starting layer for electroplating [David, 2007].

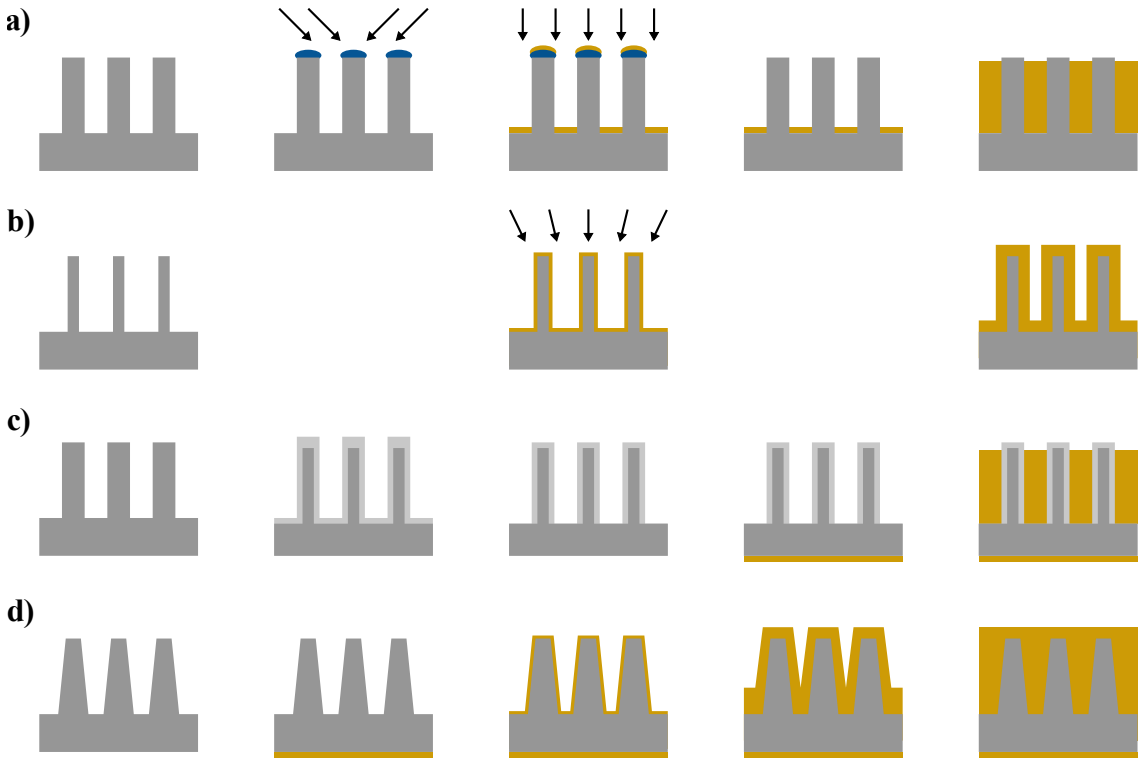

Figure 3.3: Four different approaches for absorber filling of etched silicon grating templates based on electroplating. **a)** First an aluminum protective cape is evaporated onto the silicon bars followed by perpendicular gold evaporation. Then the aluminum is chemically removed and only the gold at the bottom of the grating trenches remains as plating contact for the final electroplating. **b)** A grating template with an adapted DC of 0.75 is first coated with a homogeneous gold layer. In the following precisely controlled electroplating a uniform gold layer is deposited such that the gold thickness on the walls equals one quarter of the etched grating period, causing a frequency doubling of the grating period. **c)** On a low resistivity silicon wafer, an insulating SiO_2 layer is generated by thermal oxidation and additional evaporation onto the top of the grating bars. Before the electroplating is performed, the SiO_2 layer at the bottom of the trenches is removed by DRIE and an optional gold back contact is evaporated onto the backside of the wafer. **d)** An optional gold back contact is deposited onto the backside of a low resistivity silicon wafer with an etched grating structure with a slightly tapered profile. The electroplating starts with the seedless formation of an initial gold layer followed by conformal electroplating to fill up the trenches with gold (figure adapted from [David, 2007; Kagias, 2019; Jefimovs, 2021]).

Another method is shown in Figure 3.3 **b)**. Here, the silicon grating structure is etched with an increased DC of 0.75. The plating contact is then intentionally applied to the walls of the trenches as well, by atomic layer deposition, which is an isotropic process. During a precisely controlled electroplating process, a uniform gold layer is deposited such that the gold thickness on the walls equals one quarter of the etched grating period. In this way, the gold layer at the trench walls serves as absorber and so-called frequency doubling occurs, since the period of the resulting grating is half that of the etched structure. A disadvantage of this method is that gold is deposited not only on the walls of the trenches, but also on the bottom of the trenches and on the top of the silicon bars - both areas where the grating should be as transparent as possible [David, 2007].

Another method is seedless electroplating, based on the fact that silicon becomes conductive as a result of intentional impurities with other elements. Two different approaches for filling the trenches on low resistivity silicon wafers have been reported in the literature. With both, an optional gold layer can be deposited on the backside of the wafer to ensure an ohmic contact to the wafer for electroplating. The first approach (Figure 3.3 **c)**) creates first a SiO_2 layer by thermal oxidation. Additionally, the SiO_2 layer on top of the silicon bars is enlarged by plasma enhanced vapor deposition of SiO_2. Then, using short DRIE, the SiO_2 at the bottom of the trenches is removed, while on the top of the silicon bars and on the walls the SiO_2 layer remains intact. As a result, a conductive contact to the bulk silicon exists only at the bottom of the trenches and the trenches can be filled from there by electroplating [Kagias, 2019]. In the second approach (Figure 3.3 **d)**), the entire surface of the wafer was first stripped of its native SiO_2 layer by HF etching so that the entire wafer surface acts as a plating contact. Conformal electroplating was then used to evenly fill the trenches with gold. Voids in the gold filling could be avoided by a slight tapering of the Si structures produced during the silicon etching and a slow electroplating process at a constant current [Jefimovs, 2021].

Atomic layer deposition

In addition to electroplating, several other alternatives for filling the grating structures were reported. One such method is based on atomic layer deposition (Figure 3.4 **a)**). Here again an etched silicon template with a DC of 0.75 is employed. Instead of gold, however, iridium was used as the absorber. By repeatedly providing the two reaction gases (iridium acetylacetonate and oxygen gas) in alternating pulses, iridium is deposited uniformly on the entire surface of the grating structure with almost atomic mono-layer accuracy [Knoops, 2010]. This allows the process to be controlled in a way that the iridium layer on the walls of the silicon bars equals a quarter of the etched period, thus achieving a frequency doubling of the period [VilaComamala, 2018]. However, the process takes a long time and is quite expensive with both iridium as well as gold. Thus, it can hardly compete with the classic manufacturing processes.

Absorber filling with molten metals

A further alternative is the deposition of absorbing material in a molten state. Several metals and alloys such as lead or an eutectic gold-tin alloy have melting points significantly below that of silicon (1410 °C), so they can be casted into silicon-etched micro structures. In this

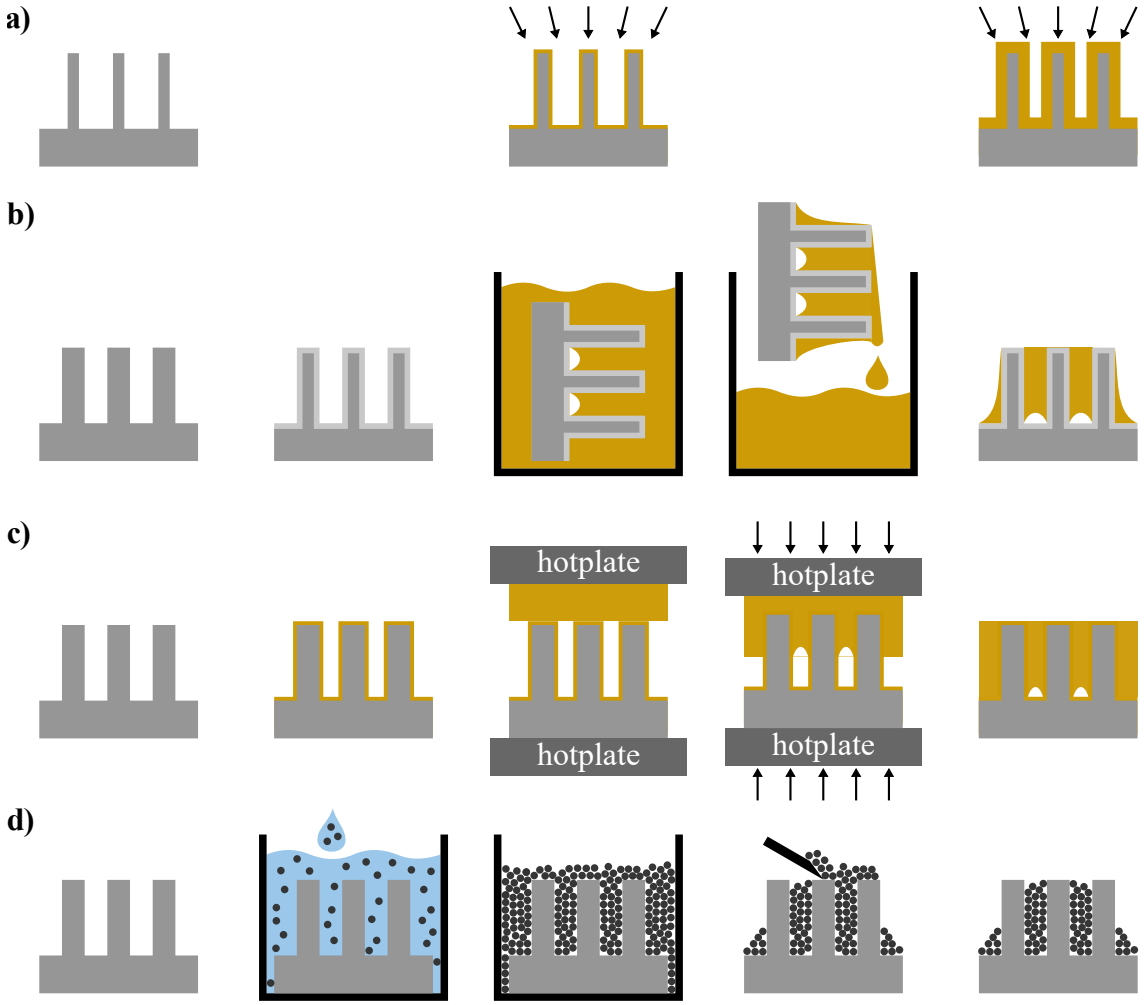

Figure 3.4: Four different approaches for absorber filling of etched silicon grating templates without electroplating. **a)** As in Figure 3.3 **b)**, a grating template with an adapted DC of 0.75 is evaporated with a strongly absorbing material. However, in this method, the entire absorber is applied by atomic layer deposition. In case the grating trenches are filled with molten absorbers, the wettability of absorber and silicon template is crucial. Depending on the absorber used, the surface can be modified, e.g. by oxidation or coating with thin contact layers. **b)** After the surface treatment, in micro-casting the grating template is immersed into a bath of a molten absorber within a vacuum chamber. The molten absorber is drawn into the grating trenches by capillary forces, and after removal from the bath, excess material is removed from the surface. **c)** In hot embossing the grating template is stacked with a thin foil of the absorber and heated from bottom and top. After the foil is melted, the absorber is pressed into the trenches of the grating by applying a high pressure. **d)** In the particle-based absorber filling particles of a strong absorbing material are suspended and applied onto the grating template. After evaporation of the carrier solution the grating surface can be cleaned with a doctor blade (figure partly adapted from [VilaComamala, 2018; Romano, 2017b]).

process, the challenge is that the penetration of liquid metals and alloys into the deep trenches of a grating is determined by their surface tension. Surface treatments or special coatings of the silicon grating templates can reduce the surface tension of the metals, resulting in increased wettability and consequently better filling of the trenches. Therefore, a surface treatment of the silicon structures adapted to the absorber material used is necessary.

When filling the grating structures with molten metals, two different types can be distinguished: micro-casting and hot embossing. Here, the difference lies in the way the liquid absorber is forced into the grating trenches. In micro-casting (Figure 3.4 **b)**), the grating template is immersed in the liquid absorber in a vacuum chamber. After a short time, the liquid absorber is pulled into the trenches by capillary action and surface tension. The filled grating is then removed from the bath and excess material is removed from the surface. In this way, for example, gratings with bismuth (melting point 272 °C) as absorber were fabricated. The surface treatment of the silicon was thereby achieved by controlled oxidation of the silicon [Lei, 2014] and can be further improved by an additional layer of Bi_2O_3 [Lei, 2016]. In this way, gratings with 3 µm period and 150 µm trench depth were filled. However, due to voids, this trench depth does not correspond to the actual absorber height of the fabricated gratings. It is also not known how large the defect density and the produced areas are.

In hot embossing (Figure 3.4 **c)**), the silicon grating and a thin foil of the absorber material are stacked and heated simultaneously from the top and bottom until the foil melts. The liquid absorber is then pressed into the grating trenches by applying a high pressure. Based on this method, the fabrication of absorption gratings made of an eutetic gold-tin alloy was demonstrated. In this case, the surface stress of the alloy was reduced by applying a thin Al_2O_3 layer followed by a second layer of iridium [Romano, 2017a]. However, absorption grating fabrication based on other alloys such as lead-indium and lead-tin-silver have also been successfully demonstrated [Romano, 2017b]. Absorption gratings with periods in the range of 1 µm to 20 µm and aspect ratios up to 50 were demonstrated. However, at such high aspect ratios, collapsed grating lines occur due to the high pressure exerted during the embossing process.

Absorber filling with particles

Another alternative is to fill small absorbing particles into the grating trenches. Empty voids between the particles are acceptable if they are compensated by an increased trench depth. For filling, the particles are suspended in a carrier solution and applied to the grating template and refilled until the trenches are completely filled. After the carrier solution is evaporated particles protruding the grating surface can be removed with a doctor blade (see Figure 3.4 **d)**). Particle-based fabrication of absorption gratings was first demonstrated for neutron interferometers using gadolinium oxysulfide particles [Kim, 2013] and has been optimized down to periods as samll as 13.3 µm [Gustschin, 2018].

The efforts to use particles as absorbing matrix for X-ray applications dates back to 2016 [Gustschin, 2016; Pinzek, 2018] where small grating pieces with 36 µm to 40 µm period were filled up with tungsten particles in two master thesis projects. Independently, absorption grat-

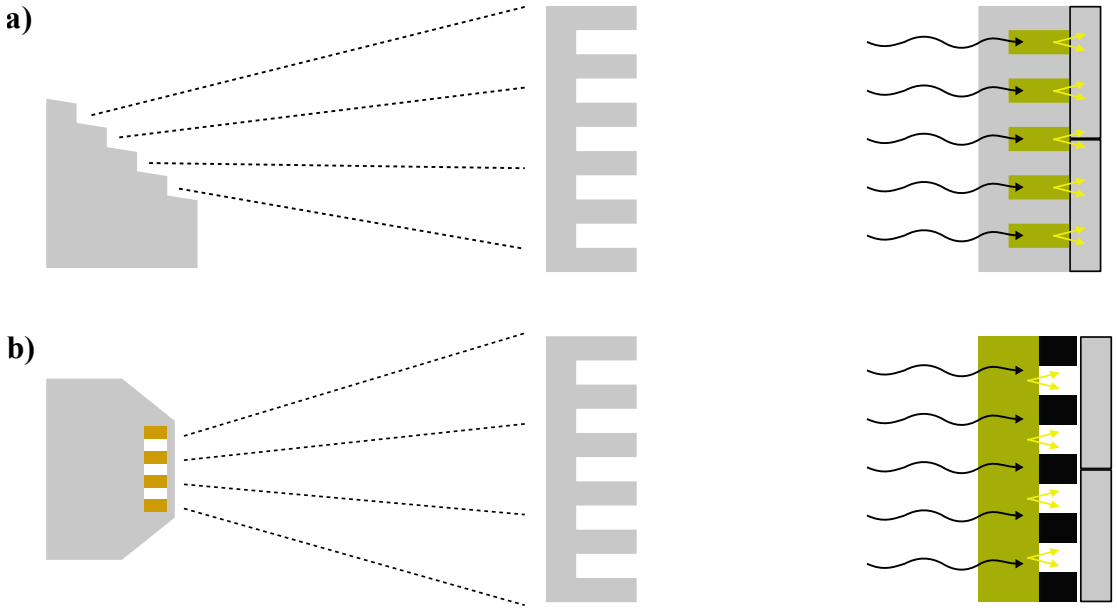

Figure 3.5: Different approaches to avoid high aspect ratio absorption gratings. **a)** The source grating is replaced by a multi-line, ladder shaped anode and instead of an absorbing analyzer gratin a scintillator grating is used [Du, 2011]. **b)** A transmission X-ray tube with a periodically line-patterned metal target on a diamond substrate replaces the source grating [Morimoto, 2014]. Instead of an X-ray absorbing analyzer grating, a visible light absorbing grating is placed behind a thin layer scintillator screen [Kim, 2020] (figure adapted from [Du, 2011; Morimoto, 2014; Kim, 2020]).

ings based on tungsten particles were reported by Lei et al. [Lei, 2019a] and were successfully scaled to 8 inch (200 mm) silicon wafers [Lei, 2019b]. Furthermore, for 8 mm × 8 mm sized gratings the particle filling ratio was improved up to 65% by ultra-centrifugation [Hojo, 2019]. However, in these two publications the aspect ratio has not exceeded 1:5. Furthermore, the demonstrated gratings have a duty cycle (DC, ratio of etched/ absorbing area to period) significantly larger than 0.5 which makes them unfavorable as analyzer gratings for dose-sensitive applications. In chapter 4 of this thesis it is shown that the filling ratio can also be improved by mixing particles of different size. Further the centrifugation approach is translated to larger grating areas.

Alternative methods

Several methods for X-ray phase-contrast imaging have been reported avoiding one or even both absorption gratings. An overview over several of these approaches is given in Figure 3.5.

In grating-based imaging a source grating is required, when the X-ray source does not meet the required coherence (see chapter 2.4.3). In this cases the source grating introduces a multi-

tude of sufficiently coherent sources, to exploit the Talbot effect. However, such a multitude of coherent sources can be also achieved by micro-structured anodes. In one approach a ladder-shaped anode which creates spatially coherent source lines similar to a source grating was used [Du, 2011], as shown in Figure 3.5 **a)**. In another approach is to use a transmission tube with a structured metal target on a diamond substrate [Morimoto, 2014; Zan, 2021] (see Figure 3.5 **b)**). However, especially the transmission tube cannot provide the X-ray flux needed for medical imaging.

Furthermore, approaches to replace the analyzer grating were reported. Instead of an absorption grating a scintillator grating can be used to detect the intensity modulation of the interference pattern [Du, 2011] (see Figure 3.5 **a)**). A grating template, which can be fabricated for example by silicon etching (see section 3.2.2), can be filled with a scintillator material and thus replace an absorbing analyzer grating. Only in the scintillator material, the X-rays are converted into visible light, which can be detected by a visible light CCD detector. However, the X-rays passing through the gratings silicon bars can not be detected by the CCD detector. Therefore, the scintillator grating performs comparable to an absorption grating since only single intensity lines are detected.
However, using scintillator gratings has significant disadvantages compared to absorption gratings. Similar to anti-scatter grids, absorption gratings prevent strongly scattered photons (e.g. due to Compton scattering) from reaching the detector. With a scintillator grating these scattered photons are also detected, leading to a visibility loss and the deterioration of the desired signal. Another disadvantage is that the scintillator material also has to be filled into high aspect ratio structures, since a scintillator thickness in the range of 600 µm is required for a good light emitting efficiency [Kleimann, 2001; Du, 2011]. Therefore, similar challenges for the fabrication of scintillator gratings apply as for absorption gratings.

Another approach to replace the analyzer grating was recently reported for a neutron Talbot–Lau interferometer. The method is based on a thin scintillator in combination with a grating for optical light [Kim, 2020]. The scintillator converts the intensity pattern behind the reference grating into visible light. The amount of visible light in this conversion is proportional to the incoming intensity causing visible light Talbot pattern, which is sampled by the visible light grating.
For the absorption of visible light, significantly lower material thicknesses are required than for the absorption of X-rays. At the same time, the use of strongly absorbing materials such as gold can be avoided. This eliminates the need for high aspect ratio structures, which significantly simplifies grating fabrication. At the same time no shadowing effects appear due to the small absorber height and thereby no bending of the analyzer grating is required. However, typical source to analyzer grating distances are in the range of 1 m and above, in which bending of gratings is feasible without the risk of grating damage. The big disadvantage of this approach is that the visible light is emitted isotropically in the scintillator material. Therefore, the resolution of the visible light Talbot pattern decreases with increasing thickness of the scintillator material. Thus, this approach is limited to scintillator thicknesses smaller than 20 µm [Kim, 2020], which lead to low photon efficiencies and is therefore not suitable for medical systems that use significantly thicker scintillators.

3.3 Grating characterization

The quality of dark-field and differential phase contrast images in a grating interferometer depends strongly on the quality of the used gratings. Therefore, knowledge of the properties and defects of individual gratings is important. The simplest way to characterize a grating is based on the process parameters used in its fabrication (e.g. etch depth, amount of gold electroplated). This allows to estimate important parameters, like the absorber height for absorption gratings. However, only gratings produced with the same fabrication method can be compared directly, as the fabrication methods may differ significantly. In addition, deviations in the manufacturing processes can cause discrepancies between the actual and design parameters. Thus, characterization methods are needed to measure and analyze a grating as it is.

3.3.1 Microscopy methods

The structures of X-ray gratings are in the order of 10 µm, so that the individual grating lamellae cannot be evaluated by eye. Therefore, a high magnification is needed for the analysis of the grating lamellae, which can be achieved by different microscopic methods.

Optical microscopy

In optical microscopy, lenses are used to create a magnified image of an object that can either be seen directly by eye or captured by a camera. For this purpose, the examined object is illuminated either from below the object (transmission mode) or with light coming through the objective also called bright field. Due to the lack of transparency for visible light, only bright field illumination can be used for the analysis of X-ray gratings. The light reflected by the surface is then captured by a objective lens and focused to form a magnified real image. The eyepiece (a second lens or group of lenses) is used to magnify this image further. The total magnification of the microscope is thereby the product of the magnifications of the objective and eyepiece. The resolution that can be achieved with an optical microscope is diffraction-limited and depends on the wavelength of the light used.

The major advantage of optical microscopy for the characterization of gratings is the wide availability of this method. This allows to inspect the surface of a grating with minimal effort. However, only a small part of the grating can be examined at once, so only local information about the grating can be obtained.

Scanning electron microscopy

In scanning electron microscopes (SEM), a thin electron beam is focused and scanned across the object of interest using magnetic coils. When the electron beam hits the object, various interactions are possible, whose detection gives information about the nature of the object. The detected electron current, which originates from re-emitted or back-scattered electrons, determines the intensity value of the corresponding pixels. The resolution of an SEM is thus mainly given by the size of the electron beam and can thus be adjusted almost continuously. To avoid scattering of electrons by gas molecules, the space around the electron optics and the object is evacuated. However, especially at high magnifications, the broadening of the electron beam in the object due to interactions limits the achievable resolution.

Compared to optical microscopy, SEM offers much better resolution, allowing even very small details to be examined. At the same time, this reduces the field of view of the sample even further. Furthermore, it is often not possible to place very large gratings in the sample chamber of an SEM, so that one is either limited to the characterization of smaller gratings, or larger gratings need to be destroyed in order to obtain an appropriate sample size. Although the electron beam penetrates the object under study, only information about the surface of the object is obtained with an SEM due to the very short range of electrons in matter.

X-ray microscopy

Both optical microscopy and SEM provide only surface information about an object. Since X-rays penetrate objects much deeper than visible light or electrons, X-ray microscopy can be used to image the internal structure of an object in a strongly magnified way. Today, different techniques of X-ray microscopy are applied. In a first method, refractive X-ray lenses (e.g. zone plates) are used to focus X-rays to a small spot. This point can be scanned with an object and the intensity transmitted can be recorded by a detector behind the object. Thus, similar to SEM, an image can be calculated whose resolution is determined by the dimension of the focus point. A second way to acquire high resolution X-ray images is based on the shadow projection method. This takes advantage of the fact that in imaging systems with divergent beam geometry objects undergo a geometric magnification (see equation (2.39)). If the object is placed close to the source or the detector is placed far behind the object, high geometric magnifications can be achieved. However, the possible resolution of such an X-ray microscope is limited by the size of the source spot, which is why microfocus tubes are usually employed. Another limitation of the resolution is the point-spread function of the detector. This effect can be reduced by using thin scintilators at the cost of reduced photon efficiency and therefore longer acquisition times.

All these X-ray microscopy methods provide high resolution 2 dimensional images. However, by combining these with computed tomography (CT) by rotating the examined object in the X-ray beam, it is also possible to determine 3 dimensional information. As many projections at different angles are required for the reconstruction of the 3 dimensional image,

the acquisition time is even further extended. Nevertheless, in some cases, high-resolution CT can provide relevant information for the characterization of X-ray gratings.

3.3.2 Interferometer visibility measurements

All microscopic methods have in common that they can usually only be used to examine small areas of a structure and therefore provide limited information about the quality of the entire grating. Therefore, characterization methods to examine gratings on a large scale are needed. One possibility to characterize a grating over a large area is the use of the grating in a grating interferometer (see chapter 2.4). Thereby, the visibility represents an important figure of merit of the interferometer and the used gratings. Here, the characterization can directly take place in the geometry of the later application. However, since the visibility can only be determined for the entire interferometer and not for a single grating, this method is particularly suitable for comparing different gratings with each other. For example, a Talbot-Lau interferometer with a given source and reference grating can be used to directly compare two analyzer gratings. It is important to keep in mind, that source and reference gratings can also have defects, which may also affect the visibility. By replacing individual gratings and comparing the resulting visibility maps, defects can be assigned to individual gratings. Another disadvantage of this method is that individual gratings may be poorly adjusted. This leads to an overall reduced visibility, which may lead to wrong conclusions about the quality of the gratings.

3.3.3 Angular X-ray transmission analysis

Another method to characterize periodic structures with high aspect ratios (i.e. gratings) is the angular X-ray transmission (AXT) analysis [Gustschin, 2019]. It allows to characterize each grating individually on a large area scale based on its locally resolved parameters like absorber height and inclination as well as its DC. Therefore, it overcomes the drawbacks of an characterization in an interferometer (even so the visibility remains an important parameter).

AXT analysis involves recording transmission images of the grating at different rotation angles between incident X-ray beam and grating structures (note that it is not necessary to resolve the grating period). With increasing tilt between incident X-rays and the grating, the detector observes changing transmission values, caused by a changing projected height profile of the grating. The highest intensity is measured for a incidence beam perpendicular to the grating structures (see Figure 3.6 **a**)). Starting from this position, the intensity decreases approximately linearly when the grating is rotated. Comparing the angle at which this maximum intensity is measured between different pixels, the inclination of the grating structure can be detected. Since each point of the grating is imaged at several angles in the AXT measurement, an additional inclination-corrected transmission image of the grating can

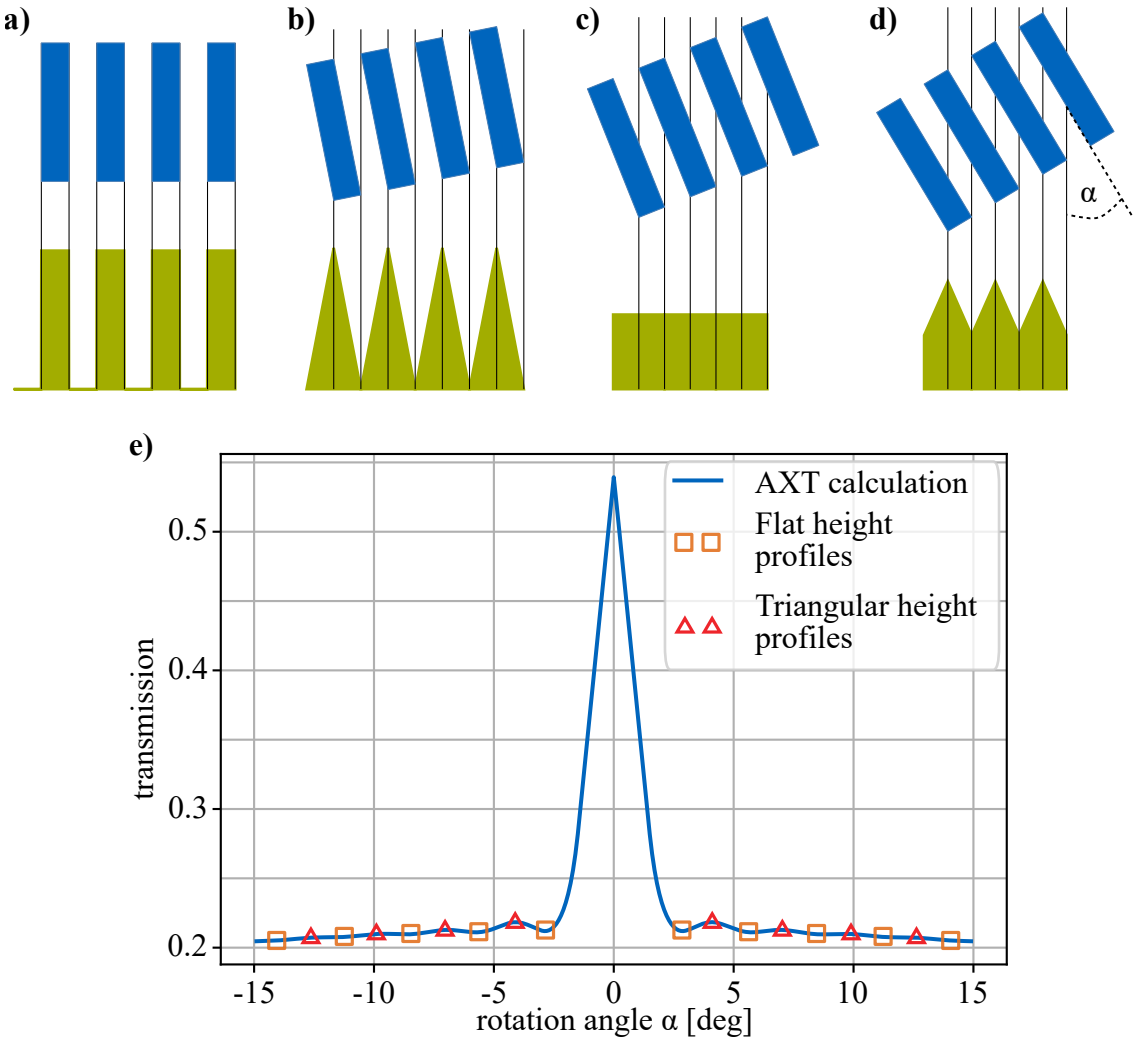

Figure 3.6: Angular X-ray transmission (AXT) analysis for a periodic structure with duty cycle 0.5 and an aspect ratio of 1:5. In **a)**-**d)** several grating rotations α and their respective projected height profiles are given underneath. With increasing tilting of the grating, the height profile changes between flat and triangular shape resulting in a modulation of transmission shown in **e)**. The squares located at the minima of the angular transmission curve indicate the flat height profiles while the triangular height profiles located near the maxima are given by the triangles (figure adapted from [Schüttler, 2016]).

be calculated, in which each point of the grating is illuminated perpendicularly to the local grating structures. Since the transmission depends mainly on the DC of the grating when the X-rays incide perpendicularly to the grating structures, variations in the DC can be detected particularly well in this corrected image. By rotating the grating further from the angle of perpendicular incidence, rectangular, trapezoidal, triangular and flat projected height profiles appear depending on the angle (see Figure 3.6 **b)** - **d)**). Thereby, especially flat and triangular projected height profiles are characterized by minima and maxima, respectively, in the recorded AXT curve (see Figure 3.6 **e)**). Since the angle α_n for the n'th minimum in the AXT curve depends only on the grating period p and height h via

$$\tan \alpha_n = \frac{n \cdot p}{h}, \tag{3.1}$$

the height of the grating structure can be calculated based on the determined minima for a known period. This provides a height map of the grating in which localized variations of the absorber height are observable. Besides this absorber height information, the local absorber inclination can be determined from the angle under which the maximum transmission is observed. Furthermore, a transmission image can be calculated from the data, which corresponds to an image taken in a parallel beam geometry. In this transmission image, variations of the DC are observable. In combination, these data provide a strong basis for assessing the quality of the examined grating.

4 Micro-particle-based absorption gratings

In chapter 3 an overview of the different possibilities to fabricate X-ray gratings is given. This chapter addresses the particle-based approach and develops it further. It is shown that by using a bimodal mixture of particles of two different sizes, the filling ratio of the particles in the grating trenches can be increased. It is additionally known that centrifugation can increase the filling ratio [Pinzek, 2018; Hojo, 2019]. Based on this, it is shown in this chapter that the centrifugal approach can be successfully used with large grating areas up to 170 mm × 38 mm and grating trench depths up to 450 µm. As a result, particle gratings are fabricated that perform comparably to state-of-the-art gratings fabricated by the LIGA process.

Some of the results and findings in this chapter are based on results of the master's thesis *Towards Low Cost and Large Area Grating Fabrication for Grating-based X-Ray Imaging* [Pinzek, 2018] and were already published in *Fabrication of X-ray absorption gratings by centrifugal deposition of bimodal tungsten particles in high aspect ratio silicon templates* [Pinzek, 2022]. Figures and text passages in this chapter may appear identical to the publication. My contribution to this study was the development of the particle filling process, the fabrication of the gratings, as well as the experiments and data analysis for the grating characterization. Compared to [Pinzek, 2018] the particle deposition process was adapted for larger gratings, that have been fabricated via DRIE on 200mm wafers. Compared to previous results the grating area and the depth have been increased and most of the defects that were associated with KOH etching could be avoided.

4.1 Theoretical aspects of particle filling

Filling a volume with particles and optimizing its effective density is subject of numerous theoretical and empirical studies and of interest for many applications such as material sciences, metallurgy, or logistics. The highest possible filling ratio of equal-sized spheres of 74% is achieved by face-centered cubic and hexagonal close-packed arrangement of spheres [Gross, 2014]. This ordered arrangement of spheres can be observed, for example, in the atomic structure of crystals. However, for macroscopic problems a random arrangement is common. For these cases it is known that a volume is filled to about 55% (loose random packing) by equal sized spheres, which can be increased to 64% by external interaction like shaking or applying pressure (random close packing) [Song, 2008]. As illustrated in Figure 4.1, this filling ratio can be increased by using additional spheres with a smaller diameter to fill

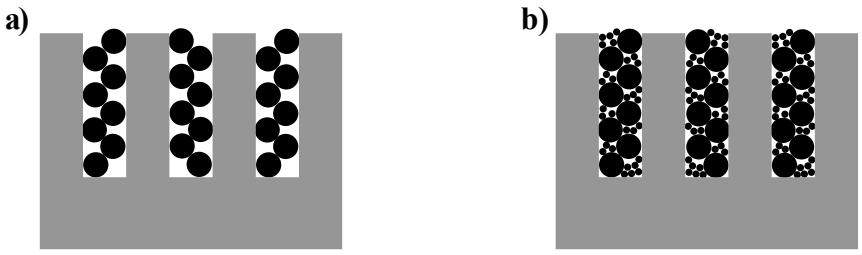

Figure 4.1: **a)** The filling ratio of equal sized spheres in a random loose packing is 55%. **b)** By adding smaller spheres, a bimodal mixture is obtained. The small particles can fill the voids between the large particles and thus increase the filling ratio. (figure adapted from [Gustschin, 2016]).

the voids between the large spheres. Such a mixture of spheres with two different diameters is also called bimodal mixture. In this case the ratio of the sphere diameters and their volume fractions are of importance [Ye, 2018]. The bigger the difference in diameter, the better the voids between the larger spheres can be filled. Typically, the diameters should differ in the range of one order of magnitude or more and the volume fraction of the larger spheres should be in the range of 0.65-0.8 to achieve optimal filling ratios. However, unfavorable effects like walling, loosening, and wedging decrease the theoretical density predicted by simple models. In one such study, the packing has been increased from 53% to 59% by using a bimodal mixture [Ye, 2018].

When high aspect ratio structures are filled additional effects like empty cavities at the trench walls appear, especially when the large spheres are in the same size range as the trench opening. Due to reduced mobility in the trenches, there is more potential to get stuck and prevent other particles to rearrange and find favorable positions. Additionally, it has to be considered that commercially available particles are usually not spherical as assumed by the models. Furthermore, these particles do not have a uniform size, but have a significant size dispersity. In addition, physical and chemical interactions become more relevant at smaller particle sizes so that they can significantly influence the micromorphology.

4.2 Particle-based absorption gratings in literature

First results on particle-based absorption gratings were reported in 2013 by Kim et al. [Kim, 2013] in the field of neutron interferometry. They used a silicon template into which 477 µm wide and 500 µm deep grating trenches with a period of 774 µm were etched by DRIE. To fill these trenches, gadolinium oxysulfide (Gadox) particles with a particle size of 5 µm were suspended in a binder solution consisting of texanol and acrylic resin and poured onto the grating template. Excess particles were then removed from the surface and the taxanol was evaporated in an oven to solidify the binder. This method was successfully adopted by Gutschin

et al. [Gustschin, 2018] to further fill gratings with 13.3 µm period and 80 µm trench depth. Instead of Gadox particles, a metallic gadolinium powder was used whose particles were milled to the required size in a wet milling process and suspended in a binder solution based on poly(vinyl alcohol) (PVA). During the filling process, ultrasound was used to increase the mobility of the particles resulting in improved penetration into the deep trenches. After the gratings dried at ambient temperature, the surface was also cleaned of excess particles. Note that for neutron absorption gratings an effective height of 15 µm Gadolinium is sufficient. Therefore, good performance of particle-based absorption gratings can be reached already with low aspect ratios.

First attempts to fabricate particle-based X-ray absorption gratings dates back to 2016 [Gustschin, 2016; Pinzek, 2018] where small grating pieces with 36 µm to 40 µm period were filled up with tungsten particles in two master thesis projects. In the process, important groundwork was laid for this chapter. Independently, absorption gratings based on tungsten particles were reported in 2019 by Lei et al. [Lei, 2019a]. They filled a silicon grating template with 42 µm period, 31.5 µm trench width, and 150 µm trench depth with tungsten nanoparticles with an average diameter of 50 nm. For the micro-casting process, the particles were suspended in a binder solution consisting of ethanol and the surface active agent OP-10. This particle suspension was then poured onto the grating surface under vacuum conditions, to guarantee a complete trench wetting. Afterwards, the grating was dried at 80 °C to evaporate the binder solution. The method was successfully scaled to an 8 inch (200 mm) silicon wafer and the filling ratio in the trenches was estimated to be 33% [Lei, 2019b] and up to 10% visibility were achieved in a cascade Talbot–Lau interferometer operated at 40 kV tube voltage. Independently, Hojo et al. [Hojo, 2019] also reported a particle-based deposition approach using ultra-centrifugation with 1.5 µm gold particles. For that, the particles were dispersed in water poured over the grating template with a period of 30 µm, a trench width of 20 µm, a trench depth of 67 µm, and an overall grating area of 8 mm × 8 mm. By centrifuging with an centrifugal acceleration of 162000×g the particles were forced into the trenches. After evaporation of water in an oven at 70 °C a particle filling ratio of 65% was estimated by determining the effective gold height from transmission images. However, it remains unclear to what extent this method can be scaled to larger grating areas in view of the large centrifugal accelerations.

As these examples show, the aspect ratios of particle-filled X-ray absorption gratings have not exceeded 1:5 yet. As a result, an effective absorber height (filling ratio × trench depth) of 50 µm has not been exceeded so far. However, for high energy X-ray Talbot–Lau interferometers (eg. for human lung imaging) effective absorber heights in the range of 150 µm and more are required [Sauter, 2019]. Furthermore, the demonstrated gratings had a DC significantly larger than 0.5 which makes them unfavorable as analyzer gratings for dose-sensitive applications.

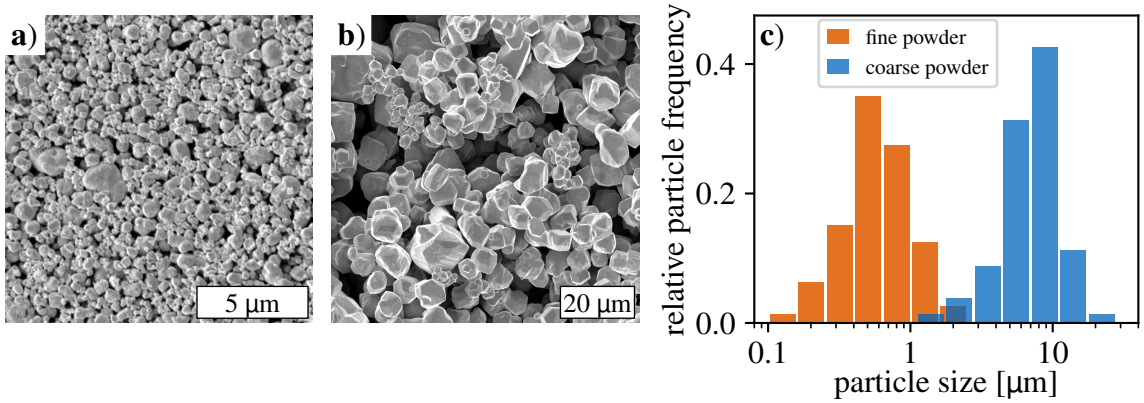

Figure 4.2: SEM images of **a)** the fine and **b)** the coarse tungsten particle powder. **c)** Particle size distribution for both particle powders determined from 40 representative particles for each powder. A mean particle size of $(0.66 \pm 0.35)\,\mu m$ and $(7.7 \pm 3.4)\,\mu m$ is determined for the fine and the coarse tungsten particle powder, respectively (figure adapted from [Pinzek, 2022]).

4.3 Preparation of the particle suspensions

As absorbing material in the following sections two different tungsten powders were used, since tungsten has a high density comparable to gold. Furthermore, tungsten micro-powders are commercially available in different particle sizes at negligible cost compared to gold. Some samples of a fine powder (tungsten, <1 µm, 99.95%) and a coarse powder (tungsten, 12 µm, 99.9%) from Sigma Aldrich (Sigma Aldrich, St. Luis, USA) were prepared to determine their particle size distribution. For that, the size of 40 representative particles from both powders was measured from SEM images. SEM images of both tungsten powders are shown in Figure 4.2 **a)** and **b)** and **c)** provides histograms of the measured particle size distributions. For the fine powder the particle size was estimated to be $(0.66 \pm 0.35)\,\mu m$ and for the coarse powder it was $(7.7 \pm 3.4)\,\mu m$, which is about one order of magnitude larger. Additionally, a bimodal mixture of both powders was prepared with a ratio of 1:2 (fine powder : coarse powder), resulting in a coarse particle weight fraction of 0.67, which is in the optimized range as discussed in section 4.1.

To fill the particle powders into high aspect ratio grating structures they were suspended in a carrier solution. Previous studies have demonstrated that the particle filling ratio can be increased by dissolving a polymer-based binder in the particle suspension [Pinzek, 2018]. For that, Polyvinylpyrrolidone (PVP, $10\,000\,g\,mol^{-1}$, Sigma Aldrich, St. Luis, USA) was dissolved in ethanol with a concentration of $1\,mg\,mL^{-1}$. After evaporation of the ethanol, the PVP polymer serves as a binder fixing the particles in the trenches. Both powders and their bimodal mixture were suspended in the carrier solution with a particle concentration of $0.45\,g\,mL^{-1}$. This results in a tungsten/PVP-weight ratio of 450:1. To prevent particle sedimentation and achieve good mixing, the suspensions were magnetically stirred at 300 rotations per minute.

4.4 Comparison of different tungsten particle fillings

So far, the two tungsten powders have been analyzed only by their surface appearance. In this section, the fine, the coarse, as well as the bimodal mixture of both powders are filled in high aspect ratio grating templates and then compared with each other.

4.4.1 Preparation of small test gratings

For first experiments 10 mm × 10 mm sized grating pieces with a period of 36 µm, a depth of 170 µm, and a DC of 0.6 (trench width of 21.6 µm) were fabricated by DRIE. These small grating templates were filled with particles in a spin dryer centrifuge (oneConcept WS-3500) with a drum diameter of 240 mm. For this purpose, a custom sample container comparable to the one shown in Figure 4.5 **a)** was designed and 3D printed in a way that it can be magnetically attached inside the rotating drum and carries grating piece and particle suspension. To directly compare the filling of the fine and coarse powder, as well as their bimodal mixture, three grating samples were prepared. Each grating template was inserted into a sample container and was wetted with ethanol to prevent air bubbles after the application of the particle suspension. Therefore, no surface treatment was necessary, since the ethanol wetted even deep trenches properly. Thereafter, the particle suspensions were dripped onto the grating structure with a pipette until the container reservoir was filled and the containers were sealed with a lid. Then, the containers were placed in the centrifuge drum. To prevent instabilities and vibrations upon drum rotation, the centrifuge was counterbalanced with an object of comparable dimensions and weight. The centrifugation was carried out for 5 minutes at 2800 rotations per minute, resulting in a centrifugal acceleration of 1050×g. Subsequently, each container was flipped and centrifuged a second time for 5 minutes as the particle concentration tends to increase at the bottom of the vessel due to sedimentation resulting in uneven particle distribution. Afterwards, each container was opened and placed in a fume hood at ambient conditions to evaporate the ethanol over night. Thereafter, the surface of the gratings was completely covered with particles and the gratings were extracted from the containers. Using a razor blade or a scalpel, the surface of each grating was cleaned from excess particles. Note that it is essential to ablate the particle layer moving the blade parallel to the grating lines to avoid any damage to the grating structure.

4.4.2 Characterization of the small test gratings

Methods

For a first impression of the particle shape, size, and morphology in the grating trenches SEM images of the three gratings were acquired with a JEOL JSM-6060LV (JEOL, Freising, Germany) SEM. The respective surface images of the three 10 mm × 10 mm sized gratings are displayed in Figure 4.3 **a) – d)**. For in-depth information of the three particle fillings high-resolution radiographs were acquired with an Xradia 500 Versa X-ray microscope at 100 kV and 70 µA tube parameters and an exposure time of 120 s. By a combination of optical and geometrical magnification, the effective pixel size was 1.04 µm which allowed to resolve the structure well. The obtained images allow a comparison of the attenuation performance of the three different particle fillings. Therefore, the three radiographs were normalized to the transmission signal of the silicon bars and histograms of the pixel transmission values were extracted (Figure 4.3 **e)**).

Results

After the surface cleaning of the gratings almost all particles are removed from the transmitting silicon lines and only a few small residual particles remain on the area that is supposed to be X-ray transparent, as shown in Figure 4.3 **a) – d)**. The fine particle filling (Figure 4.3 **a)**) gives a uniform impression, however, the magnified image in Figure 4.3 **b)** reveals a high porosity of the particle filling. For the coarse particle filling (Figure 4.3 **c)**) also large voids between the particles are visible. These voids are especially located close to the trench walls and it can be expected that their abundance increases with depth as the particle mobility is limited. The interpretation of the bimodal filling (Figure 4.3 **d)**) is difficult, since the fine particles cover the coarse ones hindering an evaluation of the their distribution.

A possibility to compare the average particle absorber density (which is proportional to the particle filling ratio) of the three particle fillings is provided by the X-ray microscopy data. The histograms of the pixel transmission values in Figure 4.3 **e)** show that the fine and the coarse powder filling have comparable transmission (0.4) at the absorbing areas. However, compared to the fine particle filling, the coarse particles histogram has a broader distribution of the transmission values indicating that there are areas with significantly higher or lower filling ratio. The latter might be the case at the trench edges as there are more voids near the trench walls. In comparison to the fine and the coarse particle filling the bimodal filling has a significantly lower average transmission (0.35) and it clearly reduces the fraction of transmission values in the range of 0.4-0.5. This suggests that the finer particles in the bimodal mixture fill voids between the coarse particles. Especially the filled cavities close the edges help to achieve a sharper grating transmission profile. Therefore, in the following sections the bimodal particle mixture will be used for particle deposition.

This suggests that the finer particles in the bimodal mixture fill voids between the coarse

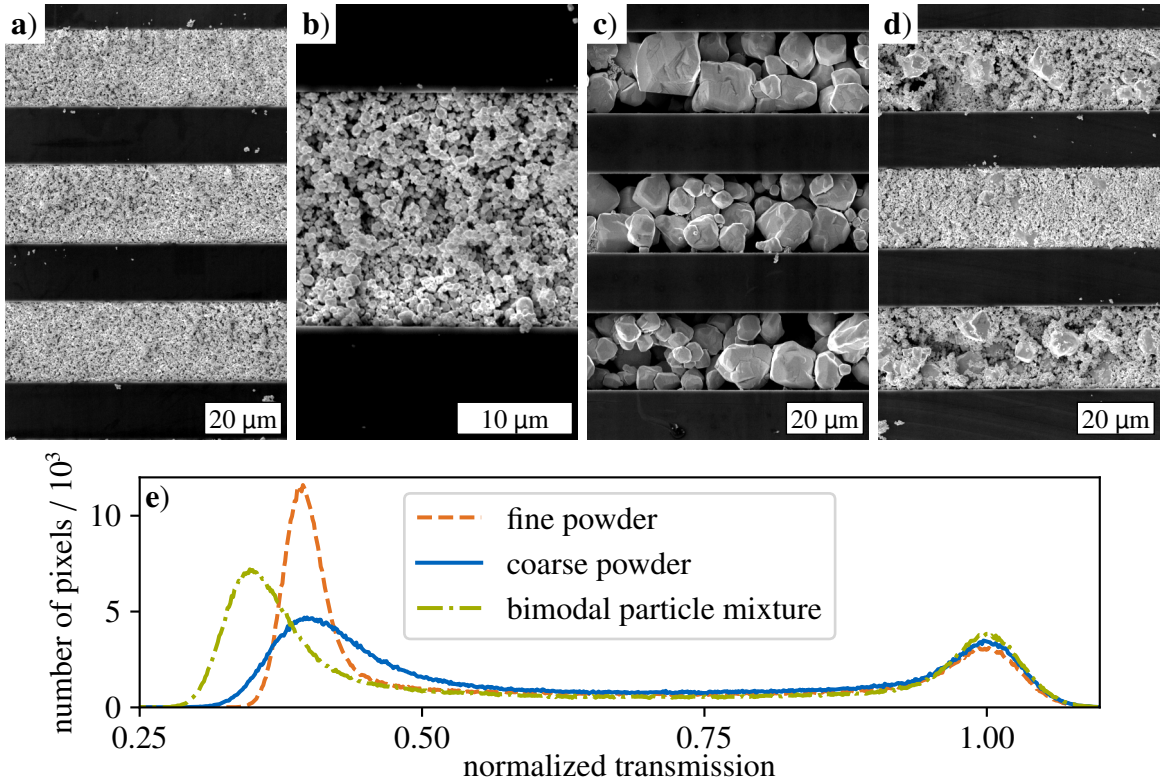

Figure 4.3: SEM images of the 10 mm × 10 mm sized absorption gratings with 36 µm period filled with a) and b) the fine tungsten particle powder, c) the coarse tungsten particle powder, and d) the bimodal mixture of fine and coarse (ratio 1:2) tungsten particle powders. e) Histograms of high-resolution X-ray transmission images of the three gratings normalized to the transmission of the silicon lines (figure adapted from [Pinzek, 2022]).

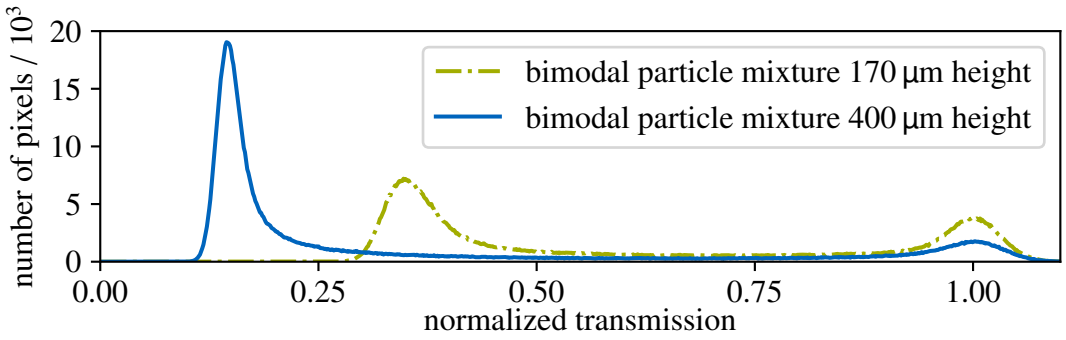

Figure 4.4: Histograms of high-resolution X-ray transmission images normalized to the transmission of the silicon lines for the gratings filled with the bimodal tungsten particle filling with a trench depth of 170 µm and 400 µm, respectively.

particles. Especially the filled cavities close the edges help to achieve a sharper grating transmission profile.

4.5 Increasing trench depth

As shown in the previous section, the bimodal mixture of the fine and the coarse particle powder increases the filling ratio and thus the absorption of the grating lines. However, an average transmission of 0.35 is still to much for high quality absorption gratings. Thus, the next step was increasing the trench depth. A 20 mm × 20 mm sized silicon grating template was prepared next. The template was etched to form 400 µm deep trenches with 40 µm period and a DC of 0.7 corresponding to a trench width of 28 µm. The grating was filled with the bimodal tungsten particle mixture in the same way as described in section 4.4.1. To evaluate the grating high-resolution X-ray radiographs were acquired with an Xradia 500 Versa X-ray microscope with the same parameters as described in section 4.4.2. A histogram of the normalized transmission signal is shown in Figure 4.4. For comparison also the normalized histogram of the previous 170 µm deep grating filled with the bimodal particle mixture is displayed.

The histogram of the 400 µm deep grating shows with an average transmission value of 0.15 a significantly improved absorption compared to the 170 µm deep grating with an average transmission of 0.35. This 20% stronger absorption suggests that the filling ratio can be kept at a high level even for increased trench depths.

4.6 Increasing grating area

After these promising results with the particle based filling approach and the bimodal particle mixture, the next step is focused on scaling the grating area as well as the aspect ratio. The objective is to fabricate an analyzer gratings for a compact inverse Talbot–Lau interferometer system designed for CT application [Viermetz, 2022].

4.6.1 Preparation of large area gratings

Custom-designed grating templates with an active area of 170 mm × 38 mm were acquired from Fraunhofer IPMS (Dresden, Germany), allowing to cover the entire 800 mm analyzer grating slot with 5 individual grating tiles. The templates were fabricated by DRIE on an 8 inch wafer with a period of 45 µm, a DC of 0.54 (which is equivalent to a trench width of 24.3 µm), and a depth of 450 µm. The grating lines are orientated parallel to the short edge of the grating template and the etched trenches are surrounded by 16 mm unetched silicon substrate (see Figure 4.6). Two grating templates (grating #1 and grating #2) were filled with tungsten particles. For further analysis of some local grating defects grating #2 was additionally examined before the particle deposition process. For the particle deposition process a custom centrifuge container (Figure 4.5 **a)**) was designed and 3D printed consisting of a holder with an inner cavity containing an inlay for easier grating extraction after centrifugation. A spacer reduces the reservoir for the particle suspension to the volume above the active grating area. During centrifugation the vessel is closed by a lid with an EPDM seal. The silicon grating templates are inserted into the container between inlay and spacer and are wetted with ethanol as previously described for the small test gratings. Then, the reservoir was filled with the bimodal particle suspension, sealed, and centrifuged in a spin dryer centrifuge (oneConcept WS-3500) two times for 5 minutes after a flip in-between applying the same parameters as described in section 4.4.1. Subsequently, the container was opened to inspect the grating under a microscope. The suspension cleared up as the majority of the particles were deposited into the grating trenches, which were not yet filled completely. The remaining fluid was suctioned with a pipet and the reservoir was refilled with the bimodal particle suspension for a second centrifugation step applying the same protocol. Afterwards, it was observed that the remaining suspension in the container was still turbid, indicating that the trenches were completely filled with particles. Thus, the substrate was allowed to dry overnight leading to a completely covered particle layer on the grating surface. Despite the large grating area, the residual particle layer on the surface could be cleanly removed with a razor blade with relatively low effort in about one hour. A weight increase of the substrate after the particle deposition and the surface cleaning of 13.9 g (grating #1) and 13.5 g (grating #2) was determined, which allows to estimate the particle filling ratio. A photograph of the processed grating #1 is shown in Figure 4.6. Additionally to the large area grating, a smaller edge piece that was fabricated on the same wafer with the same process parameters was filled with the bimodal particle mixture with the same protocol. This piece was cleaved to investigate the grating profile and its filling via SEM.

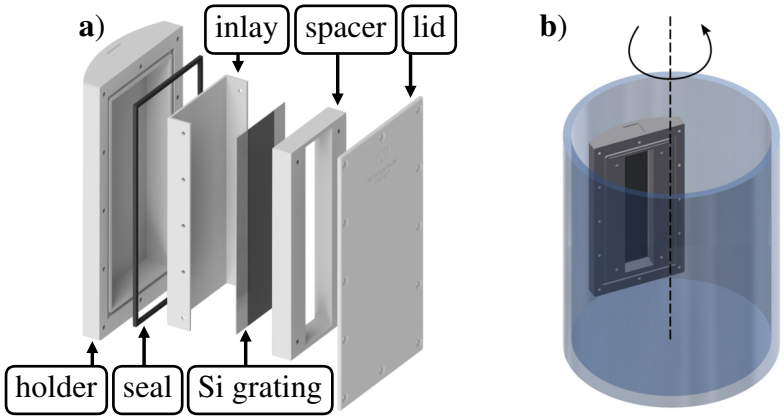

Figure 4.5: **a)** Design of the centrifuge container, built up by a holder with a cavity for the grating inlay and the particle suspension. The inlay helps to remove the grating after centrifugation and the spacer confines the volume in the particle reservoir to the grating area. The lid and the seal close the vessel and prevent leakage. The silicon (Si) grating template is placed between inlay and spacer. **b)** Illustration of the centrifuge container placed in the centrifuge drum. (figure adapted from [Pinzek, 2022]).

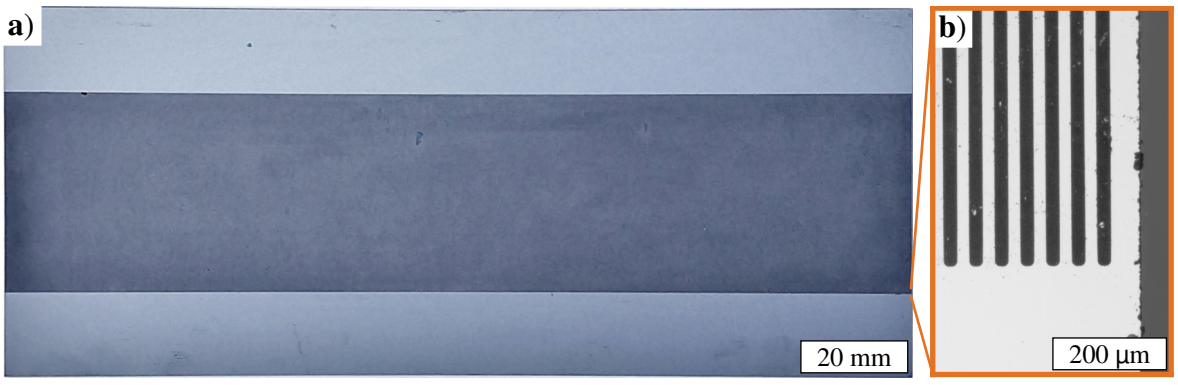

Figure 4.6: **a)** Photograph of the fabricated grating #1 with an active area of 170 mm × 38 mm. **b)** A magnified image of the lower right grating edge acquired with a light microscope. The grating lines are parallel to the short edge of the grating.

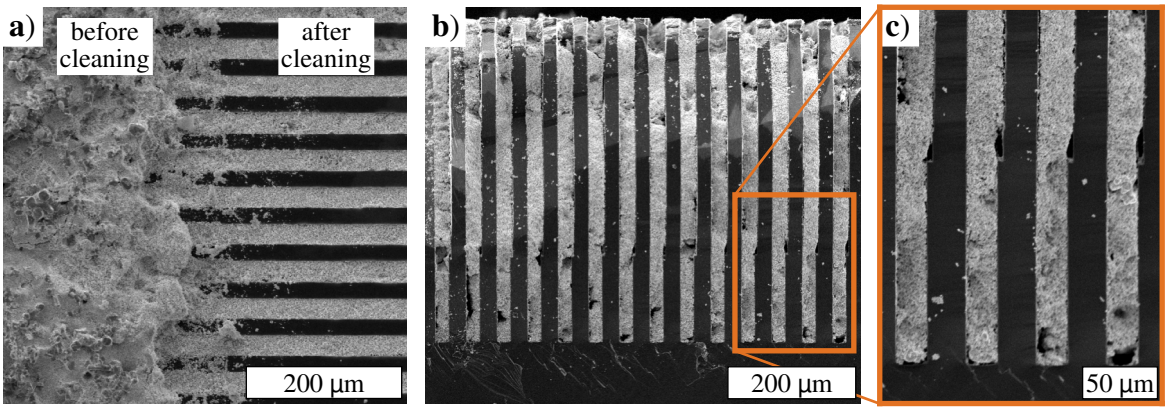

Figure 4.7: SEM images of the small grating piece filled with the bimodal tungsten particle mixture. a) The grating surface is shown after the particle deposition (left) and after removing the protruding particles from the surface (right). b) A cross-sectional view of the grating profile after it has been cleaved, and c) a magnified view of the region in the orange rectangle (figure adapted from [Pinzek, 2022]).

4.6.2 Characterization of a large area grating

The characterization of the large area gratings was performed with different complementary techniques such as SEM, XRM, AXT and a visibility analysis in a compact Talbot–Lau interferometer. This methods provide a wide and comprehensive characterization of the fabricated gratings from the micrometer scale to its large-area properties.

Methods

To investigate the particle filling of the gratings, the small edge piece was examined by SEM. Figure 4.7 **a)** shows a comparison of the grating surface before and after the removal of the residual particle layer. After surface cleaning, this small grating piece was cleaved to obtain a cross-sectional view of the particle filling. Figure 4.7 **b)** shows the grating profile with the filled trenches and a magnified view of the orange rectangle is provided in **c)**.

Further, the large grating #1 was directly compared with a state-of-the-art gold (Au) LIGA grating (microworks GmbH, Karlsruhe, Germany) with 280 µm absorber height, 45 µm period, and a DC of 0.54 fabricated on a graphite substrate. XRM images of both samples were acquired with an Xradia 500 Versa X-ray microscope at 80 kV and 5.5 W with an exposure time of 45 s. The XRM system in this configuration had a resolution of 3.8 µm (full width at half maximum of the line spread function) as determined from an error function fit of an absorbing edge. Since both gratings have different substrates and thus slightly different transmittance on the transparent lines, the transmission images were normalized to their maximum values. The transmission images of both gratings are provided in Figure 4.8 **a)** and **b)** and a line plot of the normalized transmission is plotted in **c)**.

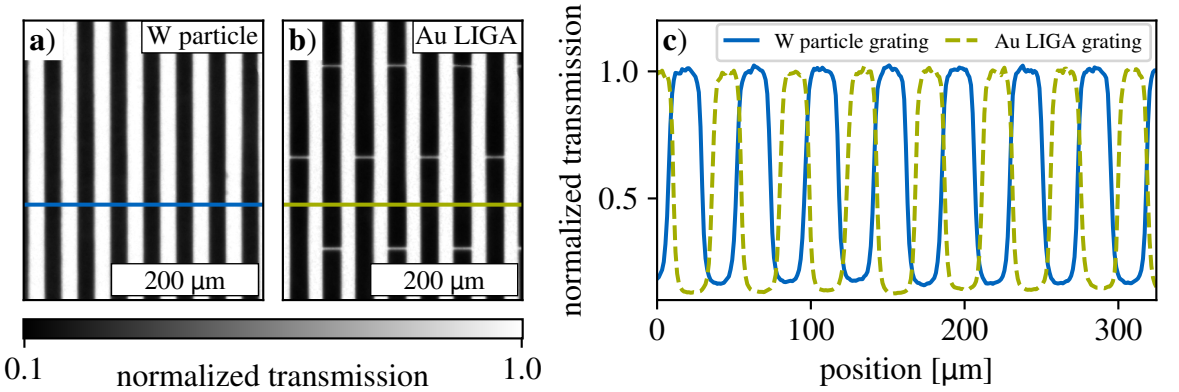

Figure 4.8: Normalized high-resolution transmission images of a) the 170 mm × 38 mm sized grating #1 filled with the bimodal tungsten (W) particle mixture and b) of a state-of-the-art gold (Au) LIGA grating for comparison. c) Line plots of the normalized transmission for both gratings along the colored lines in a) and b) (figure adapted from [Pinzek, 2022]).

AXT analyses [Gustschin, 2019] of grating #1 and grating #2 were performed using a phoenix|X-ray v|tome|x (General Electrics) microCT system, to investigate the grating quality over the entire surface of the large grating. For that, 800 transmission images were acquired while the grating was rotated over an angle range of ±40°. During this acquisition, the tube was operated at 80 kV tube voltage and 75 µA tube current, and the exposure time was set to 6 s. From this set of images the grating transmission was determined (see Figure 4.9 **a)** with a respective line plot in **b)**) over the entire area without shadowing artifacts that typically arise with cone-beam systems when the gratings are not bent to the respective radius. The transmission image is sensitive to DC variations, poorly filled trenches, or defects in the grating structure [Gustschin, 2019]. Additionally, the angular data allows to reconstruct a spatial height map of the grating, which is provided in Figure 4.9 **c)** with a respective line plot in **d)**.
In addition, for grating #2 an AXT analysis was performed before particle deposition (also 800 images in the range of ±40°). This takes advantage of the fact that the silicon lines of the template absorb X-rays stronger than the air within the grating trenches. However, since silicon absorbs much weaker than the tungsten absorber of the final grating, the tube voltage was reduced to 40 keV. The anode current was 45 µA and the exposure time 10 s. From these two measurements, a cone-beam corrected transmission image (normalized with the transmission value of the solid silicon grating edge) and the height map of the grating before and after the filling of the grating were calculated, respectively (see Figure 4.10).

A final characterization of the grating #1 was performed in a compact Talbot-Lau interferometer with an inverse grating geometry designed for clinical X-ray dark-field CT. Such setups allow to use analyzer gratings with relatively large periods and therefore reduce the requirements for the aspect ratio [Donath, 2009]. At the same time, the geometry requires relatively small G_0 and G_1 gratings with high aspect ratios. The grating parameters and the used hardware are given in Table 4.1 and more information on the design can be found in

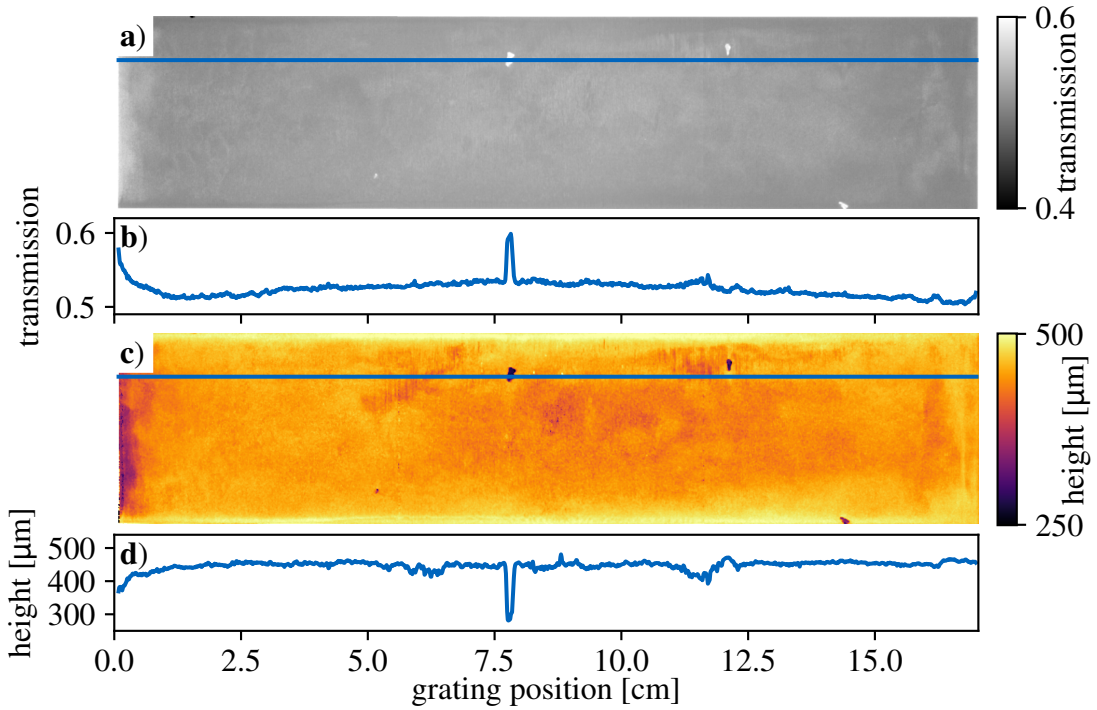

Figure 4.9: Angular X-ray transmission analysis results for grating #1 filled with the bimodal tungsten particle mixture. a) Transmission image that has been virtually recorded with a parallel beam geometry and c) the geometrical height image. Corresponding line plots along the blue lines are given in b) and d) (figure adapted from [Pinzek, 2022]).

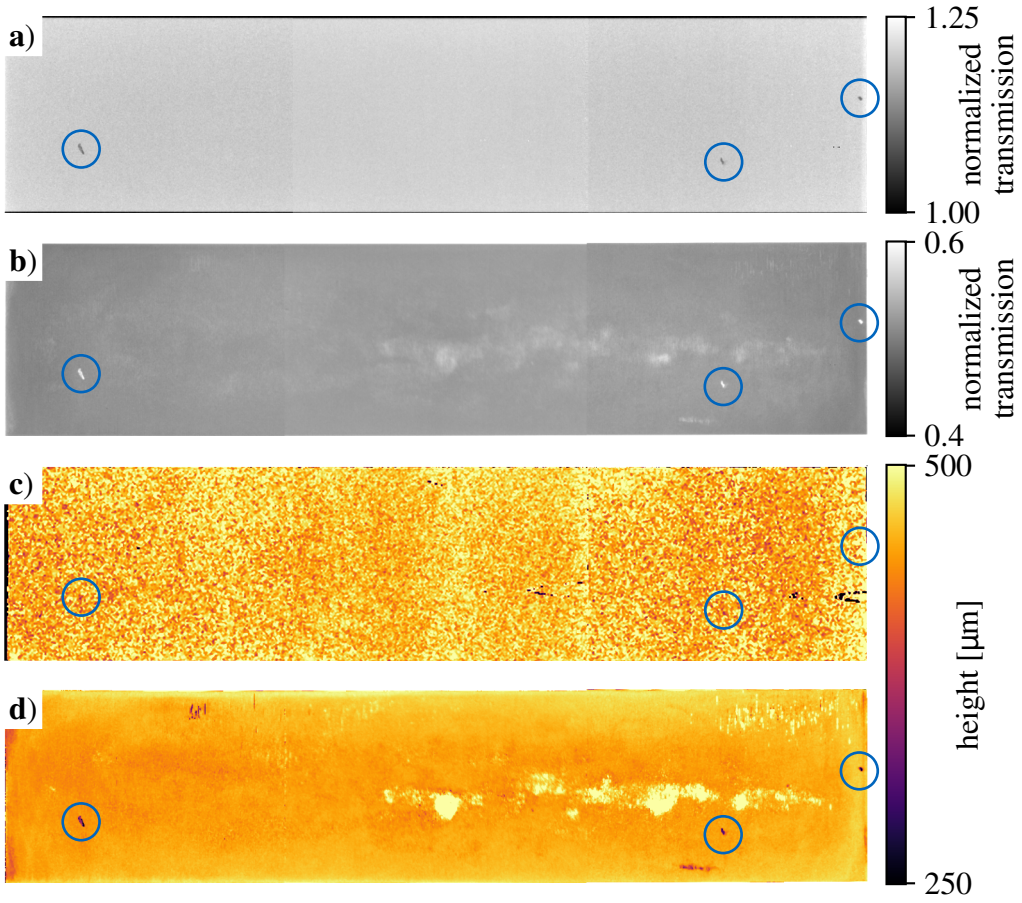

Figure 4.10: Angular X-ray transmission analysis results for grating #2 before and after filling with the bimodal tungsten particle mixture. **a)** and **c)** Transmission image and height map of the empty silicon grating template. **b)** and **d)** Transmission image and height map of filled grating. The blue circles mark local defects similar to the ones visible for the first large tungsten particle grating in Figure 4.9.

Parameter	W particle grating #1	Au LIGA grating
X-ray source	XWT-160-CT, X-rayWorX	
X-ray filter	3 mm Al + 0.5 mm Mo	
Source-G_0 distance / bending radius	$\approx$ 100 mm	
G_0 (period / DC / height)	4.8 µm / 0.5-0.6 / 280 µm Au	
G_1-source distance / bending radius	$\approx$ 200 mm	
G_1 (period / height)	4.34 µm / 18.5 µm Au triangular	
G_2-source distance / bending radius	$\approx$ 1000 mm	
G_2 (period / DC / height)	45.0 µm / 0.54 / 450 µm effective height 207 µm W	45.0 µm / 0.54 / 280 µm
Phase stepping	G_2, 45.0 µm range, 11 steps	
Source-sample distance	$\approx$ 580 mm	
Detector	XRD 4343CT (Varex) - 2 s exposure time	
Visibility 60kV	(33.6 ± 1.4) %	(32.4 ± 1.1) %
Visibility 70kV	(26.0 ± 1.3) %	(28.7 ± 1.3) %
Visibility 80kV	(21.1 ± 1.2) %	(23.5 ± 1.3) %

Table 4.1: Experimental parameters and results of the Talbot-Lau interferometer used for visibility comparison and imaging. The $\pm$ sign indicates the standard deviation of the visibility.

a recently published article [Viermetz, 2022]. The described geometry of the clinical X-ray dark-field CT was replicated in a laboratory setup to characterize the grating at a high resolution. The visibility of the interferometer with the large W particle grating as analyzer grating was determined at 60 kV, 70 kV and 80 kV tube voltage at 40 W tube power. The X-ray source was filtered with 3 mm of aluminium and 0.5 mm molybdenum to obtain hard X-ray spectra similar to medical CT applications. For comparison also the visibility with a gold LIGA grating (microworks GmbH, Karlsruhe, Germany) as analyzer grating was determined at identical tube parameters. Figure 4.11 **a)** shows the visibility map with a respective line plot in **b)** acquired at 60 kV. Histograms of the achieved visibilities using the W particle grating at different tube voltages are shown in Figure 4.11 **c)**. For comparison, visibility histograms using the gold LIGA grating are displayed for the same tube voltages. Further, a sample composed of different nuts (see Figure 4.12 **a)**) was imaged with the W particle grating as G_2 at 60 kV tube voltage and processed with an expectation-maximization-assisted sinusoidal least square fitting. The transmission, the dark-field, and the differential phase images shown in Figure 4.12 **b) – d)** respectively are stitched together from 3 individual images which were stepped in height, as the sample did not fit into the field of view in vertical direction.

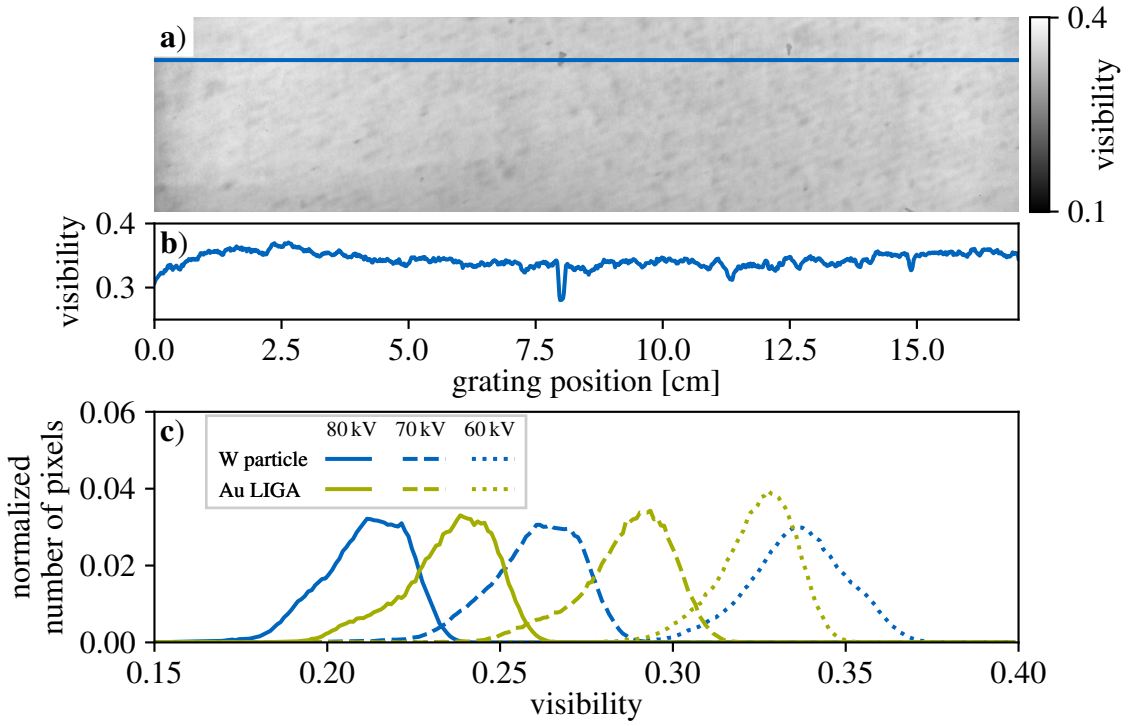

Figure 4.11: Characterization of grating #1 in an X-ray grating interferometer. a) Visibility in a Talbot-Lau interferometer for X-ray dark-field computed tomography, in which the large tungsten (W) particle grating was employed as G_2, at 60 kV tube voltage and b) the corresponding line plot along the blue line in a). c) Visibility distribution of the interferometer using the W particle grating (blue) and a state-of-the-art gold (Au) LIGA grating as G_2 at 80 kV (solid line), 70 kV (dashed line), and 60 kV (dotted line) tube voltage (figure adapted from [Pinzek, 2022]).

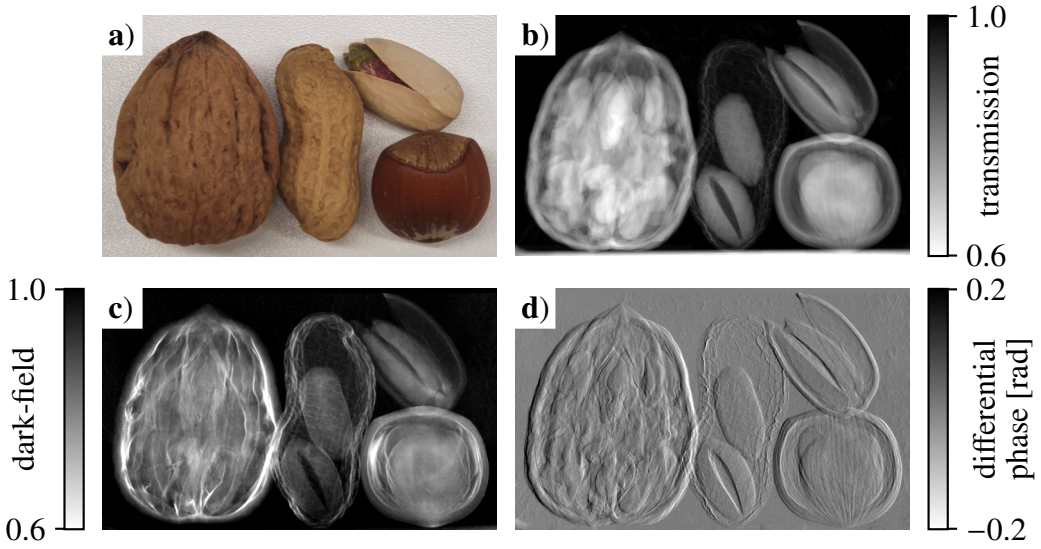

Figure 4.12: Imaging example using grating #1 as analyzer grating in an X-ray grating interferometer. a) Photograph of the imaged nuts, namely a walnut, a peanut, a pistachio, and a hazelnut. b) Transmission image, c) dark-field image, and d) differential phase image of the four nuts acquired at 60 kV tube voltage (figure adapted from [Pinzek, 2022]).

Results and discussion

The SEM images in Figure 4.7 show that the tungsten particle mixture covers the trenches throughout the entire depth of 450 µm. Several larger bubble-like voids are visible, however, it is difficult to tell how much of them were created due to the breaking of the substrate to visualize the profile. The average DC of the grating was estimated to 0.54 from measuring the trench opening at different depths of the grating. The XRM measurements of the grating #1 (Figure 4.8 **a)**) show a well-defined linear pattern with sharp edges comparable to the gold LIGA-fabricated grating (Figure 4.8 **b)**). The comparison of the line plots of the transmission profiles in Figure 4.8 **c)** reveals 16% and 13% residual transmittance on the absorbing areas for the W particle grating and the gold LIGA grating, respectively. This slightly better absorption performance of the gold LIGA grating is expected, as its attenuating lamellae have a significantly higher effective thickness. However, the gold LIGA grating has X-ray transparent resist stabilization structures ('bridges') between the transmitting lines as seen in Figure 4.8 **b)**. These transparent bridges reduce the performance of the absorption gratings especially at smaller periods when the fraction of bridge-related transparent area becomes relatively high. Using silicon-based grating templates usually allows avoiding such unfavorable structures.

As a next step, a large area characterization of the grating structures is necessary to confirm that the presented deposition process can be conducted homogeneously over the entire active area without damaging the fine grating structure. The AXT analysis shows that the grating #1 transmission (Figure 4.9 **a)**) is mostly uniform between 0.5 and 0.55 over the entire grat-

ing area. Only a slight increase is recognizable at the left edge and some local defects with an increased transmission are present as depicted by the line plot in Figure 4.9 **b)**. At the same time, the heightmap (Figure 4.9 **c)**) shows a reduced height on the same spots. The line plot of the height (Figure 4.9 **d)**) shows a reduction to slightly below 300 µm at the defect in the middle of the grating and a reduction to 380 µm on the left grating edge. Note here that the AXT analysis provides the filled height of the grating structure [Gustschin, 2019] and not the effective height, which denotes the thickness of the absorbing material. The area with a reduced transmission on the left might be caused by insufficient filling during centrifugation. As the grating is placed into the insert with the particle reservoir, the bottom area might be blocked by larger particles which sediment much faster and compromise the penetration of smaller particles into the trenches. Similar local defects, with increased transmission and reduced height, are also visible in the AXT analysis of grating #2 (see blue circles in Figure 4.10 **b)** and **d)**). At the same time, these locations in the transmission image of the grating before the particle deposition (Figure 4.10 **a)**) are characterized by reduced transmission. Hence, these spot-like defects are not voids in the trenches but deficiencies in the etched grating template and can therefore not be filled. Overall, an average height of 450 µm particle filling in the trenches is observed for both large area gratings which coincides with the design values.

Considering the local height distribution for each pixel, the DC of 0.54, and a weight increase after particle deposition (13.9 g) an average filling ratio of 46.6% can be estimated for the first large area grating. This is significantly higher than a recent work with a slightly larger trench width by Lei et al. [Lei, 2019b] estimating 33% filling and lower than the ultracentrifugation approach reporting 64% by Hojo et al. [Hojo, 2019] with a slightly smaller trench width compared to the grating presented here. However, the aspect ratio is significantly increased compared to the recent publications resulting in an average effective tungsten filling of 207 µm. Furthermore, it was shown that a centrifugation approach - albeit at a much lower rotation speed - can be also realized with much larger grating areas compared to [Hojo, 2019].

The final characterization of grating #1 performed in a Talbot–Lau interferometer yields a homogeneous visibility map (Figure 4.11 **a)**) and an average of 33.6% at 60 kV tube voltage. The local defects discussed before degrade the visibility to about 28% as denoted by the line plot in Figure 4.11 **b)**. Some further spots with reduced visibility are visible in the visibility image, which are not apparent in the transmission image from the AXT analysis (Figure 4.9 **a)**). Those are caused by grating defects in the G_0 and G_1 gratings since they were also present with the gold LIGA grating. Histograms of the visibility images for the tungsten particle grating as well as the gold LIGA analyzer grating show an visibility increase with decreasing tube voltages (Figure 4.9 **c)**). This is expectable as the gratings become more transparent with higher X-ray energies. The comparison reveals that both analyzer gratings perform comparable at 60 kV, even so the tungsten particle grating achieves a slightly higher average visibility. This might be explained by the bridges present in the gold LIGA grating diminishing their performance compared to the tungsten particle grating. However, for higher tube voltages the gold LIGA grating performs better, since at higher energies the significantly higher absorption thickness of the gold bars (280 µm) and its stronger attenuation

coefficient compared to tungsten absorb better. Overall, the visibility performance of both gratings differs only in the range of a few percent. An imaging example (Figure 4.9) using the fabricated tungsten particle grating at 60 kV tube voltage yields excellent, artifact-free images confirming their applicability for hard X-ray phase-contrast and dark-field imaging.

4.7 Summary

A method to deposit tungsten micro-particles as absorber material into high aspect ratio grating structures by centrifugation is successfully introduced. This allows using conventional micropatterning and etching technologies such as UV-lithography and DRIE (available up to 300 mm wafers) to fabricate grating templates without the need for further special processing steps like seed layer deposition and electroplating. The particle deposition process itself does not require controlled environment and sophisticated equipment and allows to use significantly cheaper alternatives to gold as absorber material. Tungsten is commercially available in a high variety of powders due to its wide applications in metallurgy and provides a similar density as gold. Its lower K-absorption edge at 69.5 keV might also be considered as an advantage compared to gold, however, will only play a considerable role for systems with significantly higher design energy than the system presented here. Furthermore, it is demonstrated that a bimodal particle mixture improves the filling ratio compared to a coarse or fine powder only.

In process of this chapter, the fabrication process is successfully adapted to improve the absorber height, as well as the grating area leading to a 170 mm $\times$ 38 mm sized grating with a particle filling ratio of 46.6% and an effective tungsten height of 207 µm. The latter clearly exceeds recently reported studies [Lei, 2019a; Lei, 2019b; Hojo, 2019] and allows the grating to be used for hard X-ray applications. In a direct comparison with a LIGA-fabricated gold grating conducted in an inverse, compact Talbot–Lau setup similar visibilities were reached.

5 Grating fabrication at a conventional X-ray tube

In this chapter, the fabrication of X-ray gratings is addressed using the LIGA approach introduced in section 3.2.1. In contrast to the classical LIGA approach, the aim here is to adapt the deep X-ray lithography step in such a way that it can be implemented on conventional X-ray tubes. As X-ray tubes are more widely available than synchrotron sources, this will allow to overcome the strong dependence of X-ray grating fabrication on large synchrotron facilities.

Some of the results and findings in this chapter were previously published in *Fabrication of x-ray absorption gratings via deep x-ray lithography using a conventional x-ray tube* [Pinzek, 2021a]. Figures and text passages in this chapter may appear as in this publication. My contribution to this study was the realization of the exposures for the deep X-ray lithography process, the characterization of the fabricated grating structures and the further development of the exposure setup based on the obtained findings.

5.1 Previous results

The application of conventional X-ray tubes for X-ray lithography has already been evaluated in previous studies. Even before the 1980s, soft X-rays generated by X-ray tubes with rhodium, palladium, aluminum, silicon, or carbon anodes were applied to produce structures as small as 17.5 nm by X-ray lithography [Smith, 1980]. Since these anode materials possess fluorescence lines below 4 keV, these early applications are particularly suitable for exposure of thin resist films as used in the semiconductor industry.

At these low radiation energies even thin resist films absorb a large fraction of the radiation. Therefore, these anode materials are not suitable for deep X-ray lithography where significantly thicker resist films are required. To deposit sufficient dose in the bottom region of up to several hundred µm thick resist layers without overexposing the upper regions of the resist, energies above 5 keV are required. Hence, for deep X-ray lithography, anode materials such as chromium, iron, cobalt, nickel, copper, and tungsten are more suitable as they possess fluorescence lines between 5 keV and just above 10 keV [Gustschin, 2016]. Another important aspect, besides the anode material, is the choice of the acceleration voltage. Increasing the tube voltage increases the maximum energy of the X-ray spectrum, and also increases the intensity. This increase is particularly dominant in the low-energy part of the spectrum. Thus, in case of a copper anode, increasing the tube voltage from 20 kV to 60 kV

can increase the absorbed dose in the resist by a factor of 2.6, while at the same time the mean absorbed energy increases by only 0.5 keV [Gustschin, 2016]. This allows to reduce the required exposure time significantly. Another important influence on the exposure time is the flux of the source, which can be increased by increasing the tube power, i.e., the tube's anode current. However, this can also enlarge the source spot, resulting in increased blurring of the mask features. To counteract this dose blurring in the resist, the distance between the source and the mask can be increased, as this reduces the projected source size in the resist. However, this would increase the exposure time significantly, since the flux of a divergent source decreases with the inverse-square law. Nevertheless, simulations have shown that even with source spots larger than 1 mm, mask features with the size of 5 µm can be transferred into several hundred µm thick resist layers if an exposure distance around 30 cm is chosen [Pinzek, 2018].

In first experiments, a 8 mm × 8 mm large area was successfully exposed at a rotating anode X-ray tube with a molybdenum target. A mask with 68.72 µm periodicity was used which was placed together with the photo resist coated substrate at a distance of 10 cm from the source spot. The exposure was then performed for 10 hours at a tube voltage of 28 keV and an anode current of 70 mA. Although the characteristic fluorescence lines of molybdenum at 17.5 keV and 19.6 keV are well above the optimal range of 5 keV to 10 keV, the substrate with a 250 µm thick resist layer (MR-x 50) was successfully developed and electroplated with gold [Gustschin, 2016].

5.2 Setup requirements

In the past, deep X-ray lithography was successfully established at synchrotron facilities and particularly in the field of X-ray grating fabrication many optimizations where introduced [Mohr, 2012a; Kenntner, 2012; Meyer, 2014; Koch, 2015; Schröter, 2017c]. Therefore, the aim of this chapter is to maintain as many established process steps as possible. However, conventional X-ray tubes introduce several challenges for deep X-ray lithography which will be addressed in this section.

A key difference between synchrotron sources and conventional X-ray tubes is the provided X-ray spectrum. Figure 5.1 **a)** displays the X-ray spectrum commonly used for exposure of the epoxy-based resist with heights from 100 µm to 1500 µm at the Karlsruhe Research Accelerator (KARA) synchrotron facility in Karlsruhe. This synchrotron operates at 2.5 GeV and the deep X-ray LIGA beamline LIGA2 is implemented at a 1.5 T dipole magnet. To cut off the high energy part of the continuous spectrum, a nickel mirror (4.85 mrad) is placed between the magnet and the exposure station. Using this spectrum for resist exposure, the majority of the dose is deposited in the energy range from 5 keV to 15 keV. As a result, at 10 keV the relative accumulated dose reaches a value of 0.8, as can be seen in Figure 5.1 **b)**. For comparison, the spectrum of a tungsten X-ray tube at 40 kV tube voltage is displayed in Figure 5.1 **a)**. As mentioned in the previous section, the tungsten fluorescent L-lines with 8.4 keV, 9.7 keV, and 11.3 keV [Attwood, 1999] are located in the same energy range. To

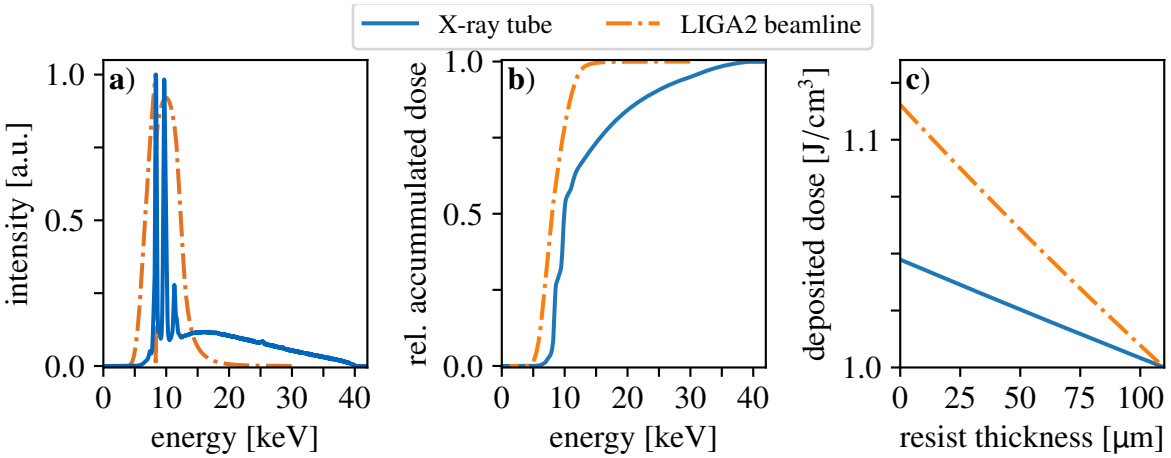

Figure 5.1: **a)** Normalized spectra entering at the surface of the resist for a tungsten anode X-ray tube operated at 40 kV tube voltage and for the LIGA2-Beamline at KARA synchrotron facility. **b)** Ratio of the accumulated deposited dose to the total deposited dose as a function of the energy at a resist depth of 55 µm for both spectra. **c)** Deposited dose in the 110 µm thick resist layer calculated for a bottom dose of 1 J cm^{-1}. (figure adapted from [Pinzek, 2021a]).

obtain a high flux in the range of the L-lines and at the same time to keep negative effects at higher energies due to secondary radiation low [Pantenburg, 1995], here a tube voltage of 40 kV is selected. Its relative accumulated dose (Figure 5.1 **b)**) is shifted to higher energies compared to the LIGA2 beamline, reducing the possible resolution of small structure features [Griffiths, 2004]. However, for grating structures with periods of several µm this should only lead to slight deviations of the duty cycle which is given by the fraction of the absorbing area. Figure 5.1 **c)** presents the calculated deposited dose in a 110 µm thick resist layer over the resist height for the two spectra. The top-to-bottom dose ratio is comparable for both spectra and should therefore not be the limiting factor for DXRL at X-ray tubes.

In contrast to synchrotron sources, X-ray tubes deliver a much lower flux. In addition, the flux decreases with increasing distance from the source (inverse-square law), since the radiation is emitted in a divergent cone geometry. Hence, the exposure distance should be kept as small as possible. At the same time, conventional X-ray tubes have comparably large source spots, resulting in diffuse dose deposition in the periphery of the exposed area defined by the shadow mask. Thus, a trade-off is needed between exposure time and the influence of the source spot. Short exposure distances result in a strong cone geometry of the radiation which causes increased absorption at the edges of the mask, since the radiation hits the absorber structures non-perpendicular (shadowing). Further, the tilted incidence of the radiation at the edges of the mask causes an inclined structure orientation with respect to a line which is perpendicular to the substrate (see Figure 5.2 **a)**). In the course of this chapter, the exposure geometry is adjusted in a way that both mask and substrate are bent cylindrical with the source spot in center, as illustrated in Figure 5.2 **b)**. This avoids shadowing at the edges of the mask and the irradiated resist structures are oriented perpendicular to the substrate (Figure 5.2 **c)**), as it is for DXRL at synchrotron sources. However, bending is only

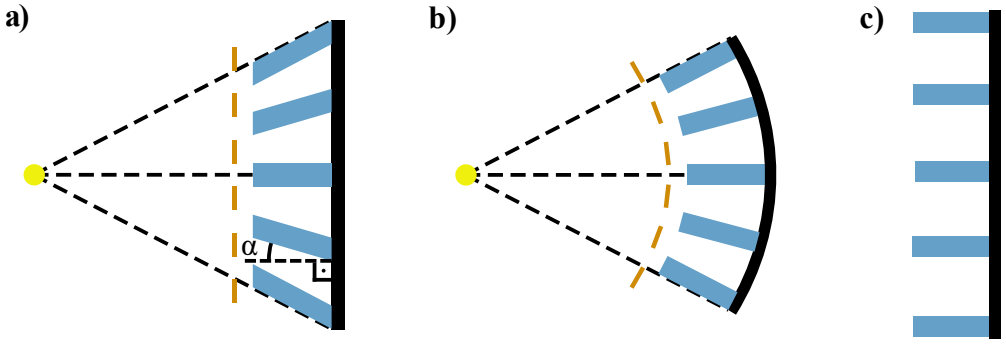

Figure 5.2: Schematic illustrations of the exposure geometry. **a)** In case of unbent mask and substrate, an inclination α of the resulting structures with respect to a line which is perpendicular to the substrate is expected. **b)** For bent mask and substrate the incident radiation impinges on the entire mask perpendicular to its surface. **c)** After the bending is released, the irradiated structures are expected to be perpendicular to the substrate (figure adapted from [Pinzek, 2021a]).

possible with respect to one bending axis. Thus, a structure inclination determined by the cone geometry is expected along the axis around which mask and substrate were not bent.

5.3 Experimental setup

To realize the deep X-ray lithography process with a conventional X-ray tube, an exposure setup was implemented in a compact (1 m wide, 1.6 m long) radiation protection cabin, as shown in Figure 5.3. For the exposure, a sealed fixed-target X-ray tube (MXR-160HP/11, Comet AG, Switzerland) with a tungsten anode is used. The X-ray tube is mounted tilted so that the horizontal central beam has a take-off angle of 24° to the anode to reduce the intensity gradient due to the Heel effect [Pinzek, 2018]. The tube is operated at 40 kV tube voltage and 25 mA anode current with a nominal focal spot size of 1 mm. The exposed substrate is mounted together with the X-ray mask on an object table, which can be moved in 3 dimensions via three motorized linear axes. To reduce the amount of scattered radiation a collimator is placed near the tube window. A second collimator is placed in front of the mask to limit the exposed area as required. Both collimators are adjusted before each exposure to ensure that only the desired area of the substrate is exposed. In case of multiple exposures, where several areas of the same size are exposed on a single substrate, substrate and mask are moved between the individual exposures relatively to the collimators. In addition to these two collimators, a third circular collimator with a fixed diameter of 80 mm is placed at the position of the second collimator to account for the round mask and substrate design. Since conventional X-ray tubes are not designed for continuous operation over many hours and days, flux variations can occur. Therefore, a flux monitor is installed directly below the first collimator, where it measures a small part of the tubes direct beam. This allows to measure flux variations and thereby compare different exposures.

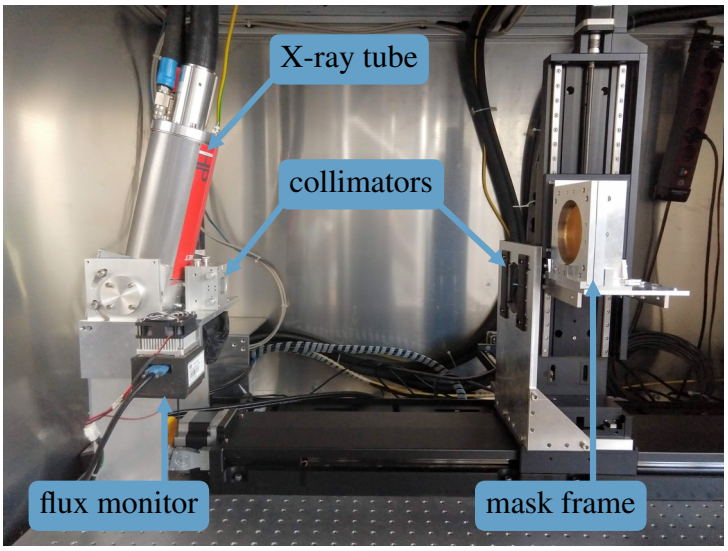

Figure 5.3: Photograph of the lithography setup at a conventional X-ray tube. The entire setup is located in a compact radiation protection cabin (figure adapted from [Pinzek, 2021a]).

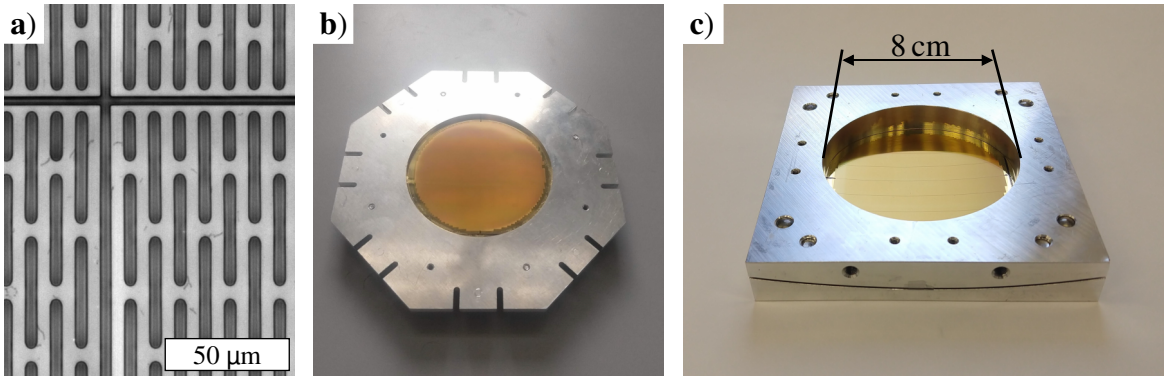

Figure 5.4: **a)** Optical microscope image of the employed X-ray mask. The periodic grating structure with its supporting bridge structures is interrupted every 10 mm in vertical and horizontal direction by an expansion joint. **b)** Photograph of the mask mounted in a flat frame. **c)** Photograph of the same mask mounted in a frame with a bending radius of 30 cm (figure partly adapted from [Pinzek, 2021a]).

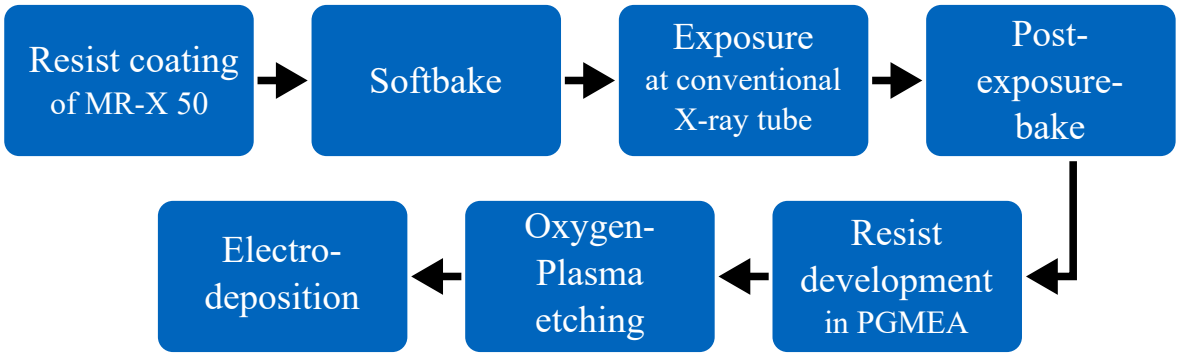

Figure 5.5: The substrate preparation involves resist coating and softbake followed by the X-ray exposure. Afterwards the post-exposure-bake and the chemical development is performed. Optionally, a Oxygen-Plasma etching and gold electrodeposition can be carried out thereafter (figure adapted from [Pinzek, 2021a]).

For all exposures in this thesis, an X-ray mask was used as employed for the standard process at the KARA synchrotron facility. The mask is fabricated on a 550 µm thick polyimide four inch wafer substrate and has a gold absorber height of 40 µm. It consists of an array of 45 µm gold lamellae separated by 5 µm supporting resist bridge structures. The gold lamellae have a periodicity of 10 µm and their duty cycle is 0.53 to 0.54. Furthermore, the mask includes expansion joints with the same width as the gold lamellae in the horizontal and vertical direction spaced at 10 mm intervals, which are required to reduce stress on the resist structures during post-exposure-bake of the grating (see Figure 5.4 **a)**). At the beginning of this thesis, the mask was mounted together with the coated substrate in a flat mask frame on the object table (see Figure 5.4 **b)**). Towards the end of the thesis, this mask frame was replaced by a bending mask frame (30 cm radius), which bends both mask and substrate cylindrically focusing into the source spot of the X-ray tube (see Figure 5.4 **c)**).

5.4 Substrate preparation

For the exposures at the setup as described above, partly, coated substrates were used that were purchased from microworks GmbH (Karlsruhe, Germany). In this case, the substrates were illuminated and sent back for the subsequent process steps. However, the pre-treatment and post-treatment steps are comparable to the procedures illustrated in Figure 5.5 and described in more detail below for substrates that were prepared on site.

5.4.1 Photoresist coating

For substrates prepared on site, four inch graphite wafers were used. The advantages of graphite as a substrate material are discussed in chapter 3.1.1. First, the surface of the

graphite substrate is cleaned under demineralized water and then dried at 200 °C on a hot plate. Afterwards, compressed air is used to remove any remaining dust particles from the surface of the substrate. Subsequently, the substrate is mounted on a vacuum chuck in a spin-coater and then covered with a layer of the photosensitive negative resist MR-X 50 (Microresist Technology, Germany). Due to the high viscosity of the resist, the amount of resist applied varies strongly. To distribute the resist evenly and to achieve a uniform film thickness, the substrate is first rotated for 30 s at 500 revolutions per minute, followed by a 60 s pause. Then the substrate is rotated again at 550 revolutions per minute for 60 s.

5.4.2 Softbake

The spin coating process is immediately followed by a softbake, in which the solvent content of the resist is reduced. For this purpose, the substrate with the resist is placed on a hot plate, which follows a precise temperature profile. First, the substrate is heated to 75 °C over 30 min and this temperature is kept constant for 1 h. Then the temperature is increased to 95 °C over 30 min and is kept constant for 4 h. The temperature is then lowered to ambient temperature over another 4 h. The softbake is carried out in a laminar flowbox to avoid contamination with dust particles, which might lead to defects in the resist layer. After the softbake, the substrate is ready for X-ray exposure.

5.4.3 Exposure

During the exposure step, the substrate together with an X-ray absorbing mask is illuminated with an X-ray beam. The mask used results in only certain areas of the resist being exposed. The exposure process has been continuously improved during the course of this thesis and will be discussed in more detail in the following sections.

5.4.4 Post-exposure-bake

After X-ray exposure, a post-exposure-bake of the substrate is performed for cross-linking the exposed resist molecules. For this purpose, the substrate is heated over 1.5 h to 66 °C on the same hotplate as used for the softbake and held at this temperature for 4 h. The temperature is then reduced linearly to 50 °C over 10 h. After 30 min at this temperature, it is reduced to ambient temperature over 4 h. The temperature ramps are chosen so flat to reduce internal stress in the resist structures.

5.4.5 Chemical development

Directly following the post-exposure-bake, the unexposed and thus non-crosslinked regions of the resist are dissolved in a solvent bath of propylene glycol methyl ether acetate (PGMEA). Therefore, the substrate is placed in the solvent with the resist layer facing downwards and no agitation was applied. The entire development process lasted 4 h, with the PGMEA solvent being replaced after 30 and 90 min. Then, the substrate was dried at 30 °C in a heating chamber.

5.4.6 Plasma etching and electroplating

During this thesis, the processes described in this section were carried out by microworks GmbH (Karlsruhe, Germany).

After the development of the resist, residue can remain at the bottom of the developed structure, which will disturb the electroplating step. To ensure a homogeneous electroplating process the residue are removed by a Oxygen-Plasma treatment in a Reactive-Ion etching machine (Sentech Etchlab 200) for 1 h with a high frequency (HF)-Power of 120 W and 50 sscm at 10 mTorr atmosphere. The HF-Bias voltage is set to −310 V.

The electrodeposition is performed at 55 °C using a sulfite gold plating solution with a gold concentration of 20 gAu/L instead of the often used gold cyanide which is less environment and operator friendly. Using a current density of 0.17 A dm^{-1}, a plating rate of 6 µm h^{-1} can be achieved. Special care is taken to ensure a homogeneous exchange of electrolyte. Agitation with a magnetic stirrer at 100 rotations per minute and a homogeneous distribution of the electric field are applied. Both aspects are important to obtain homogeneous growth rates over the entire area of the grating.

5.5 Determining exposure time

5.5.1 Exposure series

In a first step, the required exposure time was determined. For this purpose, a silicon substrate prepared by microworks GmbH (Karlsruhe, Germany) with a photo resist layer about 170 µm thick was mounted together with the mask in the flat frame shown in Figure 5.4 **b)** and placed at 30 cm distance from the source spot. To test multiple exposure times on a single substrate, the collimators were adjusted to expose only an area of 15 mm × 15 mm at a time. Relative movement of the mask and substrate with respect to the collimators thus allowed 12 test areas to be exposed. During the initial experiment exposure times ranging from 16.8 h

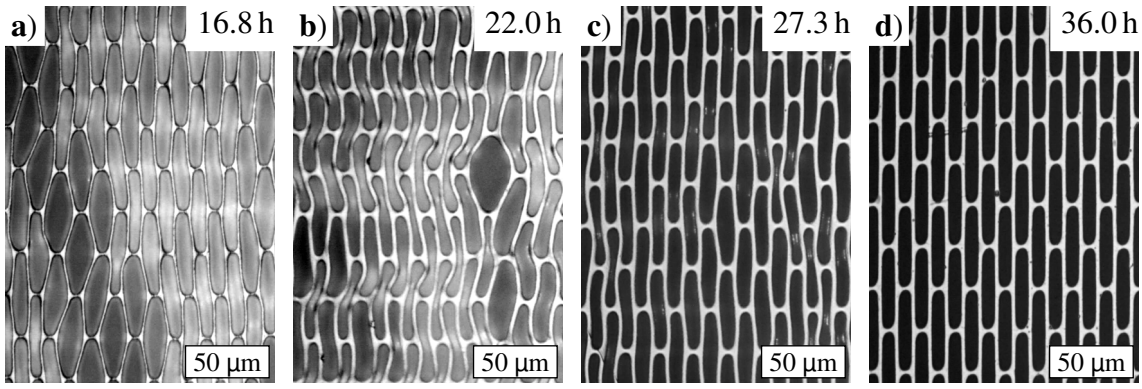

Figure 5.6: Optical microscope images of the developed resist structures for different exposure times.

to 36 h have been applied. Afterwards, post-exposure-bake and chemical development of the exposed substrate were performed by microworks GmbH (Karlsruhe, Germany).

Optical microscope images were taken of each exposed area to characterize the individual areas and thus to evaluate the optimal exposure time. Figure 5.6 shows a selection of images for different exposure times. Microscope images of all 12 exposed areas are given in appendix A. Clear deformations of the resist structure are visible in Figure 5.6 **a) – c)**. Only the 36 h exposed area in Figure 5.6 **d)** reveals parallel grating lines connected by regular bridge structures.

Since the 36 h exposed area was observed to have the best structure, only this area was prepared for electroplating and the remaining areas were covered during the remaining process. An Oxygen-Plasma treatment was first used to remove any resist residues in the structure trenches to enable proper gold deposition. Figure 5.7 **a)** shows a photo of the electroplated area. A bright gold surface is visible at the left edge, as more gold was deposited there during electrodeposition and the resist structures were overplated. Figure 5.7 **b)** shows a optical microscope image of the gold-filled grating structure in the center of the area. It is evident that gold has been deposited in all visible grating trenches and therefore there are no missing gold lamellae.

5.5.2 Characterization of the 36 h exposed grating structure

Since this small grating sample is one of the first gratings exposed with a conventional X-ray tube (and thus with a divergent beam geometry), the inclination of the grating lines is of particular interest. Therefore, an AXT analysis (see section 3.3.3) was performed for the characterization of the grating sample. For this purpose, 300 transmission images were acquired in an angular range of $\pm 15^\circ$ in a phoenix|X-ray v|tome|x (General Electrics) microCT system with a direct tungsten anode tube. The tube was operated at 70 kV tube voltage and

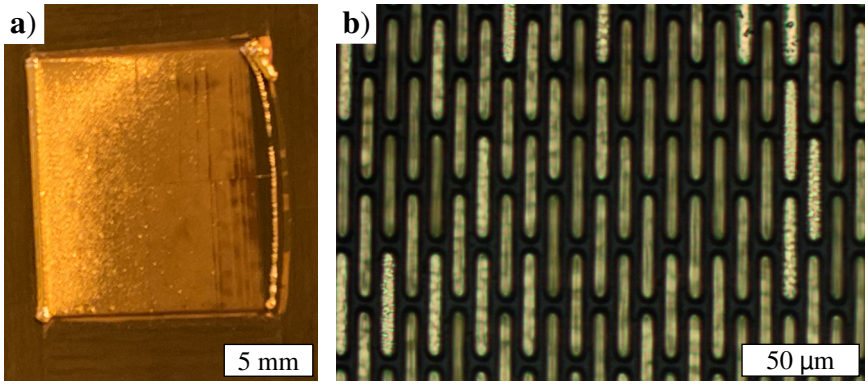

Figure 5.7: **a)** Photograph of the area exposed for 36 h after electroplating. **b)** Optical microscope image of resist structure filled with gold.

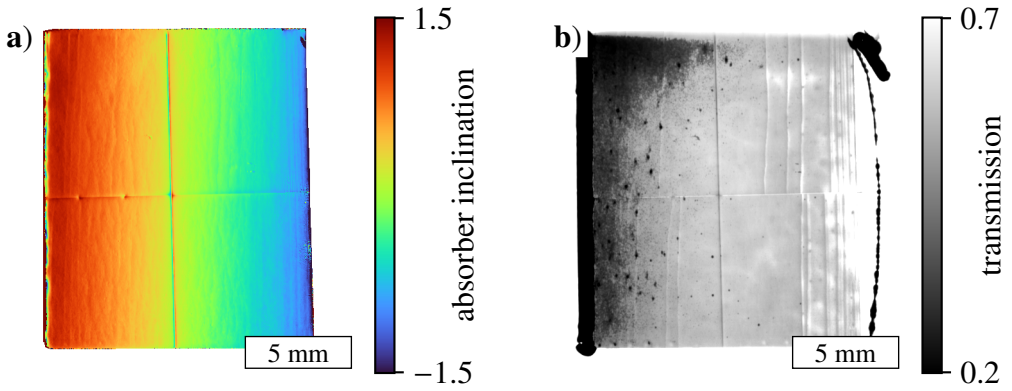

Figure 5.8: **a)** Inclination angle α of the gratings absorption lines and **b)** a inclination corrected transmission image of the small grating area which was exposed for 36 h.

100 µA tube current and the images were acquired with an exposure time of 5 s. The resulting absorber inclination image is given in Figure 5.8 **a)**. An uniform gradient of the absorber inclination is found, which coincides with the cone angle of the exposed area at a distance of 30 cm. In addition, a cross-like structure can be seen extending from the upper to the lower edge as well as from the left to the right edge. This structure is a result of the expansion joints in the mask design shown in Figure 5.4 **a)**. An inclination corrected transmission image is shown in Figure 5.8 **b)**. Here it is clearly visible that the grating absorbs much stronger at the left edge than on the remaining area. This can be explained by the local over plating which was already observed in Figure 5.7 **a)**. Overall, this suggests that during this 36 h exposure sufficient dose for a successful development and subsequent electroplating was deposited in the photo resist. Therefore, this 36 h exposure is used as reference exposure time in the further course of this chapter.

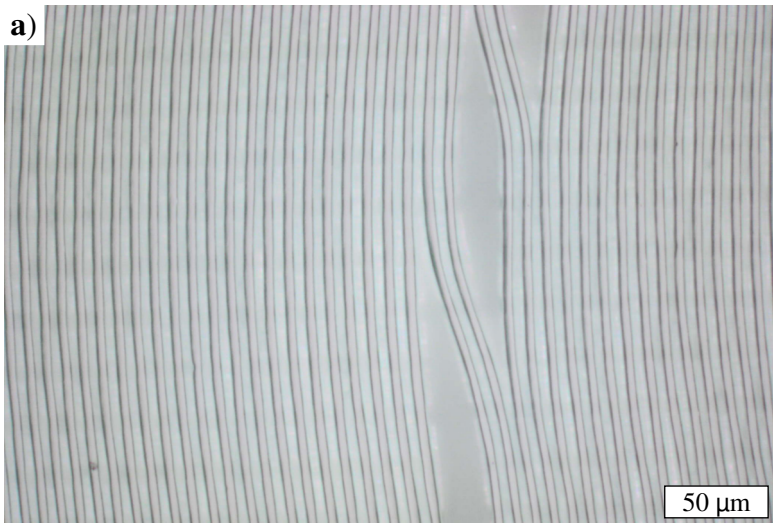

Figure 5.9: Optical microscope image of the developed resist structure after the continues scanning exposure. No bridge structures are present as the deposited dose is smeared out in these regions due to the divergent X-ray beam.

5.6 Increasing exposure area

After the successful exposure of the small grating area described above, the next step is to fabricate larger grating areas. For this purpose, several approaches were pursued, which are described and subsequently analyzed in this section.

5.6.1 Continuous scanning exposure

In a first approach, a continuous scanning was applied. For this purpose, the collimators were adjusted to irradiate a 18 mm × 80 mm-sized horizontal slot in the mask plane. Again, a silicon substrate prepared by microworks GmbH (Karlsruhe, Germany) with a photo resist layer of about 185 µm was mounted together with the mask in the flat frame shown in Figure 5.4 **b)** and placed at 30 cm distance from the source. During the exposure the mask and substrate assembly was moved/scanned vertically through the 18 mm high slot at a speed of 0.5 mm h^{-1}. Consequently, each point of the substrate was exposed for a total of 36 h. Afterwards, post-exposure-bake and chemical development of the exposed substrate were conducted by microworks GmbH (Karlsruhe, Germany).

After development of the substrate, a partial lift-off of the resist structure occurred. An optical microscope image of the developed structure is shown in Figure 5.9. The developed grating lines do not run straight and partly larger gaps between individual lines are torn open. Also, no bridge structures as present in the mask design (see Figure 5.4 **a)**) are observable.

The reason for the absence of bridge structures, although they are present in the mask design,

is the divergence of the applied X-ray radiation. The 18 mm slot height at a distance of 30 cm from the source results in an angle of 3.4° between the upper-most and lower-most ray paths hitting the mask. Considering the thickness of the mask substrate of 550 µm this leads to a shift of the bridge positions projected into the resist by about 33 µm when mask and substrate pass through the slot. Since the bridges of the mask are only 5 µm wide, this results in a strong smearing of the dose in this area. Consequently, no sufficient dose for cross-linking of the resist is applied to imprint the bridges.

Consequently, the continuous scanning approach will not be pursued further in the following sections since it can not transfer the bridges into the resist. This problem could be solved by using a significantly smaller slot width, i.e., much smaller than 18 mm, but can not be fully eliminated. Another important conclusion from this exposure experiment is the observed lift-off and grating line deformation. While the latter can be explained in part by the absence of the bridges and consequently a loss of stability the lift-off is usually an indication for insufficient exposure dose. This is also consistent with the flux monitor measurement, which showed a significant decrease in average tube flux compared to the exposure in section 5.5. Therefore, the exposure time is increased to 50 h for the following exposure.

5.6.2 Step and shoot exposure

The next approach to increase the total exposed area can be described by a step and shoot process. The collimators were adjusted to irradiate a 21 mm × 80 mm-sized horizontal slot in the mask plane. In this way it is possible to expose the entire mask area in four successive exposures (shots), between which the mask and substrate are shifted by one slot height (steps). For this exposure a silicon substrate prepared by microworks GmbH (Karlsruhe, Germany) with a photo resist layer of about 200 µm was mounted together with the mask in the flat frame shown in Figure 5.4 **b)** and placed at 30 cm distance from the source. The exposure time was set to 50 h for each slot to compensate the reduced flux of the X-ray tube, resulting in a total process time of 200 h. Post-exposure-bake and chemical development of the substrate were conducted by microworks GmbH (Karlsruhe, Germany).

In the picture of the developed substrate (see Figure 5.10 **a)**) the four individual exposure slots separated by horizontal lines are visible. Figure 5.10 **b)** and **c)** show microscope images of the developed resits structure in the center of the substrate and near right edge, respectively. In both images bridges are visible and grating structure seems significantly less distorted than in the previous experiment with scanning exposure. However, the duty cycle of the structure in both images differs significantly. The duty cycle in the center of the substrate is close to 0.5, as intended, while it approaches close to 1 near the left and right edges of the exposure slot. Since the structures are overall of good quality, the entire substrate was subsequently plasma etched and electroplated with gold (Figure 5.10 **d)**). After electroplating again the horizontal lines separating the individual exposure slots are visible as areas where no gold has been deposited. In addition, a dark region is visible in the center of the substrate, extending from the top to the bottom edge, where no gold deposition has taken place.

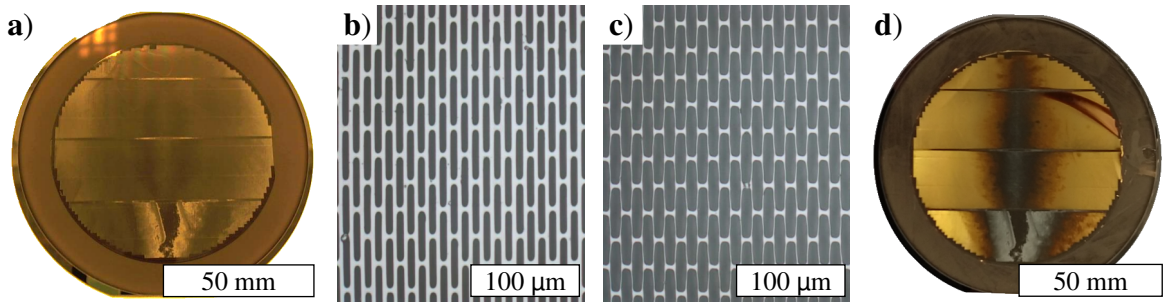

Figure 5.10: **a)** Photograph of the developed substrate exposed by the step and shoot process. Optical microscope images of the resist structure in the center and near the right edge of the wafer are shown in **b)** and **c)**, respectively. **d)** shows a photograph of the same wafer after electroplating.

The visible separation of the individual exposure slots (Figure 5.10 **a)** and **d)**) is caused by a slightly larger exposure slot compared to the shift of mask and substrate between the individual exposures. As a result, in an area of about 1 mm height, a double exposure occurred and thus twice the dose was deposited, which leads to a local overexposure. Due to this overexposure no electroplating could start in this regions.

Both optical microscope images of the grating structure (Figure 5.10 **b)** and **c)**) reveal parallel grating lines connected by regular bridge structures, indicating that the exposure time of 50 h was in the correct time range. However, the dark region in the center of the electroplated substrate indicates, that the deposited dose was too high in the central region. Due to the inverse-square law, the deposited dose decreases towards the edges of the substrate, which prevents overexposure there and allows for successful electroplating. The change of the duty cycle depending on the position is caused by shadowing effects in the mask during exposure. In the center of the mask, the X-rays impinge perpendicular to the mask lamellae, whereas the radiation impinges in an inclined way onto the mask at the edges. Thus, at the edges the radiation sees an effectively smaller mask opening, leading also to thinner resist structures. To compensate this duty cycle variation but also the dose gradient from the center to the edges a bending frame for mask and substrate with an bending radius equal to the exposure distance is used for the next exposures.

Furthermore, it has been observed in previous sections that the flux variations of the X-ray tube cause problems in the deposition of the optimal resist dose. Until now, exposure times are referred to as the absolute times required for a successful exposure. However, in the course of several exposures it is found that the flux of the X-ray tube varies by several percent within an exposure and tends to decrease with the overall operating time of the X-ray tube. Figure 5.11 shows the measured flux of the X-ray tube for four consecutive exposure series. Each exposure begins with a warm-up procedure in which the tube current is increased stepwise. Immediately afterwards, the maximum flux is measured for each exposure. Over a period of about 5 h, the flux initially decreases by 1-1.5% as the tube and its components reach thermal equilibrium during this period. Thereafter, the flux continues to drop, but at a much slower rate. It is noticeable that the flux reached after the first steep flux drop is

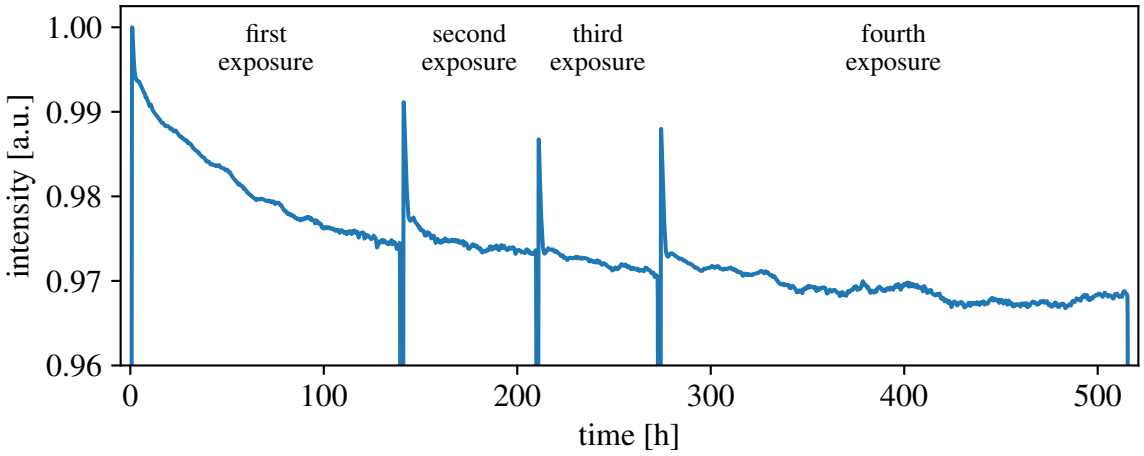

Figure 5.11: Measured flux of the X-ray tube over four consecutive exposures. Each exposure starts with a short warming up procedure followed by the actual exposure. A permanent and non-reversible decrease of the flux of approximately 3% is apparent.

approximately the same as the flux reached at the end of the previous exposure. This causes the overall flux to decrease permanently from exposure to exposure. Therefore, instead of using a fixed exposure time for the following exposures, a duration adjusted to the flux was used. For this purpose, the flux is integrated during the exposure. The exposure is then continued until the value for the integrated flux of the 36 h reference exposure is reached.

5.6.3 Full-field exposure

The final approach to achieve increased grating area is a single full-field exposure of the entire mask and substrate. The collimators were adjusted to irradiate a 66 mm × 66 mm-sized area in the mask plane. Thus, it is possible to cover almost the entire mask area in a single exposure. For this exposure a graphite substrate was coated with a photo resist layer of about 110 µm. To prevent variations in duty cycle and the deposited dose as seen before, mask and substrate were mounted in a frame with a bending radius of 30 cm (see Figure 5.4 **c)**) and were positioned with the source in it's center. The actual exposure was performed until the integrated flux of the beam monitor reached the reference value of the 36 h exposure in section 5.5. This lead to a total exposure time of 55.2 h. Subsequently a post-exposure-bake and chemical development of the substrate were conducted. Plasma etching and electroplating the developed substrate was performed by microworks GmbH (Karlsruhe, Germany) achieving a gold height of about 80 µm. Photographs of the grating after the chemical development and after the electroplating are shown in Figure 5.12 **a)** and **d)**.

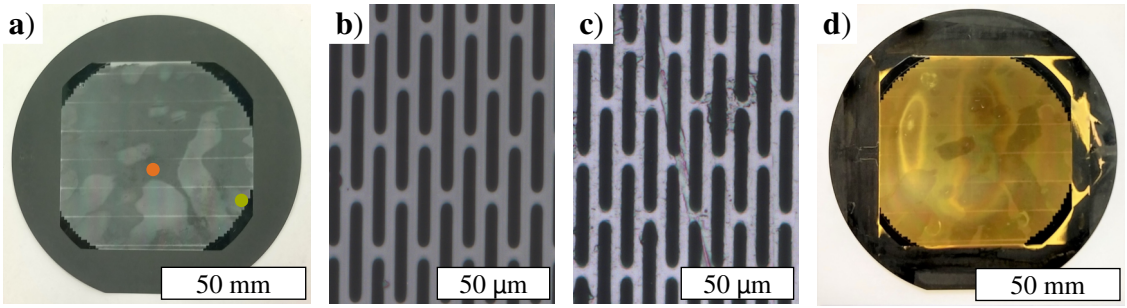

Figure 5.12: **a)** Photograph of the developed resist structure on a four inch graphite wafer which was exposed to X-ray radiation in a single full-field exposure. **b)** & **c)** Optical microscope images with 200x magnification of the grating structure before electroplating marked by the orange (**b)**) and green (**c)**) dots in **a)**. **d)** Photograph of the fabricated grating after electroplating (figure partly adapted from [Pinzek, 2021a]).

Characterization methods

Representative images of the developed grating structure before electroplating were acquired with an optical microscope (Axiskop 2 MAT mot, ZEISS), to examine the structure quality. Figure 5.12 **b)** and **c)** show microscope images of the resist structure in the center of the wafer and near its lateral edge. In addition, from these images, the duty cycle of the grating was determined in regions without support structures (bridges).

A high-resolution X-ray transmission radiograph of a representative region in the center of the grating was acquired with a microCT system (Xradia 500 Versa, ZEISS) with an effective pixel-size of 0.619 µm. The tube voltage and current were set to 60 kV and 16.7 µA respectively and the exposure time was 180 s. For comparison, a radiograph of a classical direct deep X-ray LIGA grating with the same period was acquired using the same measurement parameters. This grating was fabricated by the direct deep X-ray LIGA-process at a synchrotron source on a 530 µm thick silicon substrate and has a gold height of 145 µm. For both gratings transmission images which are normalized to their maximum value are shown in Figure 5.13 **a)** and **b)**. For better comparison, corresponding line profiles in a region of interest in which no bridges are present between the grating lines are plotted in Figure 5.13 **c)**. To increase statistics data of 15 pixel-rows is averaged.

As the exposure at a conventional X-ray tube is performed with a divergent beam geometry, the inclination of the absorber lines and bridge structures is of particular interest. Therefore, the angular X-ray transmission of the grating was evaluated in a phoenix|X-ray v|tome|x (General Electrics) microCT system with a direct tungsten anode tube. The tube was operated at 70 kV tube voltage and 120 µA tube current. Between $\pm 30^\circ$ rotation of the grating, images were taken in 0.2° steps with an exposure time of 5 s. Two sets of images were taken, one with the rotation axis along and one with the rotation axis perpendicular to the grating lines. Afterwards, both measurements were processed to obtain a spatial map of the structure inclination (see Figure 5.14 **a)** and **b)**). Additionally, an inclination corrected

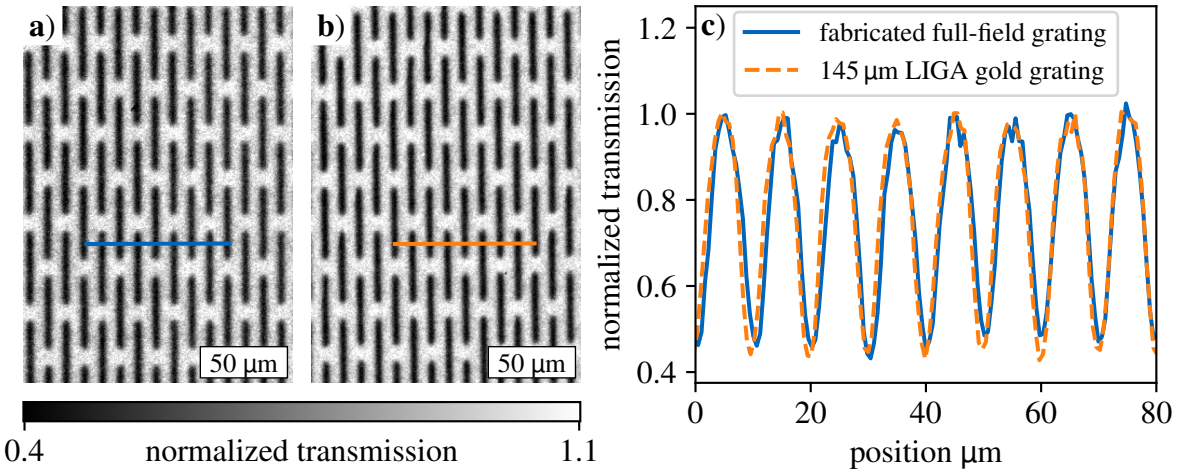

Figure 5.13: Representative transmission images at 60 kV tube voltage for **a)** the fabricated full-field grating and **b)** a classical direct deep X-ray LIGA grating with 145 µm gold height fabricated at a synchrotron source. c) Corresponding line profiles along the blue and orange lines in **a)** and **b** (figure partly adapted from [Pinzek, 2021a]).

transmission image of the grating was determined (see Figure 5.14 **c)**).

To analyze the performance of the grating, it was tested in a preclinical Talbot–Lau interferometer designed for medical thorax imaging. It was used as analyzer grating and was arranged together with a source grating fabricated by LIGA (200 µm gold height) and a silicon π-phase shifting grating (60 µm silicon height). All gratings have a period of 10 µm and the source grating was bent with the source spot in its center to reduce shadowing effects. The gratings were configured in a symmetric geometry with an inter-grating distance of 92 cm operated in the first fractional Talbot distance. The distance between analyzer grating and the X-ray tube (MRC 200 0310 ROT-GS1004, Philips Medical Systems, Hamburg, Germany) was 196 cm. The tube was operated at 60 kV tube voltage and 250 mA tube current. Seven images with 500 ms exposure time were acquired using a flat-panel detector (Pixium RF 4343, Trixell, Moirans, France) while the source grating was stepped over one grating period. Images with and without samples were processed as described in section 2.4.5 to obtain transmission, dark-field, and differential phase images (Figure 5.15). As samples, a 1 cm neoprene cube and three Eppendorf tubes filled with water, cotton wool, and air, respectively were used. The flat-field visibility of the interferometer, which is a crucial parameter for image quality, was determined from the images without samples.

Characterization results and discussion

Results from optical evaluation

As the photograph of the substrate after the chemical development in Figure 5.12 **a)** shows, no lift-off of the resist structure took place during development. Further the photograph after

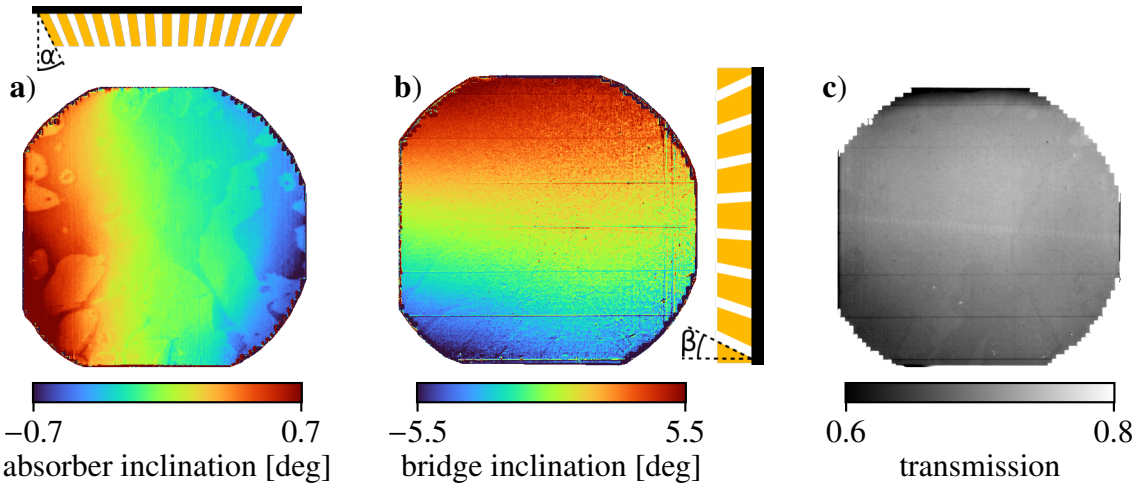

Figure 5.14: **a)** Inclination angle α of the gratings absorption lines with a sketch of their orientation. **b)** Inclination angle β of the gratings resist support bridges with a sketch of their orientation. **c)** Inclination corrected transmission of the grating. All three images are a result of an AXT analysis (figure adapted from [Pinzek, 2021a]).

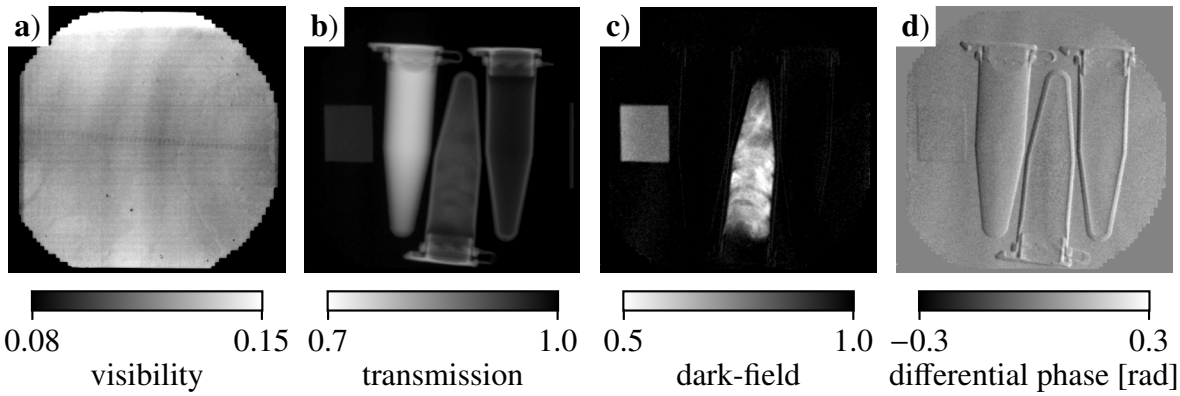

Figure 5.15: **a)** Visibility in a preclinical X-ray dark-field interferometer designed for medical thorax imaging at 60 kV tube voltage. **b)** Transmission image, **c)** dark-field image, and **d)** differential phase image of a neoprene cube and three Eppendorf tubes filled with water, cotton wool, and air (figure adapted from [Pinzek, 2021a]).

electroplating (Figure 5.12 **d)**) reveals that gold was deposited in the grating structures over the entire exposed area. There are some patches and 7 horizontal lines with 1 cm distance between each other visible in both pictures. These patches are located at the positions where air was present between the substrate and the protective polyimide foil after exposure. The horizontal lines correspond to the expansion joints in the mask design.

A qualitative inspection of the grating surface was performed at several locations by optical light microscopy showing a good structural uniformity (Figure 5.12 **b)** and **c)**). This shows that the chosen exposure time of 55.2 h was sufficient to deposit enough dose for successful cross-linking of the resist. The duty cycle of the grating is 0.55 measured from microscope images, which is close to the masks duty cycle of 0.53 to 0.54. Such small duty cycle variations can be attributed to minor over or underexposure of the resist.

Results from X-ray transmission analysis
So far, only the surface of the grating has been inspected. The normalized transmission images of the grating fabricated with the full-field exposure and of the classical direct deep X-ray LIGA grating (Figure 5.13 **a)** and **b)**) reveal comparable structure quality. The transmission profiles of both gratings emphasize this finding further (Figure 5.13 **c)**). For both gratings, the minimum normalized transmission is around the value 45%. The classical direct deep X-ray LIGA grating absorbs slightly more.

The evaluation using X-ray transmission imaging demonstrates that X-ray tube exposed gratings can reach comparable attenuation profiles as gratings exposed at a synchrotron. However, due to lack of comparable substrates and absorber heights a direct comparison is not possible.

Evaluation results for structure inclination
The inclination of the gratings absorber lines has a gradient perpendicular to their orientation in the range of $\pm 0.7^\circ$, as it can be seen in Figure 5.14 **a)**. This gradient is overlaid with the patch pattern, which was already visible in Figure 5.12 **a)** and **d)**. The inclination of the supporting bridge structures is shown in Figure 5.14 **b)**. It reveals a gradient in the range from $\pm 5.1^\circ$ along the orientation of the grating absorber lines. The gradient is overlaid by the seven horizontal lines which are also visible in Figure 5.12 **a)** and **d)**. These are the places where no grating structure is present due to mask design. Consequently, no valid inclination information can be determined at these places.

Figure 5.14 **c)** displays the inclination corrected transmission of the grating. The transmission values at the upper and lower edges are slightly reduced compared to the center of the grating, while no gradient from the left to the right edge of the grating is visible. Since mask and substrate were bent with their distance to the source as radius, no gradient should be visible in the inclination image for the absorber lines. The bridge inclination also deviates from the theoretically expected range of $\pm 6.3^\circ$ determined by the cone geometry of the X-ray beam (resulting from 66 mm grating width and 30 cm exposure distance). As the resist shrinks during the post-exposure-bake process, stress is induced between the substrate and the resist layer. This stress causes a bending of the substrate and thus of the entire grating. This also occurs for gratings exposed at synchrotron sources, and results there as well in ab-

sorber inclinations in the same order of magnitude for comparable gratings (i.e. similar area and substrate). Another possible reason is a deviation from the cylindrical bending during exposure. However, this would result in a change of duty cycle at the edges of the grating as well, which would be visible in the inclination corrected transmission by reduced values at the left and right edges. Since this is not visible, it can be assumed that no major deviations from the cylindrical bending has occurred during exposure. The reason for the slightly reduced transmission values at the upper and lower edges is that the measurement only corrects for the absorber inclination and not for the influence of the bridge inclination.

Results from an interferometric measurement
The flat-field visibility of the interferometer is shown in Figure 5.15 **a)**. The mean visibility obtained is 12.5 %, with increasing visibility towards the upper and lower edges and reaching a maximum value of 19.0 %. The processed transmission, dark-field, and differential phase images of the four samples are shown in Figure 5.15 **b) – d)**.

This comparably low visibility is expected, as the gold height is significantly lower than for state-of-the-art direct deep X-ray LIGA gratings, and at the same time a relatively hard X-ray spectrum at 60 kV tube voltage was used. The visibility gradient is a consequence of the transparent bridges which can be seen with classical direct deep X-ray LIGA gratings as well. In the center of the grating, the X-ray radiation impinges parallel to the transparent bridges. Therefore, the radiation is not absorbed in these areas and the visibility is reduced. However, at the edges of the grating, the bridges are no longer parallel to the radiation due to the bridge inclination and the cone geometry of the imaging setup. This implies shadowing of the bridges leading to increased absorption of the radiation, and therefore increased visibility. The processed transmission, dark-field, and differential phase images of the four samples demonstrate the complementarity of the three modalities. The water-filled Eppendorf tube mainly absorbs the X-rays and is thus clearly visible in the transmission image. The neoprene cube and the Eppendorf tube filled with cotton wool cause small-angle scattering of the radiation due to the many air-material interfaces and are thus particularly visible in the dark-field image. Although the Eppendorf tubes themself lead to weak absorption of the radiation, they are especially well visible in the differential phase image.

5.7 Summary

In this chapter deep X-ray lithography based on a conventional X-ray tube is introduced. Different requirements for such a setup were discussed and implementations and experimental results have been demonstrated. After a short description of the individual steps of the LIGA process, the remaining chapter focuses on the X-ray exposure. First, the exposure time required for successful development of the photosensitive resist was determined with a series of exposures to 36 h. In later exposures significant X-ray flux variations have been identified which lead to under exposure of the resist. As a consequence, instead of configuring a fixed exposure time the time was adjusted in real time using a flux monitor to reach a specific X-ray dose. In the further course, different approaches were employed to

increase the grating area. When scanning the mask and substrate continuously through a slit aperture, an unwanted smearing of the dose occurs in the area of the supporting bridge structures. As a result, no bridge structures were present after chemical development and the grating lines were strongly deformed. In another approach, mask and substrate were moved stepwise past an slit aperture in between individual exposures (step-and-shoot). Solid resist structures were successfully exposed, developed and subsequently electroplated. However, a strongly varying duty-cycle of the structures from the center to the lateral edge was observed which is cause be shadowing of the flat mask. Further a dose variation due to the inverse-square law was observed. During a 66 mm × 66 mm full-field exposure these both issues were addressed by bending mask and substrate with the source spot of the X-ray tube in its center. This led to a uniform grating structure comparable to results obtained from LIGA at a synchrotron source. Finally, this grating was characterized using optical microscopy, X-ray Transmission AXT, and angular X-ray transmission analysis and was successfully tested as analyzer grating in a preclinical Talbot–Lau imaging system designed for medical thorax imaging.

6 Non-Sinusoidal Intensity Modulations

As described in chapter 2.4, grating-based imaging extracts attenuation, dark field and differential phase signals from intensity modulations induced by gratings. Its shape is influenced by the spatial and spectral properties of the used radiation source, the gratings in the beam, the sample, and the used detecting system. The measured intensity modulation can be modeled by the convolution of the individual system components, i.e. source/source grating, reference grating, analyzer grating and detector. In most cases a sinusoidal intensity modulation can be assumed for the data processing [Chabior, 2012]. This chapter addresses cases where the intensity modulation deviates considerably from a sinusoidal shape. Therefore, a new processing method based on a piecewise-defined function composed of zero to second order polynomials is introduced. This function resembles the actual physical image formation process and is developed to model rectangular, trapezoidal, triangular, and sinusoidal intensity modulations.

The findings in this chapter were published in *Signal Retrieval from Non-Sinusoidal Intensity Modulations in X-ray and Neutron Interferometry Using Piecewise-Defined Polynomial Function* [Pinzek, 2021b]. Figures and text passages in this chapter may appear identical to the publication. My contribution to this study was the development of the polynomial-based processing, and its implementation, as well as the evaluation of the results.

6.1 Origin of non-sinusoidal intensity modulations

Following the structure of a grating interferometer as described in chapter 2.4, multiple intensity modulation shapes are possible. In case of using a single phase or absorption grating that creates a binary modulation in combination with a high coherence radiation source (e.g., highly coherent, monochromatic synchrotron radiation), a binary modulation is induced in the fractional Talbot distances. According to equation (2.34), the intensity modulation recorded by a high-resolution detector is given by a convolution of the modulation with the detector PSF. This can result in a rather trapezoidal intensity modulation as illustrated in Figure 6.1 **a)**. Due to a different DC, which deviates from 0.5, asymmetric modulations may also arise as shown in Figure 6.1 **b)**. For example, this is the case when using apertures with narrow openings [Munro, 2012] or phase gratings with non-binary profiles [Yaroshenko, 2014], which can lead to enhanced focusing. But also binary phase gratings with a DC

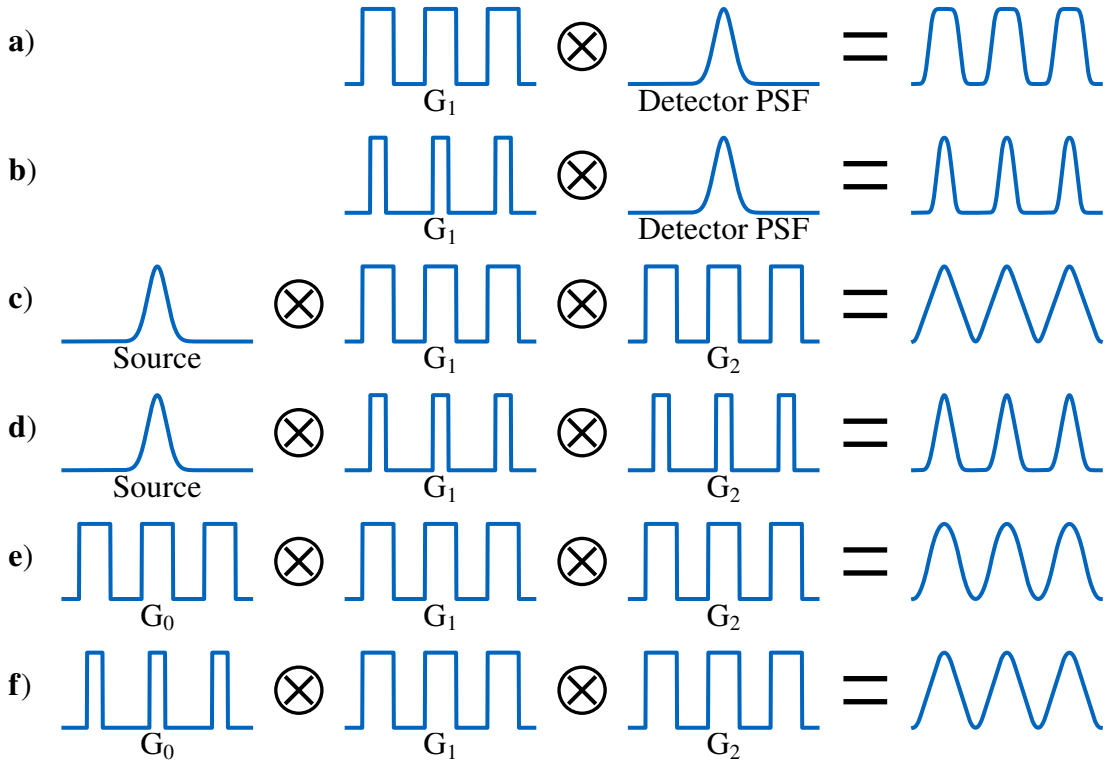

Figure 6.1: Origin of the resulting intensity modulation for different phase-sensitive imaging systems with periodic phase modulators. **a)** Single grating system with a direct resolution of the intensity pattern can result in a trapezoidal modulation. **b)** Single grating system with a larger duty cycle (DC, thus a larger absorbing fraction) resulting in an asymmetric modulation. **c)** Two grating Talbot-interferometer operated with sufficiently coherent source resulting in a triangular modulation. **d)** Two gratings with large DCs resulting in an asymmetric triangular modulation. **e)** Three grating Talbot-Lau interferometer producing a quasi-sinusoidal modulation. **f)** Talbot-Lau system with one grating having a large DC, resulting in deviations from sinusoidal modulations. (figure adapted from [Pinzek, 2021b]).

different from 0.5 can create asymmetric high-contrast modulations [Suleski, 1997].

To relax the requirements on the detector resolution, a analyzer grating can be used. According to equation (2.35), in this case the recorded intensity modulation is given by the convolution of the two grating profiles. Since for setups with analyzer grating, the detector usually records a low-frequency Moiré fringe pattern generated by both gratings, the influence of the PSF on the intensity modulation is negligible. Assuming that both the modulation induced by the G_1 and the transmission profile of the G_2 are binary, a triangular intensity modulation is obtained. According to equation (2.37), once the source used can not be assumed as a point source (e.g. because a microfocus tube with finite source size is used), the source must also be taken into account. This leads to a smoothed intensity modulation (see Figure 6.1 **c**)), which can still deviate quite strongly from a sinusoidal shape. If the DCs of both gratings deviate remarkably from 0.5, the modulation becomes asymmetric (see Figure 6.1 **d**)). This happens, for instance, with the so-called edge-illumination setups, which use apertures with relatively small openings in the range of $4/5$ of the period [Munro, 2012]. Due to Gaussian-shaped sources, for these setups the final intensity modulation can be well described with a Gaussian. However, assuming a point-like source, the intensity modulation would become triangular.

For large source sizes a G_0 can be used to achieve the required beam coherence. Here, the apertures of the grating act as new sources whose intensity profile can be assumed to be binary. Consequently, the intensity modulation in Figure 6.1 **e)** results from the convolution of the binary grating profiles using equation (2.37). Usually these systems are operated with polychromatic spectra and consist of three optics, so the resulting intensity modulation can be approximated well by a sinusoidal function. In cases where the DC of one or more grating deviates significantly from 0.5, the intensity modulation may also become non-sinusoidal, as shown in Figure 6.1 **f)**. Chabior et al. [Chabior, 2012] demonstrated analytically that increasing the DC of e.g. the source grating increases the visibility at the cost of reduced flux. Therefore, under simplified assumptions (e.g., perfectly absorbing gratings), the ideal DC of the source grating to reach the best signal-to-noise ratio in the phase image at a given flux is $2/3$. For systems, where the limiting factor is the absorbed dose (e.g. in medical applications) instead of the the source flux, it might be even more beneficial to increase the DC of the source grating even further.

Further, the intensity focusing properties of the G_1 can be improved by applying phase gratings with adapted DC and phase shift. Suleski [Suleski, 1997] reported intensity focusing ratios of 1:3 that can be reached with several binary phase grating configurations with DCs of 1/3 and 2/3. Systems employing such a G_1 benefit from increased visibility and improved performance with polychromatic spectra [Chabior, 2011]. Similar intensity focusing effects can be obtained by symmetric phase gratings with non-binary profiles, such as triangular, trapezoidal, and parabolic gratings. Using one or several of these setup modifications, the intensity modulation can become non-sinusoidal and asymmetric with three-grating interferometers as well.

6.2 methods

6.2.1 Periodic Polynomial (PP) Intensity Modulation Function

Since the intensity/transmission profiles of the grating used can be taken as binary, the intensity modulation for a Talbot-Lau interferometer results from the convolution of three rectangular functions. The function resulting from this convolution can be described section-wise with polynomials up to the second order. Therefore, to consider all possible shapes of the intensity modulation, a periodic polynomial (PP) function I^{PP} with a period of 2π is introduced in the following, which is piecewise-defined of constant, linear, and 2nd order polynomials:

$$I^{PP}(\phi) = \begin{cases} I_{min}, & 0 < |\phi - \varphi| \leqslant \delta_0 \\ b_1 \cdot (\phi - \varphi - \delta_0)^2 + I_{min}, & \delta_0 < |\phi - \varphi| \leqslant \delta_1 \\ m \cdot (\phi - \varphi) + t, & \delta_1 < |\phi - \varphi| \leqslant \delta_2 \\ -b_3 \cdot (\phi - \varphi - \delta_3)^2 + I_{max}, & \delta_2 < |\phi - \varphi| \leqslant \delta_3 \\ I_{max}, & \delta_3 < |\phi - \varphi| \leqslant \pi \end{cases} . \tag{6.1}$$

Additionally, $\phi = 2\pi x_r/p$ applies, where x_r is the relative displacement of the stepped grating and ϕ is the corresponding phase as labeled on the horizontal axis in Figure 6.2. The minimal and maximal intensity is given by I_{min} and I_{max}, respectively, the phase position by φ, and δ_0 to δ_3 indicate the transition points of the individual sections. Further, from the boundary conditions that $I^{PP}(\phi)$ and $\frac{dI^{PP}(\phi)}{d\phi}$ are continuous functions,

$$m = 2b_1(\delta_1 - \delta_0), \tag{6.2}$$

$$t = I_{min} - b_1(\delta_1^2 - \delta_0^2), \tag{6.3}$$

$$b_3 = b_1 \frac{\delta_1 - \delta_0}{\delta_3 - \delta_2}, \text{ and} \tag{6.4}$$

$$A = I_{max} - I_{min} = b_1(\delta_1 - \delta_0)(\delta_2 + \delta_3 - \delta_0 - \delta_1) \tag{6.5}$$

are derived, where A is the amplitude of I^{PP}. It can be rewritten as a function depending on the seven free parameters φ, I_{min}, A, δ_0, δ_1, δ_2, δ_3 by combining equations (6.1) to (6.5). Figure 6.2 **a)** illustrates I^{PP} exemplary. Figure 6.2 **b) – e)** show different shapes that I^{PP} can adopt by varying the transition points δ_0 to δ_3.

The transition points δ_0 to δ_3 can be determined once in advance based on a reference acquisition. Since the same setup geometry is used for the subsequent object measurement, the previously determined transitions points can be reused, reducing the number of parameters to be determined. This is possible as the shape of the intensity modulation depends on the convolution of the individual gratings and does not change between reference and object acquisition. Therefore, a least-square (LS) optimization can be used to fit $I^{PP}_{\varphi,I_{min},A,\delta_0,\delta_1,\delta_2,\delta_3}(\phi)$

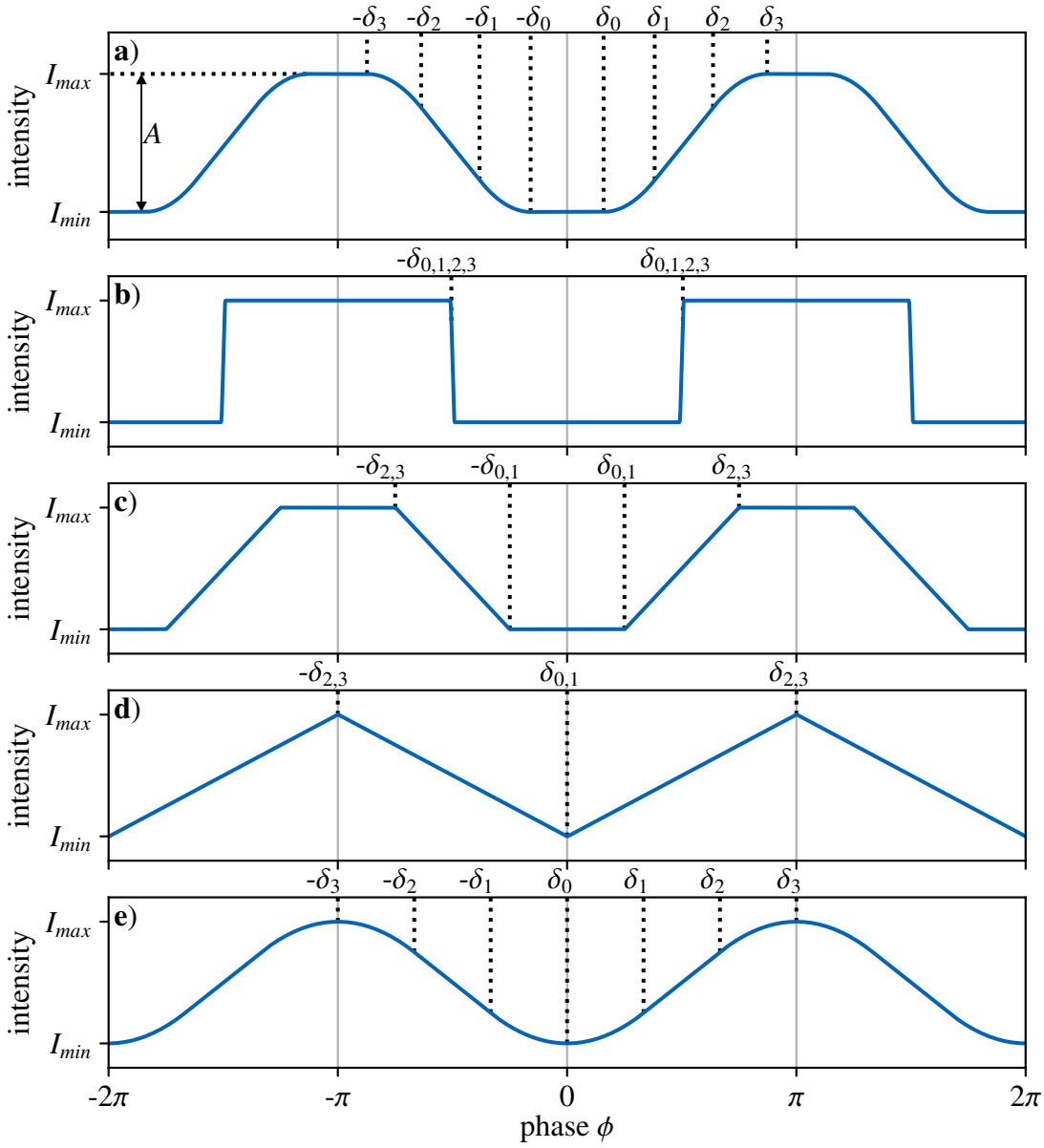

Figure 6.2: Examples of the piecewise-defined periodic polynomial (PP) function I^{PP} for $\varphi = 0$. **a)** Between 0 and δ_0, respectively, δ_3 and π I^{PP} has a constant value of I_{min} and I_{max}, respectively. For phase values between δ_0 and δ_1, respectively, δ_2 and δ_3 I^{PP} is parabolic while it is linear between δ_1 and δ_2. By selecting the four δ-values accordingly I^{PP} can approach different shapes: **b)** rectangular function for $\delta_0 = \delta_1 = \delta_2 = \delta_3$, **c)** trapezoidal function for $\delta_0 = \delta_1 > 0$ and $\delta_2 = \delta_3 < \pi$, **d)** triangular function for $\delta_0 = \delta_1 = 0$ and $\delta_2 = \delta_3 = \pi$, and **e)** sinusoidal function for $\delta_0 = 0$, and $\delta_1 = \pi/3$, $\delta_2 = 2\pi/3$, and $\delta_3 = \pi$ (subfigure **a)** adapted from [Pinzek, 2021b]).

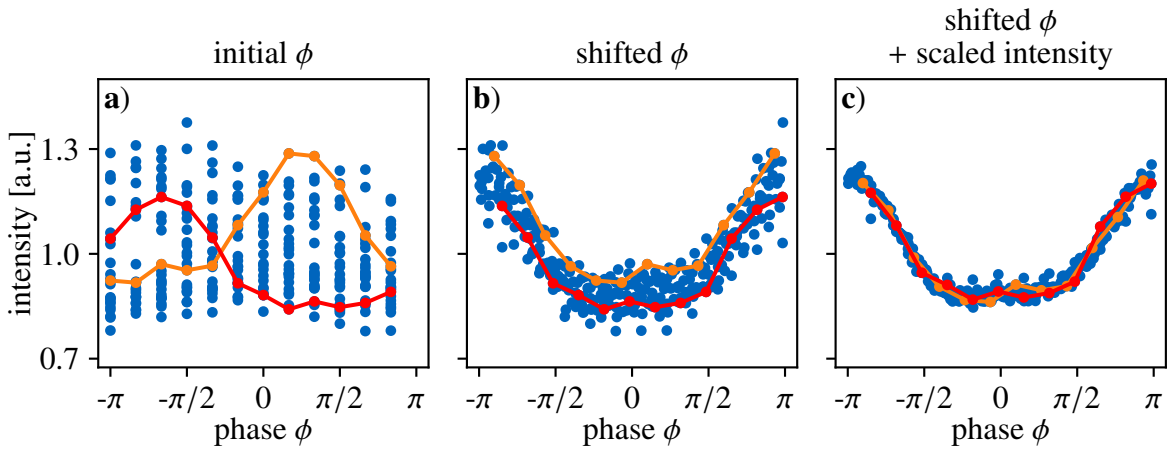

Figure 6.3: Illustration how data from different pixels can be compared to determine the intensity modulation shape. For better a visualization data of only 25 pixels is shown and the data of two different pixels is highlighted in orange and red. **a)** The initial phase ϕ for each pixel is given by the relative grating displacement during the stepping process. Therefore discrete columns with data points are visible. However, due to Moiré fringes the phase position φ of each pixel differs. **b)** By shifting the data points of each pixel by φ determined from a sinusoidal processing results in in-phase sorting. Since also the mean intensity differs from pixel to pixel due to intensity gradients, a large spreading in the intensity can be observed. **c)** Scaling each data point by the mean intensity of its pixel reduces this intensity spread significantly. The resulting data set can be fitted with a least-square optimization of I^{PP} to determine the shape of the intensity modulation.

(here the index denotes the parameters which have to be determined) to a dataset consisting of several pixels' intensity modulations from the detector's entire field of view. To determine the intensity modulation shape for the simulated or measured datasets, in the following sections 2500 pixels were used, which are randomly distributed over the detector's field of view. The number of 2500 pixels was chosen to consider stepping data in all phase positions and to avoid over-fitting of the data. Figure 6.3 shows how the data points of the individual pixels can be compared. First, the stepping positions ϕ are shifted by the first-order phase position φ, which is determined by sinusoidal processing. Afterwards, to compensate for intensity gradients across the detector, the intensities are scaled by the mean intensity of the respective pixel. The values determined for δ_0 to δ_3 represent the shape of the reference intensity modulation and can be reused to process the data of an object acquisition. Therefore, only three parameters (φ, I_{min}, and A) have to be determined by fitting $I^{PP}_{\varphi,\, I_{min},\, A}(\phi)$. However, this is only valid in cases where the object only absorbs or induces phase shifts. Once the object induces small-angle scattering, not only the amplitude but also the shape of the intensity modulation is changed. Thus, the shape of the intensity modulation is no longer adequately described by the previously determined values for δ_0 to δ_3. To address this effect, the influence of varying degrees of scattering can be taken into account in advance. For this purpose, the reference shape of the intensity modulation is convolved with different Gaussian kernels

with index i and the corresponding standard deviation σ_i. The resulting intensity modulations are again fitted with $I^{PP}_{\varphi,I_{min},A,\delta_0,\delta_1,\delta_2,\delta_3}(\phi)$ to determine the associated transition points $\delta_{0,i}$ to $\delta_{3,i}$. A scatter function SF can be created by linear interpolation of these values, which links each scattering strength σ with a corresponding set of transition points δ_0 to δ_3 and thus to a corresponding intensity modulation shape:

$$SF(\sigma) = (\delta_0, \delta_1, \delta_2, \delta_3). \tag{6.6}$$

Therefore, the dependencies in I^{PP} can be reduced by substituting δ_0 to δ_3 with the scatter parameter σ resulting in:

$$I^{PP}_{\varphi,I_{min},A,\sigma}(\phi). \tag{6.7}$$

Here, only four parameters (φ, I_{min}, A, and σ) remain to be determined by PP LS fitting. Comparable to the sinusoidal approach, φ directly holds the information about the phase signal and the differential phase $\Delta\varphi$ is calculated as in equation (2.49). In contrast to the sinusoidal approach, the mean intensity $\bar{I}$ over one period in the PP approach has to be determined from the fitted parameters:

$$\bar{I} = \frac{1}{2\pi} \int_{-\pi}^{\pi} I^{PP}_{\varphi,I_{min},A,\sigma}(\phi)\, d\phi \tag{6.8}$$

The transmission T is then determined comparable to equation (2.46) by the ratio of the mean intensity with an object $\bar{I}^{\text{obj}}$ and without an object $\bar{I}^{\text{ref}}$. Following the definition of the visibility in equation (2.47), one obtains for the visibility according to the PP approach:

$$V = \frac{I_{max} - I_{min}}{I_{max} + I_{min}} = \frac{A}{2I_{min} + A}. \tag{6.9}$$

The dark field signal is then calculated as for the sinusoidal approach according to equation (2.48).

6.2.2 Processing

Four different processing algorithms are applied to simulated and measured datasets and compared in the following sections: two conventional sinusoidal ones and two PP-based ones. The first PP processing algorithm is the periodic polynomial least square (PPLS) fitting. Initially, the intensity modulation shape and the scatter function $SF(\sigma)$ are determined using 2500 randomly selected pixels of the reference dataset as described above. Afterwards, the stepping data of each pixel is fitted with $I^{PP}_{\varphi,I_{min},A,\sigma}(\phi)$. As a comparison, for the PPLS mainly conventional sinusoidal least square fitting is used, which is based on fitting a sinusoidal function to the data of each pixel. As mentioned in chapter 2.4.5, phase stepping jitter can cause fringe artifacts in the processed modalities. Therefore, it is necessary to optimize the actual grating position for each phase-step using an EM. The second PP processing algorithm combines the PPLS with an additional EM. Hence, in the following sections it will be called periodic polynomial expectation maximization (PPEM). The PPEM first performs

an initial PPLS processing. Subsequently, an EM step where stepping jitter is corrected by minimizing the residual sum of squares (RSS) for each phase-step is performed. This is followed by again fitting $I^{PP}_{\varphi,I_{min},A,\sigma}(\phi)$ to the data of each pixel using the updated phase positions. These two steps are repeated until a previously defined convergence criterion is met. Here, the 99.9% percentile of the phase change between two iterations was chosen to less than 0.0001 as convergence criterion. The PPEM is mainly compared to a sinusoidal expectation maximization (SEM) processing.

6.2.3 Periodic artifacts

As mentioned above, even for sinusoidal intensity modulations imprecise phase-steps can induce periodic artifacts in the three extracted modalities. Since for non-sinusoidal intensity modulations the measured values do not match the theoretically expected values, too (even with precise phase steps), similar artifacts can be expected. Further, the obtained values for transmission, visibility, and differential phase will depend on the phase position in a pixel and on the number of steps. This effect can additionally manifest itself for different intensity modulation shapes in artifacts with different intensity and/or appearance. The period of these artifacts is determined on the one hand by the period of the intensity pattern on the detector (e.g. Moiré fringe pattern). On the other hand, the number of phase steps N is decisive. For equidistant phase steps, the measured sampling points repeat themselves after $1/N$ of the fringe pattern period (just shifted by a multiple of the phase $2\pi/N$). Therefore, the period of the occurring artifacts is given by $1/N$ of the fringe pattern period. In the following, these artifacts are referred to as sampling artifacts.

To compare the frequency and power of periodic artifacts between different processing algorithms, Fourier analysis is used in the following sections. In a first step, the mean signal value of the region of interest is subtracted since only the signal variations are of interest. Followed by a discreet Fourier transformation of all line profiles in the examined region. The resulting frequency spectra of all line profiles are averaged to archive better statistics. The frequency of the detector fringe pattern f_0 is chosen as reference frequency and is thus set to 1. Note that the Fourier analysis is not a direct measure of how well the used model resembles the intensity modulation like the RSS.

6.3 Simulation

Based on simulated datasets, the performance of the PP approach is compared with sinusoidal processing. Here, first the procedure for the simulation of the data sets is described, followed by the comparison of the four processing algorithms.

6.3.1 Simulation of the Grating Interferometer Data

For the simulation of the datasets, the intensity modulation was first calculated numerically for each imaging system. For this purpose, binary profiles were convolved with DCs corresponding to the gratings of the system. For systems without an analyzer grating and/or no source grating, an additional convolution with a Gaussian was applied to account for source blurring and the detector PSF, respectively. To evaluate the influence of phase-stepping and the fringe pattern, the obtained intensity modulation was translated into a dataset with 300×200 pixels and N equidistant phase steps. In addition, a phase offset along the detector was added, resulting in a Moiré fringe pattern with a period of 30 pixels. Further, to investigate the influence of object-related artifacts, an object acquisition with absorbing, scattering and phase-shifting objects was simulated. A homogeneous and purely phase-shifting sphere is placed on the right side of the array. Its differential phase shift was calculated by the derivative of its local thickness [Weitkamp, 2005]. To visualize the interference of potential artifacts with the sample in a reasonable grey value windowing the resulting maximal phase shift φ at the borders of the sphere was set to $\pm 0.06\pi$. On the left side of the array a absorption wedge and a overlaying scattering wedge were included. For the absorbing wedge, the intensity modulation was simply multiplied by a factor $\leqslant 1$ and $\geqslant 0.01$, with a linear decrease from right to left. The scattering wedge is characterized by an increasing scattering strength from top to bottom and was calculated by convolving the intensity modulation with Gaussians of increasing σ from 0 to 0.4 times the period.

As already mentioned, it is difficult to perform error-free phase stepping in real measurements due to hardware inaccuracies. To account for the resulting phase-stepping jitter, an additional random phase offset distributed with a standard deviation of 0.01π was introduced in each detector frame. A deviation in the stepping position of this magnitude for a grating with 10 µm period would result in a deviation of ± 50 nm, which is a realistic value for the precision of a medium quality linear stage. Since the main objective in this chapter is to compare the different processing algorithms and investigate artifacts due to non-sinusoidal intensity modulations, no photon noise was added to the simulated images.

To evaluate the performance of the PP model compared to sinusoidal signal-retrieval, in the following sections three exemplary imaging systems with different numbers of gratings and grating DCs as shown in Table 6.1 are simulated. Unless otherwise stated, 5 equidistant phase steps were used for this purpose.

System	Source/Detector PSF σ	G_0 DC	G_1 DC	G_2 DC
3-gratings	-	0.2	0.5	0.4
2-gratings	0.05	-	0.333	0.4
1-grating	0.02	-	0.5	-

Table 6.1: System parameters for the three simulated systems. The source size or detector Point Spread Function (PSF) is a Gaussian and its standard deviations σ are given in multiples of the period.

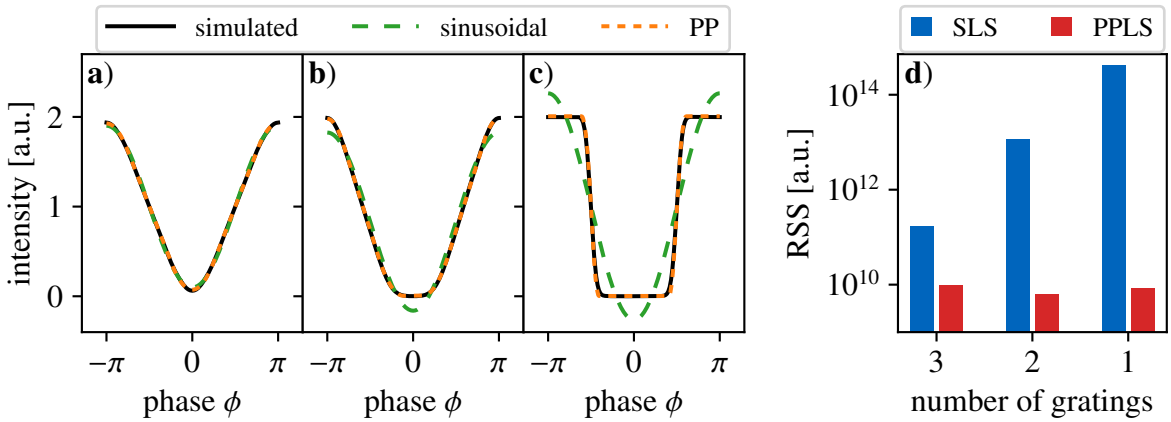

Figure 6.4: Simulated intensity modulations and fitted curves using a sinusoidal function and I^{PP} for **a)** a 3-grating interferometer, **b)** 2-grating interferometer, and **c)** 1-grating interferometer. **d)** The residual sum of squares (RSS) of the reference processing for sinusoidal least square (SLS), and periodic polynomial least square (PPLS) of the entire dataset for the three interferometers in **a)** – **c)** simulated with 100 equidistant steps and no additional phase-stepping jitter (figure adapted from [Pinzek, 2021b]).

6.3.2 Comparison of Sinusoidal and PP Approach for Interferometric intensity modulations

First, the fitting performance of the sinusoidal and PP approaches without the influence of sampling-related artifacts will be compared. For each of the three systems described in table 6.1, a dataset with 100 equidistant and precise steps (without phase stepping jitter) is simulated. The accuracy of the fits is determined firstly by observing differences between fitted and simulated intensity modulations (Figure 6.4 **a)** – **c)**), and secondly by calculating the RSS on the entire dataset processed by the SLS and the PPLS (Figure 6.4 **d)**).

As expected, in case of the three-grating interferometer in Figure 6.4 **a)** both approaches match the simulated intensity modulation well. In the case of the rather trapezoidal intensity modulation of the two-grating interferometer in Figure 6.4 **b)**, however, a difference between the two approaches is already recognizable. While the linear part of the intensity modulation is well described by both approaches, the sinusoidal approach underestimates the maximum and minimum values. The PP approach, on the other hand, can successfully adapt its shape to the simulated intensity modulation by adjusting the transition points δ_0 to δ_3. In the third example in Figure 6.4 **c)** with an almost rectangular shaped intensity modulation this behavior is even more apparent. The sinusoidal model overestimates the peaks and underestimates the minimum drastically, while the PP function again reproduces the simulated shape robustly. The same trend can be seen in Fig d) referring to the RSS. The RSS of the PPLS is much smaller than for the SLS, which could be expected to some extent, as the PPLS optimizes one more free parameter than the SLS. However, while the RSS of the SLS increases the more the intensity modulation deviates from a sinusoidal shape, The RSS of the PPLS

remains almost constant for sinusoidal, trapezoidal, and rectangular intensity modulations, confirming its robustness for different shapes.

6.3.3 Periodic Fringe Artifacts Due to Sampling and Phase-Stepping Jitter

To examine artifacts related to sampling arising from the sinusoidal and PP approach, two datasets were simulated with five equidistant phase steps for the previous discussed two-grating system. The first dataset with precise phase steps was processed with SLS and PPLS. For the second dataset, additional phase-stepping jitter was simulated. To account for the imprecise phase step positions, processing was therefore performed with SLS and PPLS, but also with SEM and PPEM.

Simulated 2-Grating Interferometer with Precise Step Positions

To get an impression of the sampling-related artifacts, the fitted object phase $\varphi_{\text{fit}}^{\text{obj}}$ was processed with the ground truth reference phase $\varphi_{\text{gt}}^{\text{ref}}$ and is shown in Figure 6.5 **a)** for the SLS and in **c)** for the PPLS algorithm. Strong fringe artifacts are observable for the SLS, while the PPLS significantly reduces these artifacts. This is also confirmed by the respective Fourier spectra in Figure 6.5 **e)**. Only within the scatter wedge in Figure 6.5 **a)**, the fringe artifacts disappear with increasing scattering strength since the intensity modulation becomes more and more sinusoidal. A complimentary picture of the artifacts appears in Figure 6.5 **b)** where the fitted reference phase $\varphi_{\text{fit}}^{\text{ref}}$ was used for processing the differential-phase contrast (DPC) images. Here, strong artifacts are visible in the region of the scattering wedge, whereas the background reveals no fringe artifacts (also indicated by the corresponding Fourier spectra). Since reference and object acquisition possess identical phase biases, they cancel each other out in the background. However, in the region of the scattering wedge the biased reference is subtracted from the artifact-free sample phase leading to strong fringe artifacts. Similar fringe artifacts are also present in the phase signal of the sphere since the phase in both, the reference, as well as the object image, is affected by sampling artifacts. The same effect is observed for the PPLS in Figure 6.5 **d)**. As for the background artifacts in Figure 6.5 **c)**, in the area of the objects the artifacts are significantly reduced compared to the SLS due to the improved fitting accuracy for non-sinusoidal intensity modulations of the PP approach.

Simulated 2-Grating Interferometer with Phase-Stepping Jitter

In real measurements phase stepping is usually not precisely reproducible. Therefore, sampling related artifacts differ between object and reference acquisition and thus do not cancel each other out as in the previous example with precise phase steps. To investigate the behav-

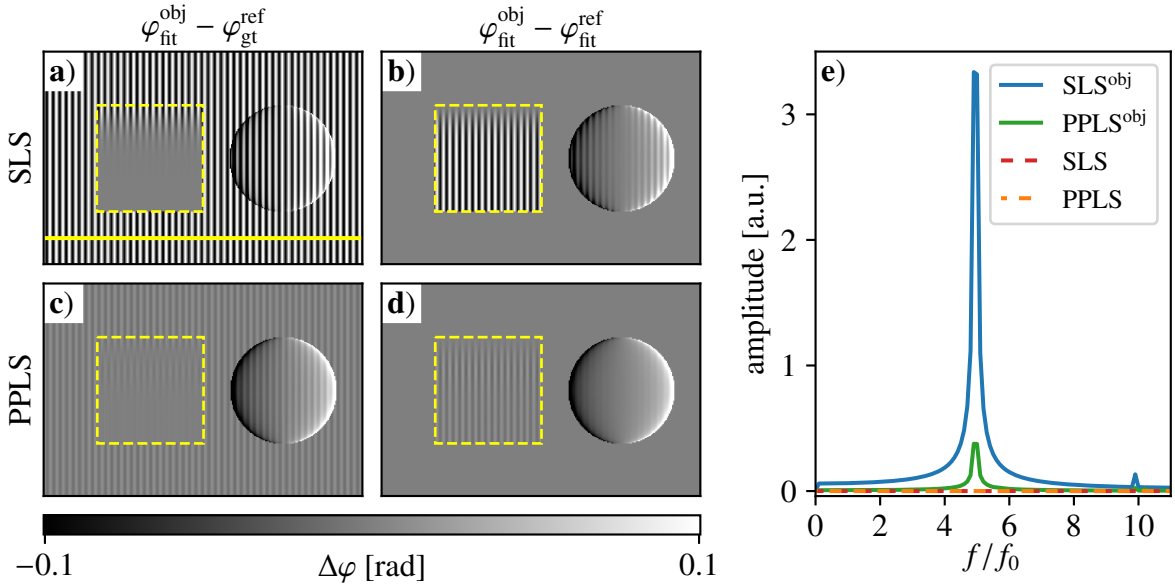

Figure 6.5: Comparison of processed differential-phase contrast (DPC) images with sinusoidal least square (SLS) and periodic polynomial least square (PPLS) fitting in case of precise phase steps. In **a)** and **c)** the object image phase ($\varphi_{\mathrm{fit}}^{\mathrm{obj}}$) is processed with the ground truth reference phase ($\varphi_{\mathrm{gt}}^{\mathrm{ref}}$) to visualize sampling artifacts for the SLS and PPLS respectively. In **b)** and **d)** the DPC images are processed with fitted reference phase ($\varphi_{\mathrm{fit}}^{\mathrm{ref}}$), respectively. The yellow dashed squares mark the region with a scatter wedge with increasing scattering strength from top to bottom. Note that the images are windowed narrowly to visualize the fringe artifacts. **e)** Corresponding Fourier spectra generated along the yellow line in **a)** (figure adapted from [Pinzek, 2021b]).

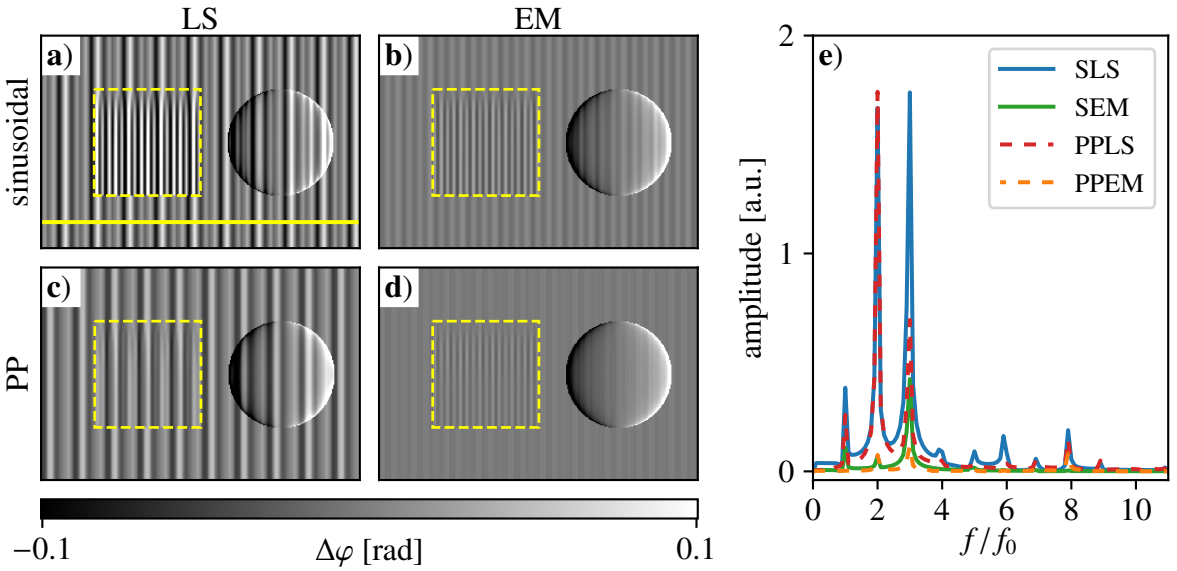

Figure 6.6: Processed differential-phase contrast images for **a)** sinusoidal least square (SLS), **b)** sinusoidal expectation maximization (SEM), **c)** periodic polynomial least square (PPLS), and **d)** periodic polynomial expectation maximization (PPEM) of the simulated two-grating interferometer with phase-stepping jitter. The yellow dashed squares mark the region with a combined attenuating and scattering wedge with increasing absorption from left to right and increasing scattering strength from top to bottom. **e)** Corresponding Fourier spectra generated along the yellow line in **a)** (figure adapted from [Pinzek, 2021b]).

ior of sinusoidal and PP approach in presence of phase jitter, processed DPC images of the same system as before with additional phase-stepping jitter are shown in Figure 6.6 **a)** – **d)**. All images were processed with fitted reference data, which were affected by phase jitter as well. Additionally to the SLS and PPLS considered in the previous section, the SEM and the PPEM are also considered for processing. A complex fringe artifact pattern appears for the conventional SLS in Figure 6.6 **a)** as different types of artifacts superimpose. Most of these artificial frequencies are removed when the SEM processing (Figure 6.6 **b)**) is applied as illustarted by the Fuorier spectra in Figure 6.6 **e)**. The PPLS (Figure 6.6 **c)**) reveals comparable artifacts as the SLS even so it considers the non-sinusoidal shape of the intensity modulation. The best result with the lowest amount of artifacts is obtained with the PPEM in Figure 6.6 **d)**, which combines the PP fitting with an EM-based phase jitter correction. Hence, fringe artifacts due to non-sinusoidal intensity modulations and related sampling artifacts should be distinguished from phase-stepping jitter and corrected separately if necessary.

As already observed in section 6.3.2, the amplitude of non-sinusoidal intensity modulations is not fitted accurately by the sinusoidal models even with a high number of sampling points. Hence, with a low number of phase steps it is assumed that the fitted amplitude will be over- and underestimated in different pixels, leading to similar sampling-related fringe artifacts in

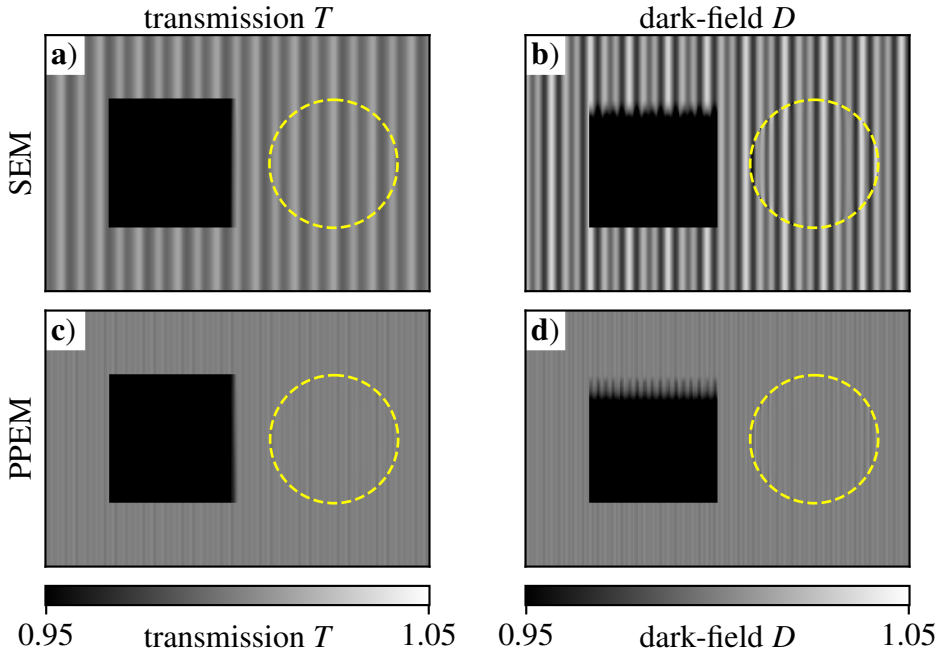

Figure 6.7: Processed transmission images for **a)** SEM and **c)** PPEM, respectively. **b)** and **d)** show the dark-field images processed with the SEM and the PPEM, respectively. The yellow dashed circles mark the region with a purely phase shifting sphere. A more detailed comparison concluding SLS and PPLS (comparable with Figure 6.6) is given in appendix B

the transmission and dark-field modality as in the DPC images. Since it has been shown for the DPC images that a dedicated correction for non-sinusoidal intensity modulations is not sufficient to significantly reduce the artifacts, only the SEM and the PPEM are compared in Figure 6.7 for the transmission and dark-field modality. For the SEM in for both modalities in Figure 6.7 **a)** and **b)** strong fringe artifacts are visible, whereas processing with the PPEM (Figure 6.7 **c)** and **d)**) clearly reduces these artifacts. This demonstrates that a combination of adapted intensity modulation shape and phase jitter correction can successfully reduce periodic artifacts in all three image modalities.

So far, the performance of the four algorithms has only been evaluated for 5 phase steps. Next, their performance will be considered depending on the number of phase steps during acquisition. Therefore, the root-mean-square (RMS) of the difference between the fitted and ground truth DPC images ($\Delta\varphi_{\text{fit}}$ and $\Delta\varphi_{\text{gt}}$) of the two-grating interferometer is determined. For each number of phase steps ten datasets were simulated and processed in the range from three (SLS and SEM) and four (PPLS and PPEM) phase steps, respectively, up to 20 phase steps. Afterwards, the RMS was averaged for each number of phase steps and each of the four processing algorithms. The resulting RMS is plotted for all four algorithms in Figure 6.8. For SLS and PPLS, a slow decrease in the RMS can be seen, whereas the PPLS is always below the SLS. In contrast, SEM and PPEM show a steep decline for small numbers of phase steps which flattens for larger numbers of phase steps. For five or more phase steps, the RMS of the PPEM is below the SEM and therefore performs superiorly in terms

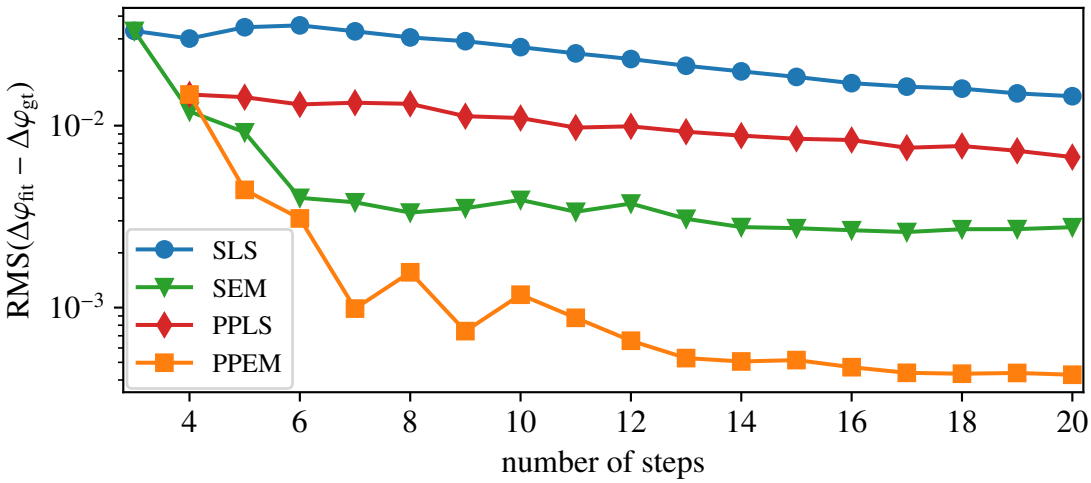

Figure 6.8: Root-mean-square (RMS) of the difference between the fitted and ground truth differential-phase contrast images ($\Delta\varphi_{\text{fit}}$ and $\Delta\varphi_{\text{gt}}$) of the 2-grating interferometer over the number of phase steps for all four processing algorithms (figure adapted from [Pinzek, 2021b]).

of sampling artifact reduction. Similar behavior is found for transmission and dark-field, for which RMS curves are plotted in appendix B.

6.4 Experimental

In the following, two different experimental examples are presented to test the newly proposed processing model. Therefore, measurements with an X-ray and a neutron grating interferometer were conducted. The acquired datasets were processed using the SLS, SEM, PPLS, and PPEM, to demonstrate that the PP approach also leads to a reduction of sampling-related artifacts on experimental data.

6.4.1 Data acquisition

First, a single phase-grating setup with an asymmetric DC is discussed. The scans were acquired at the beamline P05 at Petra III/DESY (Hamburg, Germany) [Wilde, 2016] using highly coherent X-ray synchrotron radiation generated by an undulator source and monochromatized by a double crystal monochromator at 15 keV. The silicon grating (period: 5 µm, DC $\approx 2/3$, height: ≈ 25 µm) had a binary profile fabricated by anisotropic potassium hydroxide etching. It acted as a $4/3\pi$ shift array, producing an asymmetric modulation at around $1/6$ of the Talbot distance. The diffraction pattern was directly recorded by a high-resolution CMOS camera that was focused on a 50 µm thick lutetium–aluminium garnet (LuAG) scintillator with 10× optical magnification, resulting in a pixel size of 0.64 µm. In total, 12 phase

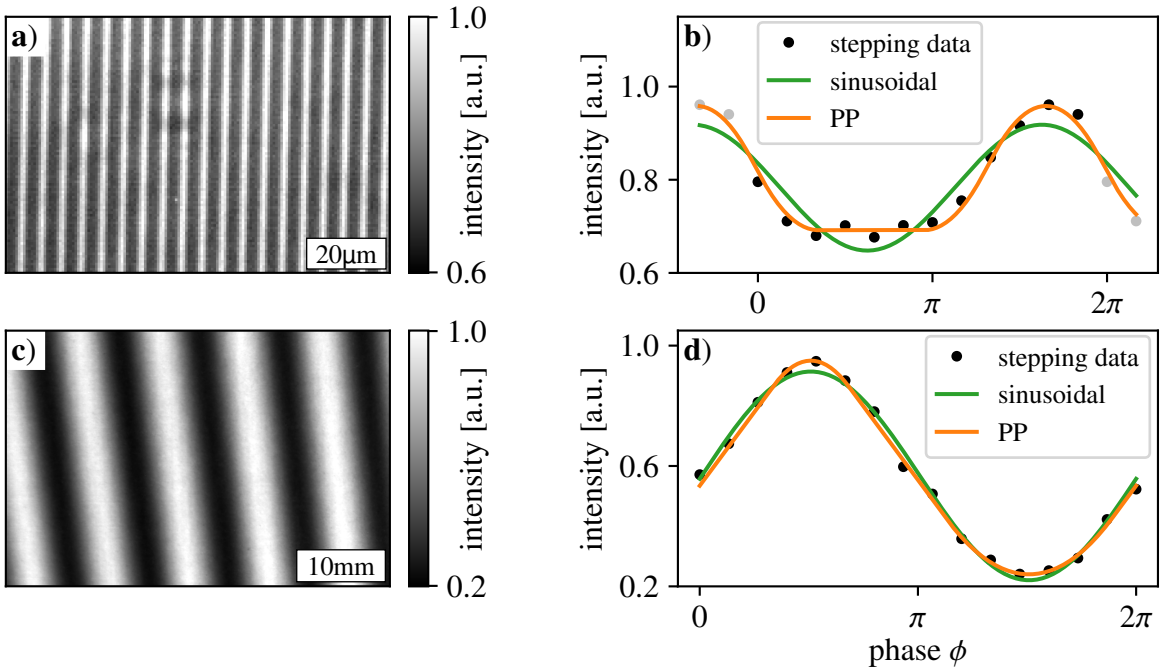

Figure 6.9: Detector image of a reference intensity modulation for the **a)** 1-grating X-ray interferometer and **c)** 3-grating neutron interferometer. Measured stepping data and fitted curves using a sinusoidal function and I^{PP} of a single detector pixel for the **b)** 1-grating X-ray interferometer and **d)** 3-grating neutron interferometer. For a better visualization in **b)**, the stepping data were periodically continued in both directions (gray markers) (figure adapted from [Pinzek, 2021b]).

steps ranging over one period were acquired with an exposure time of 200 ms per frame for the sample and the reference scan. A detector image of the reference scan and the stepping data of a single pixel (Figure 6.9 **a)** and **b)**) reveal the non-sinusoidal nature of the measured intensity modulation clearly. The sample shown in Figure 6.10 consists of full and hollow silica (SiO_2) spheres with several tens of µm in diameter.

As another example a three-grating Talbot-Lau interferometer implemented at the ANTARES beamline at FRM II (Garching, Germany) [Schulz, 2015] was chosen. The setup was operated with a neutron velocity selector providing quasi monochromatic neutron radiation of 4 Å ($\Delta\lambda/\lambda = 10\%$). Unlike typical Talbot–Lau systems operating with laboratory X-ray sources with polychromatic spectra, it is to expect that the modulation produced by the G_1 is rather more rectangular than sinusoidal. Furthermore, a source grating G_0 with a DC of 0.7 was used to increase the visibility and the DC of the G_2 was 0.55 due to fabrication-related deficiencies. The interferometer geometry is asymmetric to keep the distance of the sample to the detector as low as possible and avoid geometric source blur. The period of the G_1 grating is 24.4 µm, and the linear stage used for its stepping (MFA-PPD, Newport Corporation, Irvine, US) has a typical bi-directional repeatability of 0.2 µm according to the manufacturer. In this example, a phase stepping with 16 steps each with 20 s exposure time was performed. A detector image of the reference scan and the stepping data of a single pixel

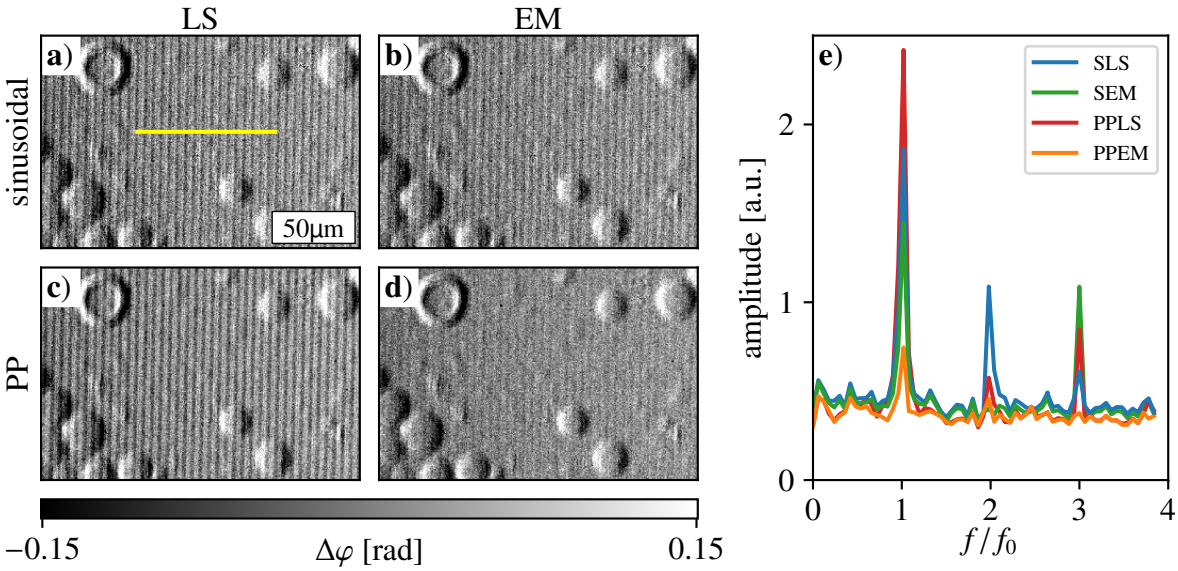

Figure 6.10: Differential-phase contrast images processed by **a)** sinusoidal least square (SLS), **b)** sinusoidal expectation maximization (SEM), **c)** periodic polynomial least square (PPLS), and **d)** periodic polynomial expectation maximization (PPEM) from a single grating X-ray interferometer. **e)** Fourier spectra for the respective processing schemes averaged from 50 pixel rows next to the yellow line in **a)** (figure adapted from [Pinzek, 2021b]).

(Figure 6.9 **c)** and **d)**) reveal a slight deviation of the measured intensity modulation from a sinusoidal shape. It is found that an EM-based determination and correction of the stepping positions was necessary in this case as well to avoid fringe artifacts. The imaged sample (shown in Figure 6.12 and Figure 6.13) was a logo of the ANTARES beamline engraved into an aluminum sheet. Further details on the geometry, grating properties, used hardware and overall performance of the instrument can be found in [Neuwirth, 2020; Gustschin, 2018].

6.4.2 Data Processing

Single Grating X-ray Interferometer

Figure 6.10 **a)** – **d)** show the DPC images of the single phase grating X-ray interferometer processed by the four previously discussed processing algorithms and respective Fourier spectra of the periodic artifacts are given in Figure 6.10 **e)**. Due to the asymmetric and non-sinusoidal intensity modulation, strong fringe artifacts appear for SLS processing (see Figure 6.10 **a)**). Since neither SEM (Figure 6.10 **b)**) nor PPLS (Figure 6.10 **c)**) clearly reduce the artifacts, it can be assumed that both phase-stepping jitter and the non-sinusoidal intensity modulations are present. Only the processing with the PPEM reduces the artifacts significantly as it considers both effects. However, some residual fringes still remain as the

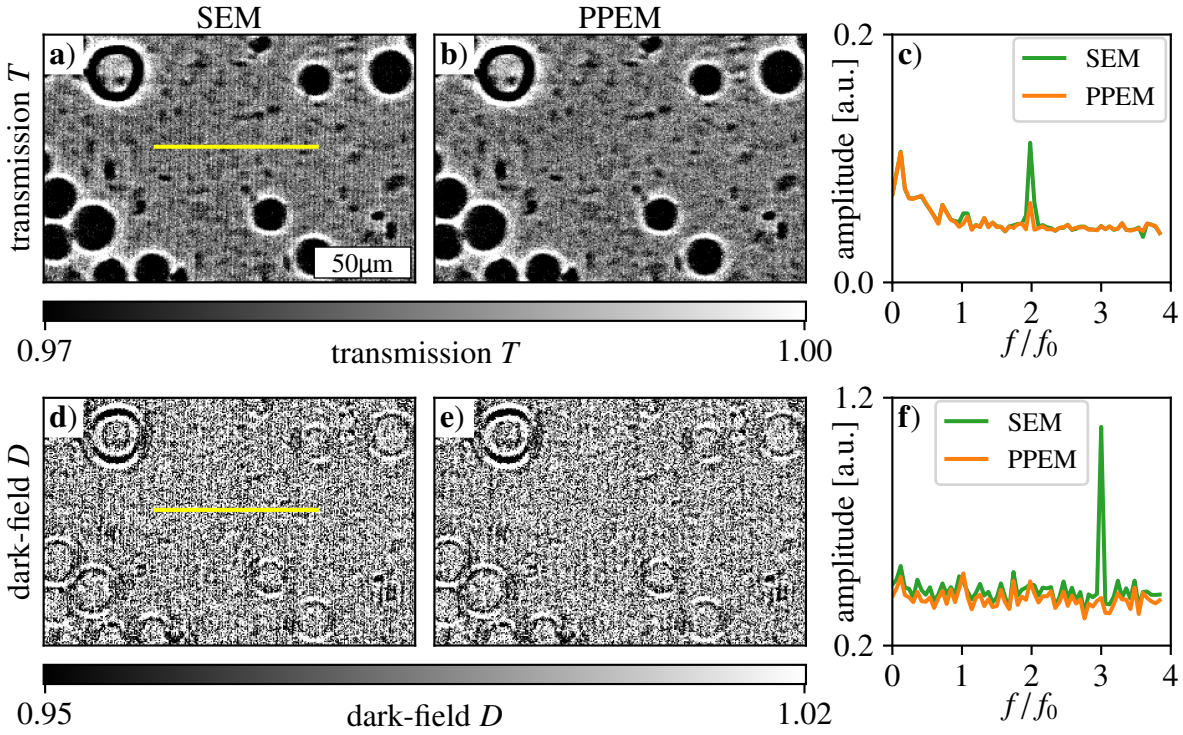

Figure 6.11: Transmission and dark-field images from the single grating X-ray interferometer processed by **a)** and **d)** sinusoidal expectation maximization (SEM), and **b)** and **e)** periodic polynomial expectation maximization (PPEM), respectively. **c)** and **f)** display corresponding Fourier spectra averaged from 50 pixel rows next to the yellow line in **a)**.

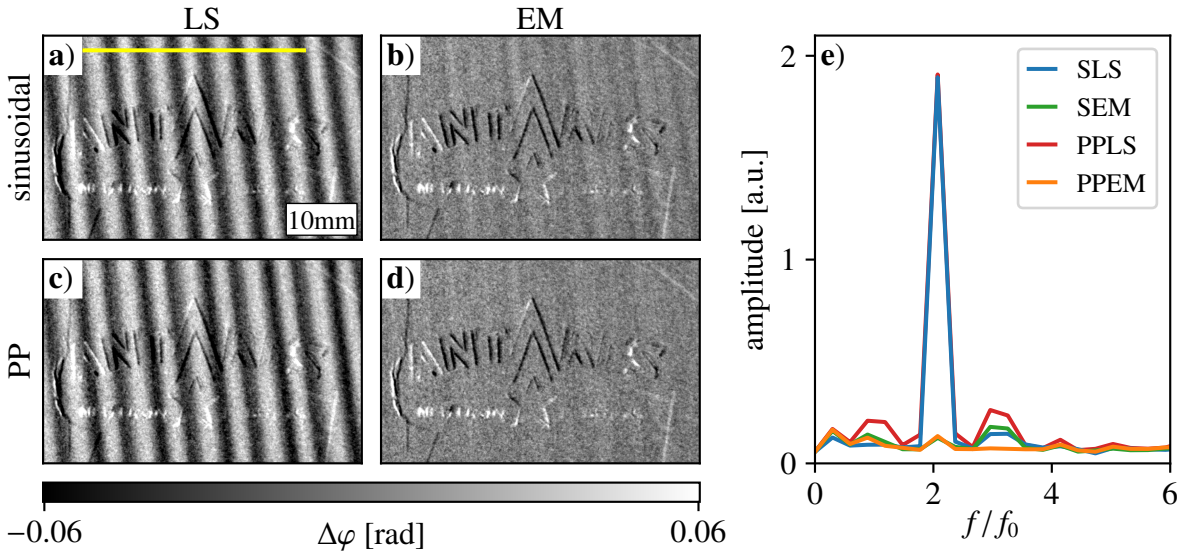

Figure 6.12: Differential-phase contrast images processed by **a)** sinusoidal least square (SLS), **b)** sinusoidal expectation maximization (SEM), **c)** periodic polynomial least square (PPLS), and **d)** periodic polynomial expectation maximization (PPEM) for the dataset measured at the Antares neutron beamline. **e)** Fourier spectra for the four algorithms averaged about 60 pixel lines along the yellow line in **a)**.

Fourier spectrum reveals. Nevertheless, they are less pronounced compared to the background noise level.

As already demonstrated for the simulated data, the PP approach can also reduce artifacts in the transmission and dark-field modalities. Since phase-stepping jitter is present in this dataset, Figure 6.11 shows only transmission and dark-field images processed by SEM and PPEM and respective Fourier spectra (graphics including also SLS and PPLS are given in appendix B). For the transmission images (Figure 6.11 **a)** and **b)**), owing to the noise that is present in the images, the difference is not as clearly visible as it is for the simulated data. In the Fourier spectrum (Figure 6.11 **c)**) it is apparent that the amplitude of the artifacts has been significantly reduced by the PPEM. The situation is similar for the dark field in Figure 6.11 **d) – f)**, although the influence of the noise is even more pronounced.

Neutron Talbot–Lau Interferometer

Also for the three grating neutron Talbot–Lau interferometer with its intensity modulation which deviates only slightly from a sinusoidal shape, the PP approach successfully reduces periodic artifacts. Figure 6.12 compares the four examined processing algorithms in the DPC modality. The image acquisition was strongly affected by phase-stepping jitter as already SEM (Figure 6.12 **b)**) brings a drastic improvement compared to SLS **a)** and PPLS

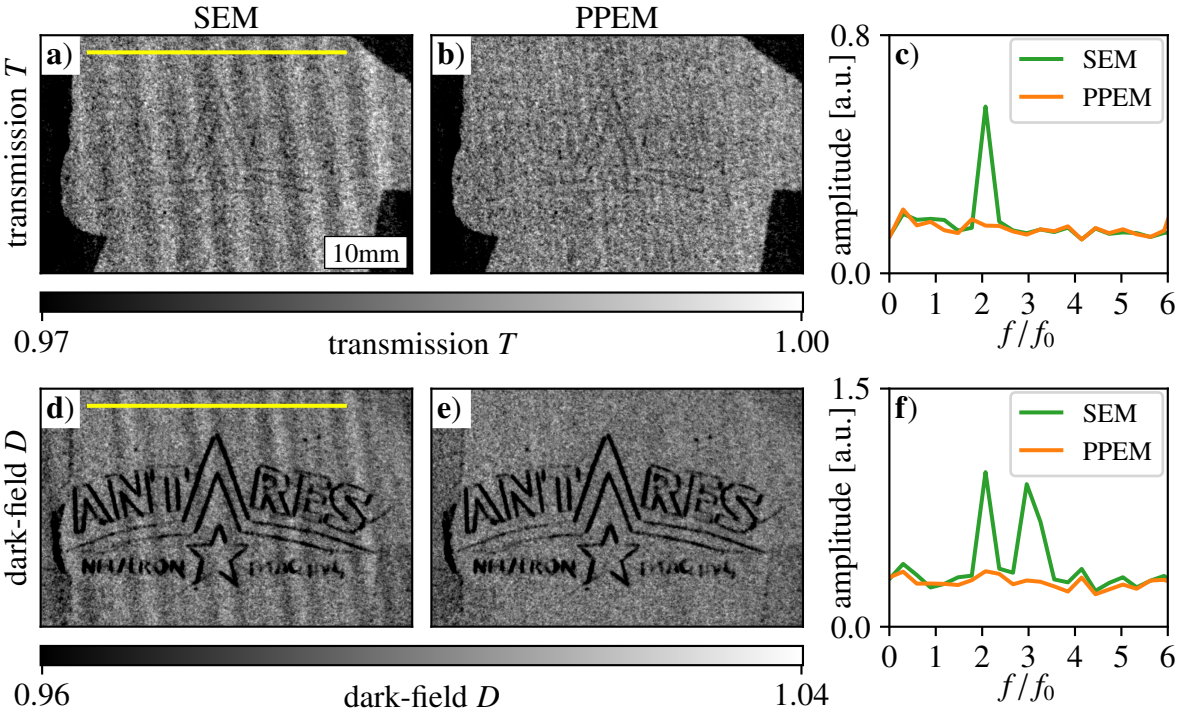

Figure 6.13: Transmission and dark-field images from the Antares neutron beamline processed by **a)** and **d)** sinusoidal expectation maximization (SEM), and **b)** and **e)** periodic polynomial expectation maximization (PPEM), respectively. **c)** and **f)** display corresponding Fourier spectra averaged from 60 pixel rows next to the yellow line in **a)**.

c) and only weak artifacts in the background remain. However, the PPEM (Figure 6.12 **d)**) again shows the best result, as it also removes the remaining fringes by considering both phase-stepping jitter and non-sinusoidal intensity modulation. The Fourier analysis shown in Figure 6.12 **e)** also reveals that the amplitude of the individual artifact frequencies is lowest for the PPEM.

A similar situation can be seen for the two other image modalities: transmission and dark-field. In Figure 6.13 only the images processed by SEM and PPEM are shown since the DPC images already revealed strong phase-stepping jitter (a comparison of all four processing schemes is given in appendix B). For both modalities a clear artifact reduction is observed when the processing is performed with the PPEM. This is also confirmed by the Fourier spectra in Figure 6.13 **c)** and **f)**.

6.5 Summary

In this chapter an alternative polynomial piece-wise defined function is introduced which allows to model intensity modulations, reproducing their physical origin from several convolutions with binary intensity profiles. This PP function is capable of handling symmetric and asymmetric intensity modulations from interferometric and non-interferometric origin recorded in a phase-stepping process. The performance of the PP approach is compared to conventional sinusoidal processing using LS fitting based on simulated imaging systems with 1 to 3 gratings with different DCs. It is shown that sampling related artifacts occur in the DPC images when non-sinusoidal intensity modulations are processed with conventional sinusoidal models. Although these artifacts originate from non-sinusoidal intensity modulations, they are comparable to phase-stepping jitter artifacts. To distinguish both, the sinusoidal (SEM) and PP (PPEM) approach are combined with an EM algorithm that corrects for phase-stepping positions employing the entire interferogram. Based on simulations it is found that even small phase-stepping deviations (jitter) create more severe artifacts than the discrepancies between the non-sinusoidal intensity modulation and the sinusoidal assumption. Nevertheless, for acquisitions with five and more phase steps, the PPEM performs superior to the SEM since it successfully corrects for jitter and almost completely eliminates residual fringe artifacts originating from non-sinusoidal intensity modulations. Consistent behavior is found in all three imaging modalities as well as for the experimental data acquired with a single grating and a Talbot–Lau interferometer.

7 Conclusion and outlook

In chapter 4, it was demonstrated that it is feasible to fabricate X-ray absorption gratings based on micro-particles that are comparable to state-off-the-art absorption gratings. To achieve this, tungsten micro-particles of two different sizes were mixed into a bimodal mixture and were deposited by centrifugation into high aspect ratio grating structures. It was shown that the bimodal particle mixture of different sizes increases the filling ratio. Further, it was demonstrated that large area gratings with trench depths of 450 µm and periods of 45 µm can be centrifuged without damaging the grating structure. Thus, a 170 mm × 38 mm-sized absorption grating with an effective tungsten height of 207 µm was fabricated. In the characterization of this grating it was shown that it is competitive to state of the art LIGA gratings. Therefore, the presented micro-particle approach is a promising method for the fabrication of X-ray absorption gratings. Especially since the main bottleneck for a clinical applications of X-ray phase-contrast and dark-field imaging remains the fabrication of the required absorption gratings. For complete coverage of the field of view of e.g. a thorax radiography system or a CT scanner, the G_2 grating poses the most effort and cost. Hence, research towards reliable and cost-effective fabrication techniques such as the one presented here should gain priority. For inverse Talbot–Lau systems source gratings with very small periods and extremely high aspect ratios are required [Donath, 2009]. Therefore, the next goal becomes to downscale the described particle deposition process to a period in the range of 10 µm to 20 µm while maintaining the effective tungsten absorbing thicknesses above 200 µm. However, fabrication of suitable silicon templates with even higher aspect ratios requires a precise profile control in DRIE to maintain a constant duty cycle. Furthermore, grating lamellae with smaller periods might stick to each other due to capillary forces introduced by the fluids or break due to the centrifugal forces. To address these stability issues the grating lines can be connected by supporting bridge structures similar to LIGA-based gratings. A further challenge might be a reduced particle filling density when smaller particles are used. To cope with that the particle suspension has to be optimized with a focus on surface-related interparticle interactions. However, especially for gratings with small periods and source gratings with their small bending radii other advanced technologies like LIGA with their dense trench filling by electroplating gold are indispensable. Furthermore, flexible substrates like graphite are compatible with LIGA and allow to create gratings that can be bent to radii down to 100 mm which is necessary for compact systems. However, for analyzer gratings with their large active area material cost become more important. At the same time, requirements regarding period and aspect ratio are more relaxed in inverse Talbot–Lau systems. For these gratings, the here presented low-cost fabrication method based on the deposition of tungsten particles is a promising alternative. Reaching good absorbing performance with periods in the sub-20 µm length scale would allow producing cost-effective and sufficiently sensitive

systems for e.g. thorax dark-field radiography, which recently demonstrated its first clinical application [Willer, 2021].

In chapter 5 the fabrication of X-ray gratings using deep X-ray lithography at a conventional X-ray tube was successfully demonstrated. Conventional X-ray tubes offer the capability to produce X-ray absorption gratings with the LIGA method independently of synchrotron facilities. The step from synchrotron to conventional X-ray tubes comes with the drawback of longer exposure times due to lower flux but has the advantage that X-ray tubes are more available and cost-efficient. A series of problems caused by the changed beam geometry compared to a synchrotron source were solved in this thesis. By bending the mask, the increased mask absorption at the edges could be prevented, resulting in a uniform dose deposition over the entire substrate area. By simultaneously bending the substrate, structure inclination parallel to the bending axis can be reduced. Along the axis around which mask and substrate were not bent a gradient can not be prevented but depending on the application, this effect might be beneficial. Thus, a 66 mm × 66 mm-sized grating structure with a resit height of 110 µm and a period of 10 µm was fabricated with a full-field exposure and successfully electroplated with 80 µm gold. However, to produce competitive absorption gratings, it is essential to increase the height of the structures in the future. The comparison of the spectra of the conventional X-ray tube and the LIGA beamline LIGA2 at the KARA synchrotron facility showed that it should be possible to successfully expose the same resist heights as with the conventional direct deep X-ray LIGA process. The large amount of higher energies compared to the synchrotron spectrum, but also the diffuse dose deposition of large source spots can become critical for small structure features. In these cases the tube voltage and anode current could be lowered to reduce the amount of high energies and the size of the source spot, respectively. Both would reduce the flux in the required energy range around 10 keV and thus increase exposure times. To address the long exposure times and the defuse dose deposition in the resist due to the large source spot a better suitable X-ray source could be employed. Modern rotating anode micro-focus X-ray tubes can provide significantly higher X-ray flux compared to the fixed-target X-ray tube we used. Furthermore, the photo-resist could be adapted to improve its dose sensitivity allowing for shorter exposure times.

An alternative processing model for intensity modulations measured in grating interferometry was introduced in chapter 6. This model is based on a polynomial piece-wise defined function, which allows to reproduce the physical origin of these intensity modulations. Based on simulated and experimental data it was shown that this model reduces sampling related artifacts caused by non-sinusoidal intensity modulations. However, it was also found that even small phase-stepping deviations (jitter) create more severe artifacts than the discrepancies between the non-sinusoidal intensity modulation and the sinusoidal assumption. Thus, a combined correction algorithm for phase jitter and non-sinusoidal intensity modulations was proposed. For the processing a high quality reference phase-stepping with a large number of steps should be acquired to determine the fitting parameters which are related to the systems intensity modulation shape. In some cases, spatial variation of grating parameters (e.g., DC) might require determining the shape parameters pixel by pixel. For dose-relevant applications, the sample measurement can be conducted with fewer steps as the fitted parameters from the reference phase-stepping can be reused. Considering all this, the proposed algo-

rithm allows to process a high variety of data from interferometric and non-interferometric systems. Further, it is adaptable to different grating-related circumstances that have not been addressed before. Therefore, it should be considered for grating-based imaging methods operated with multiple gratings and highly coherent sources (e.g., small source spots, monochromatic radiation) or high-resolution detectors, which are prone to non-sinusoidal intensity modulation. Especially when source gratings with small DC or triangular phase gratings that create an asymmetric modulation are used, a thorough analysis and modeling of the intensity modulation should also be performed in case of three-grating interferometers. However, the proposed algorithm comes at the cost of high computational effort since piecewise defined functions with many parameters must be optimized iteratively. Apart from X-ray and neutron grating interferometry, it can be used for many other applications where phase retrieval from non-sinusoidal Moire-patterns is needed.

In this thesis, two different methods for the fabrication of X-ray gratings have been presented, which have the potential to improve the availability of X-ray gratings for grating-based X-ray imaging. In addition, a processing model has been introduced that is able to handle uncommon intensity modulations that can be caused by certain grating configurations.

A Supplementary information of chapter 5

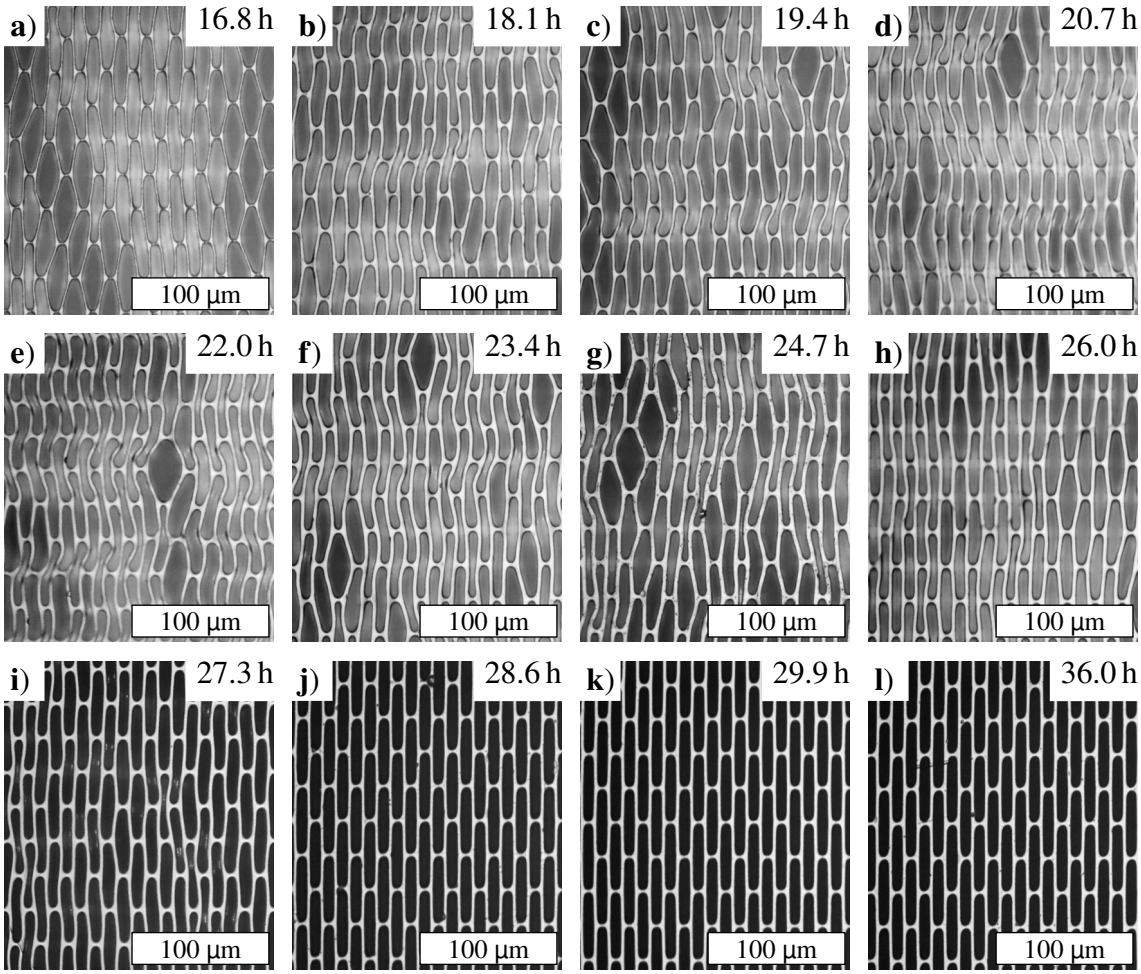

Figure A.1: Microscope images of the developed resist structures for different exposure times between 16.8 h and 36 h.

B Supplementary information of chapter 6

B.1 Simulated data

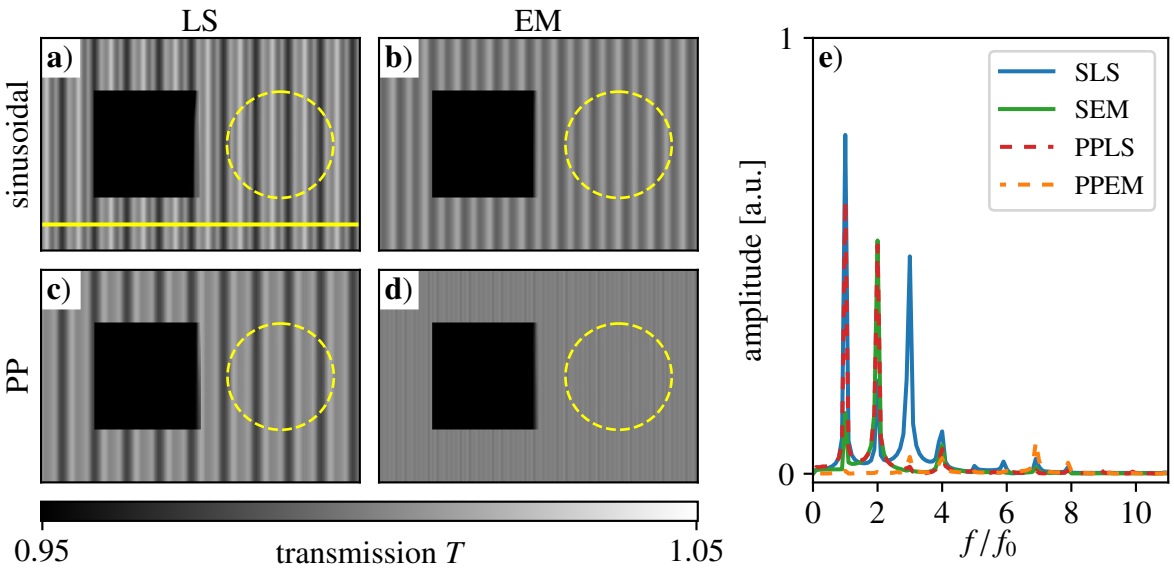

Figure B.1: Processed transmission images for **a)** sinusoidal least square (SLS), **b)** sinusoidal expectation maximization (SEM), **c)** periodic polynomial least square (PPLS), and **d)** periodic polynomial expectation maximization (PPEM) of the simulated two-grating interferometer with phase-stepping jitter. The yellow dashed circles mark the region with a phase-shifting sphere. **e)** Corresponding Fourier spectra generated along the yellow line in **a)**.

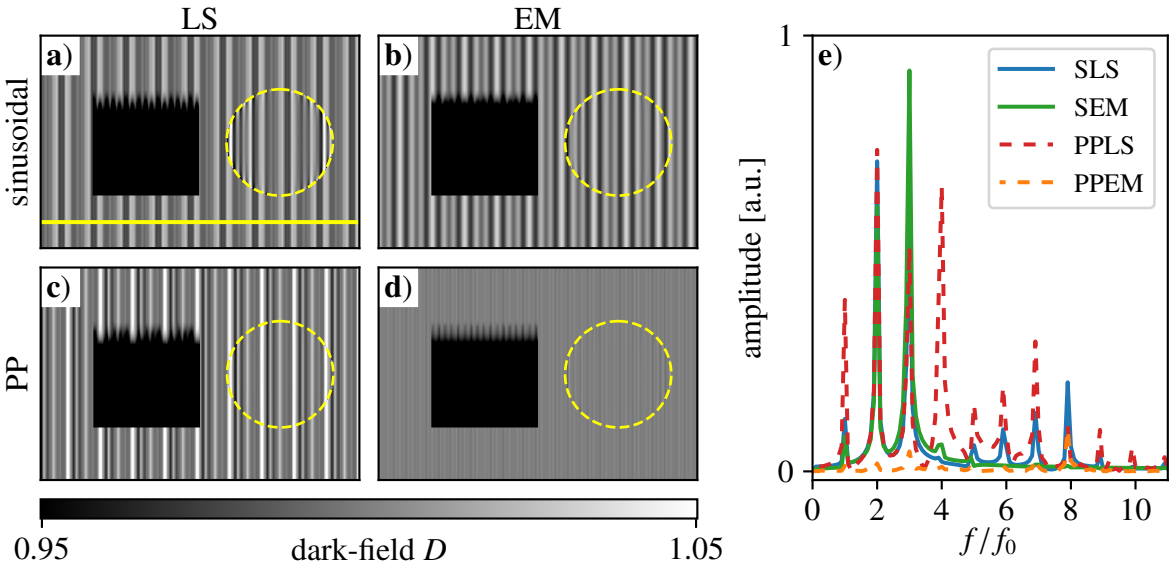

Figure B.2: Processed dark-field contrast images for **a)** sinusoidal least square (SLS), **b)** sinusoidal expectation maximization (SEM), **c)** periodic polynomial least square (PPLS), and **d)** periodic polynomial expectation maximization (PPEM) of the simulated two-grating interferometer with phase-stepping jitter. The yellow dashed circles mark the region with a phase-shifting sphere. **e)** Corresponding Fourier spectra generated along the yellow line in **a)**.

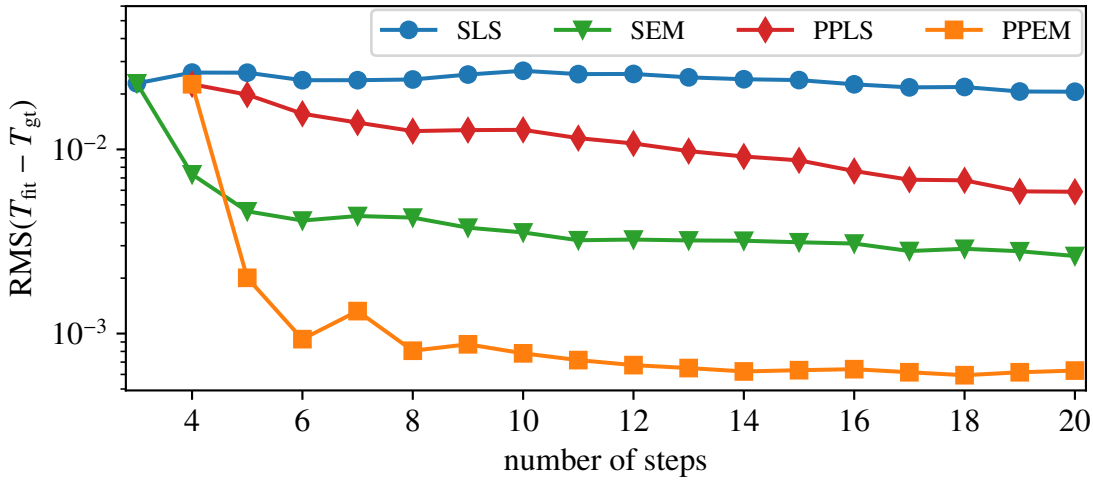

Figure B.3: Root-mean-square (RMS) of the difference between the fitted and ground truth transmission images (T_{fit} and T_{gt}) of the 2-grating interferometer over the number of phase steps for all four processing algorithms.

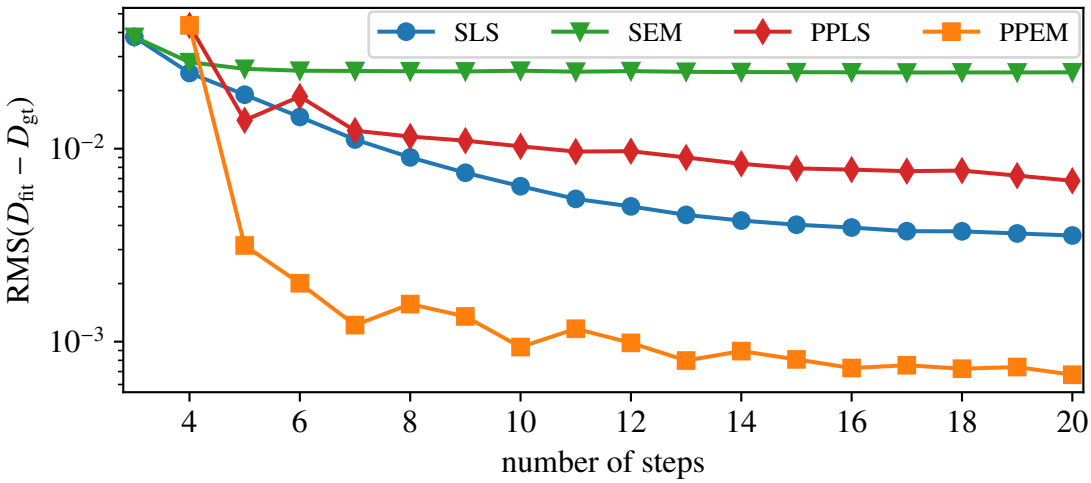

Figure B.4: Root-mean-square (RMS) of the difference between the fitted and ground truth dark-field images (D_{fit} and D_{gt}) of the 2-grating interferometer over the number of phase steps for all four processing algorithms.

B.2 Experimental data

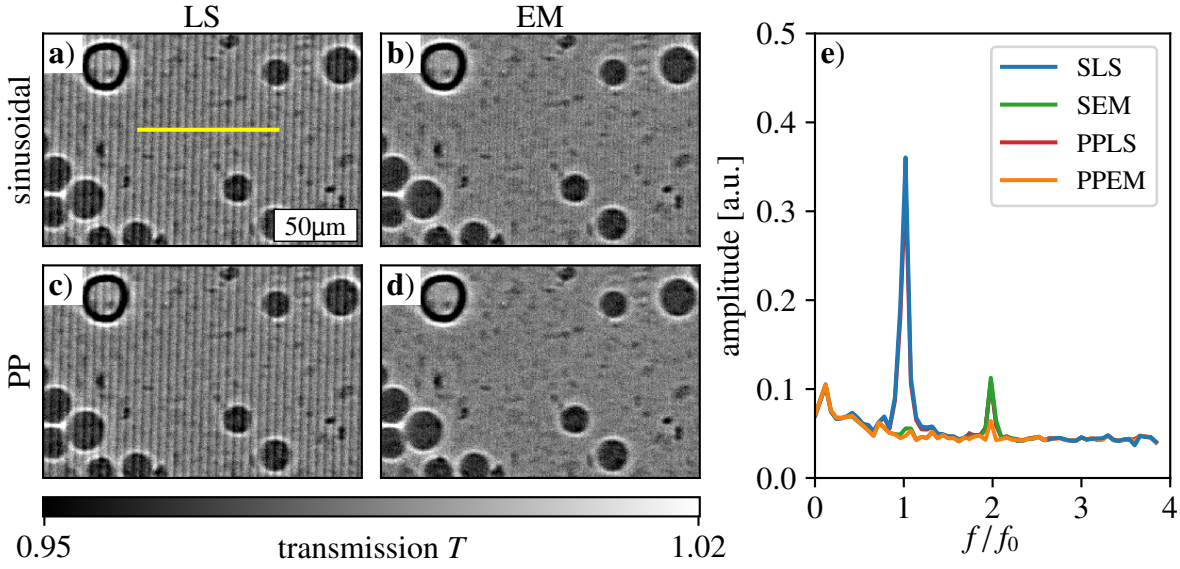

Figure B.5: Processed transmission images for **a)** sinusoidal least square (SLS), **b)** sinusoidal expectation maximization (SEM), **c)** periodic polynomial least square (PPLS), and **d)** periodic polynomial expectation maximization (PPEM) from the single grating X-ray interferometer. **e)** Fourier spectra for the respective processing schemes averaged from 50 pixel rows next to the yellow line in **a)**.

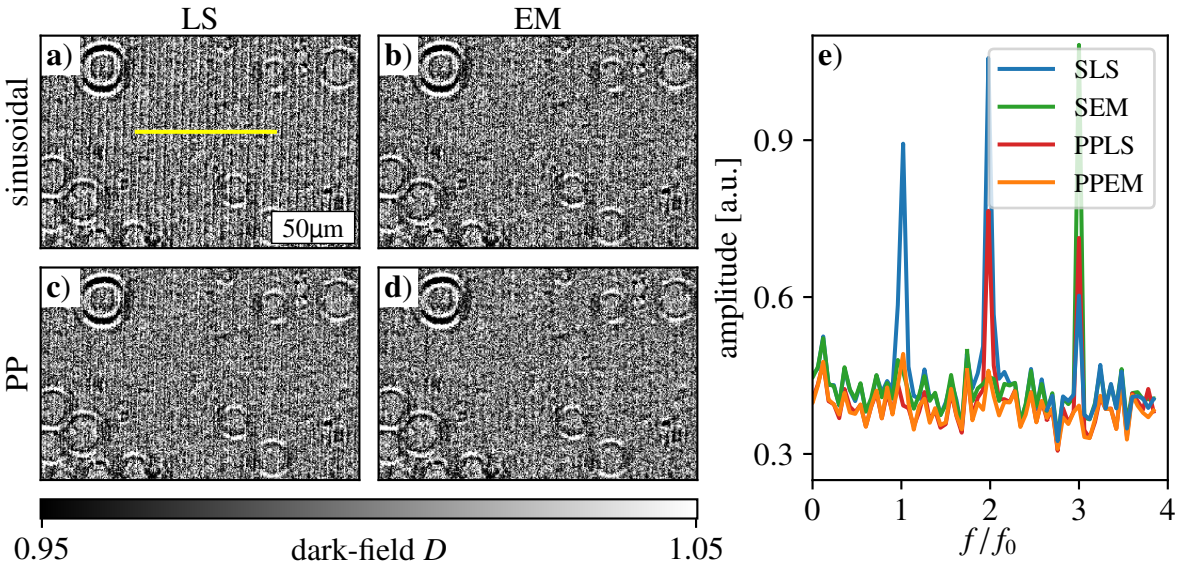

Figure B.6: Processed dark-field contrast images for **a)** sinusoidal least square (SLS), **b)** sinusoidal expectation maximization (SEM), **c)** periodic polynomial least square (PPLS), and **d)** periodic polynomial expectation maximization (PPEM) from the single grating X-ray interferometer. **e)** Fourier spectra for the respective processing schemes averaged from 50 pixel rows next to the yellow line in **a)**.

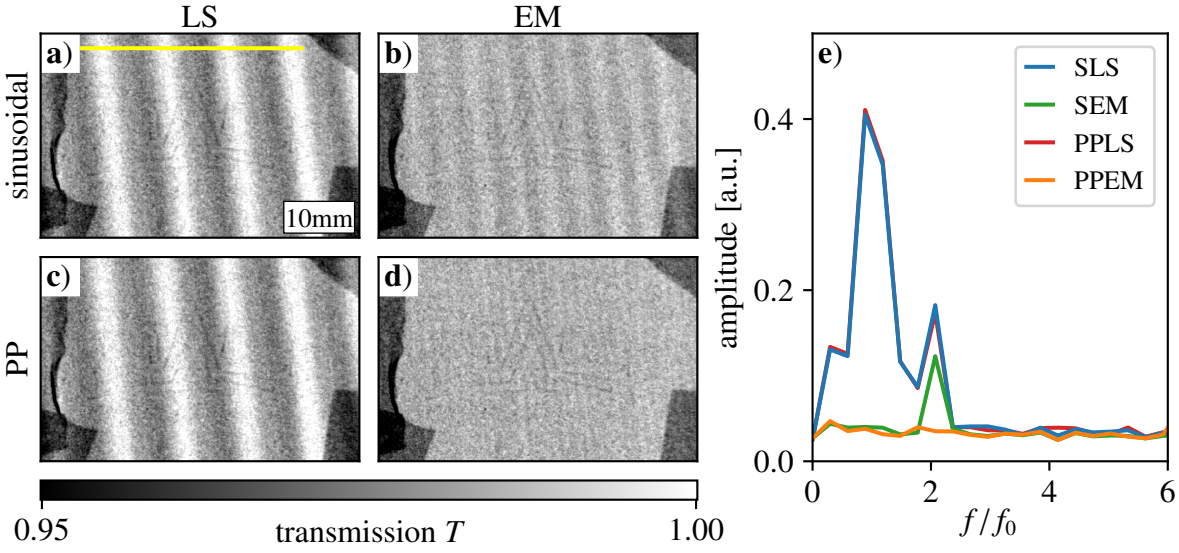

Figure B.7: Processed transmission images for **a)** sinusoidal least square (SLS), **b)** sinusoidal expectation maximization (SEM), **c)** periodic polynomial least square (PPLS), and **d)** periodic polynomial expectation maximization (PPEM) for the dataset measured at the Antares neutron beamline. **e)** Fourier spectra for the four algorithms averaged about 60 pixel lines along the yellow line in **a)**.

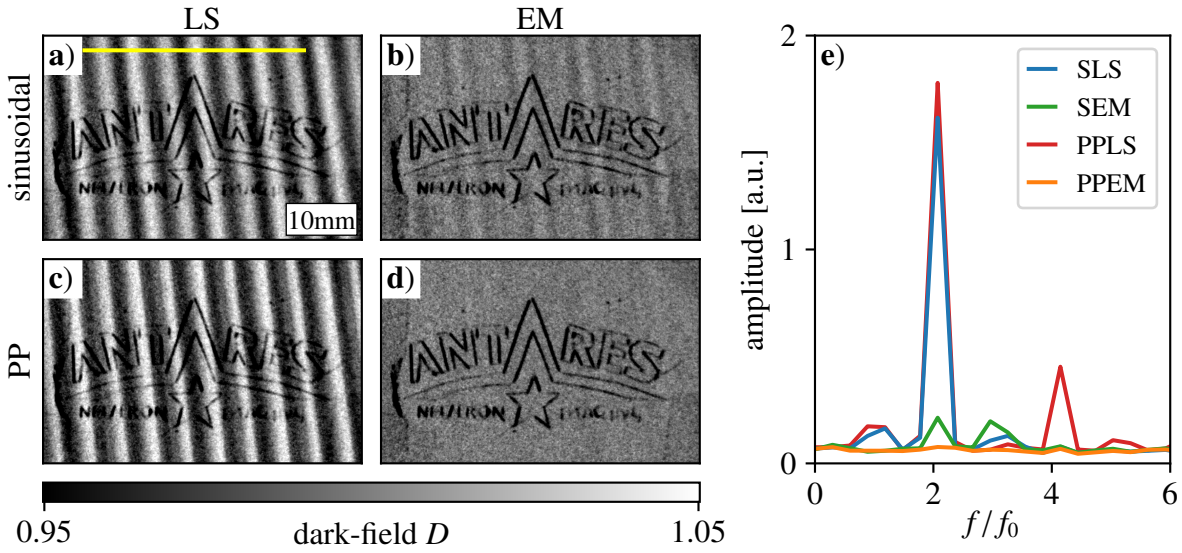

Figure B.8: Processed dark-field contrast images for **a)** sinusoidal least square (SLS), **b)** sinusoidal expectation maximization (SEM), **c)** periodic polynomial least square (PPLS), and **d)** periodic polynomial expectation maximization (PPEM) for the dataset measured at the Antares neutron beamline. **e)** Fourier spectra for the four algorithms averaged about 60 pixel lines along the yellow line in **a)**.

Bibliography

[Achenbach, 2003] Achenbach, S., Pantenburg, F. & Mohr, J. Numerical simulation of thermal distortions in deep and ultra deep X-ray lithography. *Microsystem Technologies* **9,** 220–224 (2003) (Cited on page 28).

[AlsNielsen, 2011] Als-Nielsen, J. *Elements of Modern X-ray Physics* 2nd ed. (John Wiley and Sons, 2011) (Cited on pages 5, 7–10, 13–15).

[Andrejewski, 2021] Andrejewski, J. K. L. *Human-sized X-ray Dark-field Imaging* Dissertation (Technical University of Munich, München, 2021) (Cited on pages 5, 15).

[Attwood, 1999] Attwood, D. *Soft X-rays and extreme ultraviolet radiation: Principles and Applications* (Cambridge University Press, 1999) (Cited on pages 5, 13, 14, 16, 68).

[Bech, 2009] Bech, M. *X-ray imaging with a grating interferometer* PhD thesis (University of Copenhagen, 2009) (Cited on page 20).

[Berujon, 2012] Berujon, S., Wang, H. & Sawhney, K. X-ray multimodal imaging using a random-phase object. *Physical Review A* **86,** 063813 (2012) (Cited on page 17).

[Bonse, 1965] Bonse, U. & Hart, M. An X-Ray Interferometer. *Applied Physics Letters* **6,** 155–156 (1965) (Cited on pages 1, 17).

[Cerrito, 2017] Cerrito, L. *Radiation and Detectors* (Springer, 2017) (Cited on page 5).

[Chabior, 2011] Chabior, M. *Contributions to the characterization of grating-based x-ray phase-contrast imaging* PhD thesis (Technische Universität Dresden, 2011) (Cited on pages 19–21, 89).

[Chabior, 2012] Chabior, M., Schuster, M., Goldammer, M., Schroer, C. & Pfeiffer, F. Influence of the grating profiles on the image quality in grating-based x-ray imaging. *Nuclear Instruments and Methods in Physics Research Section A: Accelerators, Spectrometers, Detectors and Associated Equipment* **683,** 71–77 (2012) (Cited on pages 23, 87, 89).

[Chapman, 1997] Chapman, D. *et al.* Diffraction enhanced x-ray imaging. *Physics in Medicine and Biology* **42,** 2015–2025 (1997) (Cited on page 17).

[Cloetens, 1996] Cloetens, P., Barrett, R., Baruchel, J., Guigay, J.-P. & Schlenker, M. Phase objects in synchrotron radiation hard x-ray imaging. *Journal of Physics D: Applied Physics* **29,** 133–146 (1996) (Cited on page 17).

[David, 2007] David, C. *et al.* Fabrication of diffraction gratings for hard X-ray phase contrast imaging. *Microelectronic Engineering* **84.** Proceedings of the 32nd International Conference on Micro- and Nano-Engineering, 1172–1177 (2007) (Cited on pages 2, 34–37).

[Davis, 1995] Davis, T. J., Gao, D., Gureyev, T. E., Stevenson, A. W. & Wilkins, S. W. Phase-contrast imaging of weakly absorbing materials using hard X-rays. *Nature* **373,** 595–598 (1995) (Cited on pages 16, 17).

[De Marco, 2018] De Marco, F. *et al.* Analysis and correction of bias induced by phase stepping jitter in grating-based X-ray phase-contrast imaging. *Optics Express* **26,** 12707–12722 (2018) (Cited on page 25).

[De Marco, 2021] De Marco, F. *Image reconstruction, pre-clinical studies, and signal formation investigations at a dark-field chest radiography setup* PhD thesis (Technical University of Munich, 2021) (Cited on page 19).

[Donath, 2009] Donath, T. *et al.* Inverse geometry for grating-based x-ray phase-contrast imaging. *Journal of Applied Physics* **106,** 054703 (2009) (Cited on pages 22, 58, 109).

[Du, 2011] Du, Y., Liu, X., Lei, Y., Guo, J. & Niu, H. Non-absorption grating approach for X-ray phase contrast imaging. *Optics Express* **19,** 22669–22674 (2011) (Cited on pages 40, 41).

[Finnegan, 2019] Finnegan, P. S., Hollowell, A. E., Arrington, C. L. & Dagel, A. L. High aspect ratio anisotropic silicon etching for x-ray phase contrast imaging grating fabrication. *Materials Science in Semiconductor Processing* **92.** Material processing of optical devices and their applications, 80–85 (2019) (Cited on pages 2, 34).

[Goettert, 2012] Goettert, J., Lemke, S., Rudolph, I., Seliger, T. & Loechel, B. *Soft X-Ray Lithography for High-Aspect Ratio Sub-Micrometer Structures* in *Nanotech Conference* (2012) (Cited on page 2).

[Griffiths, 2004] Griffiths, S. K. Fundamental limitations of LIGA x-ray lithography: Sidewall offset, slope and minimum feature size. *Journal of Micromechanics and Microengineering* **14,** 999–1011 (2004) (Cited on page 69).

[Gross, 2014] Gross, R. & Marx, A. *Festkörperphysik* (De Gruyter Oldenbourg, 2014) (Cited on page 47).

[Grünzweig, 2008] Grünzweig, C. *et al.* Neutron Decoherence Imaging for Visualizing Bulk Magnetic Domain Structures. *Physical Review Letters* **101,** 025504 (2008) (Cited on page 1).

[Gustschin, 2016] Gustschin, A. *Alternative Absorption Grating Fabrication Methods for Talbot-Lau Interferometry* MA thesis (Technical University of Munich, 2016) (Cited on pages 6, 24, 39, 48, 49, 67, 68).

[Gustschin, 2018] Gustschin, A., Neuwirth, T., Backs, A., Schulz, M. & Pfeiffer, F. Fabrication of gadolinium particle-based absorption gratings for neutron grating interferometry. *Review of Scientific Instruments* **89,** 103702 (2018) (Cited on pages 2, 39, 49, 103).

[Gustschin, 2019] Gustschin, N. *et al.* Quality and parameter control of X-ray absorption gratings by angular X-ray transmission. *Optics Express* **27,** 15943–15955 (2019) (Cited on pages 44, 58, 64).

[Han, 2014] Han, H., Huang, Z. & Lee, W. Metal-assisted chemical etching of silicon and nanotechnology applications. *Nano Today* **9,** 271–304 (2014) (Cited on page 35).

[Hashimoto, 2020] Hashimoto, K., Takano, H. & Momose, A. Improved reconstruction method for phase stepping data with stepping errors and dose fluctuations. *Optics Express* **28,** 16363 (2020) (Cited on page 25).

[Hellbach, 2016] Hellbach, K. *et al.* Facilitated Diagnosis of Pneumothoraces in Newborn Mice Using X-ray Dark-Field Radiography. *Investigative radiology* **51,** 597–601 (2016) (Cited on page 2).

[Hellbach, 2018] Hellbach, K. *et al.* X-Ray Dark-field Imaging to Depict Acute Lung Inflammation in Mice. *Scientific Reports* **8,** 2096 (2018) (Cited on page 2).

[Hojo, 2019] Hojo, D., Kamezawa, C., Hyodo, K. & Yashiro, W. Fabrication of X-ray absorption grating using an ultracentrifuge machine. *Japanese Journal of Applied Physics* **58,** 088003 (2019) (Cited on pages 2, 40, 47, 49, 64, 65).

[Hollowell, 2019] Hollowell, A. E. *et al.* Double sided grating fabrication for high energy X-ray phase contrast imaging. *Materials Science in Semiconductor Processing* **92.** Material processing of optical devices and their applications, 86–90 (2019) (Cited on pages 2, 34).

[Ingal, 1995] Ingal, V. N. & Beliaevskaya, E. A. X-ray plane-wave topography observation of the phase contrast from a non-crystalline object. *Journal of Physics D: Applied Physics* **28,** 2314–2317 (1995) (Cited on pages 1, 17).

[Jefimovs, 2021] Jefimovs, K. *et al.* Fabrication of X-ray Gratings for Interferometric Imaging by Conformal Seedless Gold Electroplating. *Micromachines* **12** (2021) (Cited on pages 2, 36, 37).

[Josell, 2020] Josell, D. *et al.* Pushing the Limits of Bottom-Up Gold Filling for X-ray Grating Interferometry. *Journal of The Electrochemical Society* **167,** 132504 (2020) (Cited on page 2).

[Kaeppler, 2017] Kaeppler, S. *et al.* Improved reconstruction of phase-stepping data for Talbot-Lau x-ray imaging. *Journal of Medical Imaging* **4,** 1–13 (2017) (Cited on page 25).

[Kagias, 2019] Kagias, M. *et al.* Fabrication of Au gratings by seedless electroplating for X-ray grating interferometry. *Materials Science in Semiconductor Processing* **92.** Material processing of optical devices and their applications, 73–79 (2019) (Cited on pages 36, 37).

[Kenntner, 2012] Kenntner, J. *et al.* Fabrication and characterization of analyzer gratings with high aspect ratios for phase contrast imaging using a Talbot interferometer. *AIP Conference Proceedings* **1437,** 89–93 (2012) (Cited on page 68).

[Kenntner, 2013] Kenntner, J. *Herstellung von Gitterstrukturen mit Aspektverhältnis 100 für die Phasenkontrastbildgebung in einem Talbot-Interferometer* PhD thesis (2013) (Cited on page 33).

[Kim, 2013] Kim, J. *et al.* Fabrication and characterization of the source grating for visibility improvement of neutron phase imaging with gratings. *Review of Scientific Instruments* **84,** 063705 (2013) (Cited on pages 39, 48).

[Kim, 2020] Kim, Y. *et al.* Neutron grating interferometer with an analyzer grating based on a light blocker. *Optics Express* **28,** 23284–23293 (2020) (Cited on pages 40, 41).

[Kleimann, 2001] Kleimann, P., Linnros, J., Fröjdh, C. & Petersson, C. An X-ray imaging pixel detector based on scintillator filled pores in a silicon matrix. *Nuclear Instruments and Methods in Physics Research Section A: Accelerators, Spectrometers, Detectors and Associated Equipment* **460.** Proc. 1st Int. Workshop on Radiation Imaging Detectors, 15–19 (2001) (Cited on page 41).

[Knoops, 2010] Knoops, H. C. M., Langereis, E., van de Sanden, M. C. M. & Kessels, W. M. M. Conformality of Plasma-Assisted ALD: Physical Processes and Modeling. *Journal of The Electrochemical Society* **157,** G241 (2010) (Cited on page 37).

[Koch, 2015] Koch, F. J. *et al.* Note: Gratings on low absorbing substrates for x-ray phase contrast imaging. *Review of Scientific Instruments* **86,** 126114 (2015) (Cited on pages 28, 33, 68).

[Kottler, 2007] Kottler, C., Pfeiffer, F., Bunk, O., Grünzweig, C. & David, C. Grating interferometer based scanning setup for hard x-ray phase contrast imaging. *Review of Scientific Instruments* **78,** 043710 (2007) (Cited on page 34).

[Lei, 2014] Lei, Y. *et al.* Fabrication of x-ray absorption gratings via microcasting for grating-based phase contrast imaging. *Journal of Micromechanics and Microengineering* **24,** 015007 (2014) (Cited on pages 2, 35, 39).

[Lei, 2016] Lei, Y., Liu, X., Li, J., Guo, J. & Niu, H. Improvement of filling bismuth for x-ray absorption gratings through the enhancement of wettability. *Journal of Micromechanics and Microengineering* **26,** 065011 (2016) (Cited on pages 2, 35, 39).

[Lei, 2019a] Lei, Y. *et al.* Tungsten nanoparticles-based x-ray absorption gratings for cascaded Talbot–Lau interferometers. *Journal of Micromechanics and Microengineering* **29,** 115008 (2019) (Cited on pages 2, 40, 49, 65).

[Lei, 2019b] Lei, Y. *et al.* An 8-inch absorption grating used in cascaded Talbot-Lau interferometers for X-ray phase-contrast imaging. *Applied Physics Express* **12,** 126504 (2019) (Cited on pages 2, 40, 49, 64, 65).

[Linnros, 2006] Linnros, J., Badel, X. & Kleimann, P. Macro pore and pillar array formation in silicon by electrochemical etching. *Physica Scripta* **T126,** 72–76 (2006) (Cited on page 35).

[Marschner, 2016] Marschner, M. *et al.* Helical X-ray phase-contrast computed tomography without phase stepping. *Scientific Reports* **6,** 23953 (2016) (Cited on page 25).

[Meiser, 2016] Meiser, J. *et al.* Increasing the field of view in grating based X-ray phase contrast imaging using stitched gratings. *Journal of X-Ray Science and Technology* **24.** 3, 379–388 (2016) (Cited on pages 33, 34).

[Meyer, 2010] Meyer, P., Schulz, J. & Saile, V. in *Micro-Manufacturing Engineering and Technology* 202–220 (William Andrew, 2010) (Cited on pages 2, 33).

[Meyer, 2014] Meyer, P. & Pantenburg, F.-J. A Monte Carlo study of the primary absorbed energy redistribution in X-ray lithography. *Microsystem Technology* **20,** 1881–1889 (2014) (Cited on page 68).

[Mohr, 2012a] Mohr, J. *et al.* High aspect ratio gratings for X-ray phase contrast imaging. *AIP Conference Proceedings* **1466,** 41–50 (2012) (Cited on page 68).

[Mohr, 2012b] Mohr, J. *et al.* RESIST STRUCTURE FOR PRODUCING AN X-RAY OPTICAL GRATING STRUCTURE. WO 2012/055495 AI (2012) (Cited on page 33).

[Momose, 2003] Momose, A. *et al.* Demonstration of X-Ray Talbot Interferometry. *Japanese Journal of Applied Physics* **42,** L866–L868 (2003) (Cited on pages 1, 17, 20).

[Morgan, 2011] Morgan, K. S., Paganin, D. M. & Siu, K. K. W. Quantitative single-exposure x-ray phase contrast imaging using a single attenuation grid. *Optics Express* **19,** 19781–19789 (2011) (Cited on page 17).

[Morgan, 2012] Morgan, K. S., Paganin, D. M. & Siu, K. K. W. X-ray phase imaging with a paper analyzer. *Applied Physics Letters* **100,** 124102 (2012) (Cited on page 17).

[Morimoto, 2014] Morimoto, N. *et al.* X-ray phase contrast imaging by compact Talbot–Lau interferometer with a single transmission grating. *Optics Letters* **39,** 4297–4300 (2014) (Cited on pages 40, 41).

[Munro, 2012] Munro, P. R., Ignatyev, K., Speller, R. D. & Olivo, A. Phase and absorption retrieval using incoherent X-ray sources. *Proceedings of the National Academy of Sciences of the United States of America* **109,** 13922–13927 (2012) (Cited on pages 1, 87, 89).

[Neuwirth, 2020] Neuwirth, T. *et al.* A high visibility Talbot-Lau neutron grating interferometer to investigate stress-induced magnetic degradation in electrical steel. *Scientific Reports* **10,** 1764 (2020) (Cited on page 103).

[Noda, 2008] Noda, D. *et al.* Fabrication of large area diffraction grating using LIGA process. *Microsystem Technologies* **14,** 1311–1315 (2008) (Cited on page 2).

[NEA, 2012] Nuclear Energy Agency. *PENELOPE 2011: A code system for Monte Carlo simulation of electron and photon transport* (OECD Publishing, 2012) (Cited on page 6).

[Olivo, 2001] Olivo, A. *et al.* An innovative digital imaging set-up allowing a low-dose approach to phase contrast applications in the medical field. *Medical Physics* **28,** 1610–1619 (2001) (Cited on page 17).

[Pantenburg, 1995] Pantenburg, F. & Mohr, J. Influence of secondary effects on the structure quality in deep X-ray lithography. *Nuclear Instruments and Methods in Physics Research Section B: Beam Interactions with Materials and Atoms* **97,** 551–556 (1995) (Cited on page 69).

[Pelzer, 2015] Pelzer, G. *et al.* Reconstruction method for grating-based x-ray phase-contrast images without knowledge of the grating positions. *Journal of Instrumentation* **10,** P12017–P12017 (2015) (Cited on page 25).

[Pfeiffer, 2006a] Pfeiffer, F., Weitkamp, T., Bunk, O. & David, C. Phase retrieval and differential phase-contrast imaging with low-brilliance X-ray sources. *Nature Physics* **2,** 258–261 (2006) (Cited on pages 1, 21).

[Pfeiffer, 2006b] Pfeiffer, F. *et al.* Neutron Phase Imaging and Tomography. *Physical Review Letters* **96,** 215505 (2006) (Cited on page 1).

[Pfeiffer, 2008] Pfeiffer, F. *et al.* Hard-X-ray dark-field imaging using a grating interferometer. *Nature Materials* **7,** 134–137 (2008) (Cited on pages 2, 23).

[Pinzek, 2018] Pinzek, S. *Towards Low Cost and Large Area Grating Fabrication for Grating-based X-Ray Imaging* MA thesis (Technical University of Munich, 2018) (Cited on pages 12, 32, 39, 47, 49, 50, 68, 70).

[Pinzek, 2021a] Pinzek, S. *et al.* Fabrication of x-ray absorption gratings via deep x-ray lithography using a conventional x-ray tube. *Journal of Micro/-Nanopatterning, Materials, and Metrology* **20,** 1–12 (2021) (Cited on pages 67, 69–72, 81–83).

[Pinzek, 2021b] Pinzek, S. *et al.* Signal Retrieval from Non-Sinusoidal Intensity Modulations in X-ray and Neutron Interferometry Using Piecewise-Defined Polynomial Function. *Journal of Imaging* **7** (2021) (Cited on pages 87, 88, 91, 96, 98, 99, 101–103).

[Pinzek, 2022] Pinzek, S., Gustschin, A., Gustschin, N., Viermetz, M. & Pfeiffer, F. Fabrication of X-ray absorption gratings by centrifugal deposition of bimodal tungsten particles in high aspect ratio silicon templates. *Scientific Reports* **12,** 5405 (2022) (Cited on pages 47, 50, 53, 56–59, 62, 63).

[Podgorsak, 2016] Podgorsak, E. *Radiation Physics for Medical Physicists* 3rd ed. (Springer, 2016) (Cited on pages 13, 14).

[Revol, 2010] Revol, V., Kottler, C., Kaufmann, R., Straumann, U. & Urban, C. Noise analysis of grating-based x-ray differential phase contrast imaging. *Review of Scientific Instruments* **81,** 073709 (2010) (Cited on page 25).

[Reznikova, 2008] Reznikova, E., Mohr, J., Boerner, M., Nazmov, V. & Jakobs, P. J. Soft X-ray lithography of high aspect ratio SU8 submicron structures. *Microsystem Technologies* **14,** 1683–1688 (2008) (Cited on page 2).

[Richter, 2022] Richter, M. *et al.* Investigation on the mechanical interface stability of curved high aspect ratio x-ray gratings made by deep x-ray lithography. *Journal of Micro/Nanopatterning, Materials, and Metrology* **21,** 1–11 (2022) (Cited on page 28).

[Rinnerbauer, 2013] Rinnerbauer, V. *et al.* Large-area fabrication of high aspect ratio tantalum photonic crystals for high-temperature selective emitters. *Journal of Vacuum Science & Technology B* **31,** 011802 (2013) (Cited on page 31).

[Röntgen, 1895] Röntgen, W. C. Ueber eine neue Art von Strahlen. Vorläufige Mittheilung. *Sitzungs-Berichte der Physikalisch-medicinischen Gesellschaft zu Würzburg* (1895) (Cited on page 1).

[Romano, 2017a] Romano, L. *et al.* High aspect ratio metal microcasting by hot embossing for X-ray optics fabrication. *Microelectronic Engineering* **176.** Micro- and Nano-Fabrication, 6–10 (2017) (Cited on pages 2, 39).

[Romano, 2017b] Romano, L., Vila-Comamala, J., Schift, H., Stampanoni, M. & Jefimovs, K. Hot embossing of Au- and Pb-based alloys for x-ray grating fabrication. *Journal of Vacuum Science & Technology B* **35,** 06G302 (2017) (Cited on pages 2, 34, 35, 38, 39).

[Romano, 2020a] Romano, L. *et al.* Metal assisted chemical etching of silicon in the gas phase: a nanofabrication platform for X-ray optics. *Nanoscale Horizons* **5,** 869–879 (2020) (Cited on pages 2, 35).

[Romano, 2020b] Romano, L., Vila-Comamala, J., Jefimovs, K. & Stampanoni, M. High-Aspect-Ratio Grating Microfabrication by Platinum-Assisted Chemical Etching and Gold Electroplating. *Advanced Engineering Materials* **22,** 2000258 (2020) (Cited on pages 2, 35).

[Sauter, 2019] Sauter, A. P. *et al.* Optimization of tube voltage in X-ray dark-field chest radiography. *Scientific Reports* **9,** 8699 (2019) (Cited on page 49).

[Scherer, 2017] Scherer, K. *et al.* X-ray Dark-field Radiography - In-Vivo Diagnosis of Lung Cancer in Mice. *Scientific Reports* **7,** 402 (2017) (Cited on page 2).

[Schleede, 2012] Schleede, S. *et al.* Emphysema diagnosis using X-ray dark-field imaging at a laser-driven compact synchrotron light source. *Proceedings of the National Academy of Sciences* **109,** 17880–17885 (2012) (Cited on page 2).

[Schoonjans, 2011] Schoonjans, T. *et al.* The xraylib library for X-ray–matter interactions. Recent developments. *Spectrochimica Acta Part B: Atomic Spectroscopy* **66,** 776–784 (2011) (Cited on pages 12, 29).

[Schröter, 2017a] Schröter, T. J. *et al.* Large field-of-view tiled grating structures for X-ray phase-contrast imaging. *Review of Scientific Instruments* **88,** 015104 (2017) (Cited on page 33).

[Schröter, 2017b] Schröter, T. J. *et al.* Large-area full field x-ray differential phase-contrast imaging using 2D tiled gratings. *Journal of Physics D: Applied Physics* **50,** 225401 (2017) (Cited on page 34).

[Schröter, 2017c] Schröter, T. *et al.* Large area gratings by x-ray LIGA dynamic exposure for x-ray phase-contrast imaging. *Journal of Micro/Nanolithography, MEMS, and MOEMS* **16,** 013501 (2017) (Cited on pages 34, 68).

[Schulz, 2015] Schulz, M. & Schillinger, B. ANTARES: Cold neutron radiography and tomography facility. *Journal of large-scale research facilities JLSRF* **1,** A17 (2015) (Cited on page 102).

[Schüttler, 2016] Schüttler, M. *et al.* Height control for small periodic structures using x-ray radiography. *Measurement Science and Technology* **27** (2016) (Cited on page 45).

[Seibert, 2005] Seibert, J. A. & Boone, J. M. X-Ray Imaging Physics for Nuclear Medicine Technologists. Part 2: X-Ray Interactions and Image Formation. *Journal of Nuclear Medicine Technology* **33,** 3–18 (2005) (Cited on page 11).

[Seifert, 2016] Seifert, M. *et al.* Optimisation of image reconstruction for phase-contrast x-ray Talbot–Lau imaging with regard to mechanical robustness. *Physics in Medicine and Biology* **61,** 6441–6464 (2016) (Cited on page 25).

[Shi, 2020] Shi, Z., Jefimovs, K., Romano, L. & Stampanoni, M. Towards the fabrication of high-aspect-ratio silicon gratings by deep reactive ion etching. *Micromachines* **11,** 1–13 (2020) (Cited on pages 2, 34).

[Shi, 2022] Shi, Z., Jefimovs, K., La Magna, A., Stampanoni, M. & Romano, L. High aspect ratio tilted gratings through local electric field modulation in plasma etching. *Applied Surface Science* **588,** 152938 (2022) (Cited on page 34).

[Smith, 1980] Smith, H. I. & Flanders, D. C. X-ray lithography – A review and assessment of future applications. *Journal of Vacuum Science and Technology* **17,** 533–535 (1980) (Cited on page 67).

[Snigirev, 1995] Snigirev, A., Snigireva, I., Kohn, V., Kuznetsov, S. & Schelokov, I. On the possibilities of x-ray phase contrast microimaging by coherent high-energy synchrotron radiation. *Review of Scientific Instruments* **66,** 5486–5492 (1995) (Cited on pages 1, 17).

[Song, 2008] Song, C., Wang, P. & Makse, H. A. A phase diagram for jammed matter. *Nature* **453,** 629–632 (2008) (Cited on page 47).

[Suleski, 1997] Suleski, T. J. Generation of Lohmann images from binary-phase Talbot array illuminators. *Applied Optics* **36,** 4686–4691 (1997) (Cited on pages 18, 89).

[Vargas, 2011] Vargas, J., Quiroga, J. A. & Belenguer, T. Phase-shifting interferometry based on principal component analysis. *Optics Letters* **36,** 1326–1328 (2011) (Cited on page 25).

[Viermetz, 2022] Viermetz, M. *et al.* Dark-field computed tomography reaches the human scale. *Proceedings of the National Academy of Sciences* **119.** eprint: `https://www.pnas.org/content/119/8/e2118799119.full.pdf` (2022) (Cited on pages 55, 61).

[VilaComamala, 2018] Vila-Comamala, J. *et al.* Towards sub-micrometer high aspect ratio X-ray gratings by atomic layer deposition of iridium. *Microelectronic Engineering* **192,** 19–24 (2018) (Cited on pages 2, 31, 34, 37, 38).

[Wang, 2007] Wang, Z. & Han, B. Advanced iterative algorithm for randomly phase-shifted interferograms with intra- and inter-frame intensity variations. *Optics and Lasers in Engineering* **45.** Phase Measurement Techniques and their applications, 274–280 (2007) (Cited on page 25).

[Weitkamp, 2005] Weitkamp, T. *et al.* X-ray phase imaging with a grating interferometer. *Optics Express* **13,** 6296–6304 (2005) (Cited on pages 1, 17, 95).

[Weitkamp, 2006] Weitkamp, T., David, C., Kottler, C., Bunk, O. & Pfeiffer, F. *Tomography with grating interferometers at low-brilliance sources* in *Developments in X-Ray Tomography V* (SPIE, 2006), 63180S (Cited on pages 17, 22).

[Wen, 2010] Wen, H. H., Bennett, E. E., Kopace, R., Stein, A. F. & Pai, V. Single-shot x-ray differential phase-contrast and diffraction imaging using two-dimensional transmission gratings. *Optics Letters* **35,** 1932–1934 (2010) (Cited on page 17).

[White, 1977] White, D. R. An analysis of the Z-dependence of photon and electron interactions. *Physics in Medicine and Biology* **22,** 219–228 (1977) (Cited on pages 12, 13).

[Wilde, 2016] Wilde, F. *et al.* Micro-CT at the imaging beamline P05 at PETRA III. *AIP Conference Proceedings* **1741,** 030035 (2016) (Cited on page 101).

[Wilkins, 1996] Wilkins, S. W., Gureyev, T. E., Gao, D., Pogany, A. & Stevenson, A. W. Phase-contrast imaging using polychromatic hard X-rays. *Nature* **384,** 356–358 (1996) (Cited on pages 1, 17).

[Willer, 2021] Willer, K. *et al.* X-ray dark-field chest imaging for detection and quantification of emphysema in patients with chronic obstructive pulmonary disease: a diagnostic accuracy study. *The Lancet Digital Health* **3,** e733–e744 (2021) (Cited on pages 2, 110).

[Willmott, 2011] Willmott, P. *An Introduction to Synchrotron Radiation: Techniques and Applications* (John Wiley and Sons, 2011) (Cited on pages 5, 12, 14–16).

[Yaroshenko, 2014] Yaroshenko, A. *et al.* Non-binary phase gratings for x-ray imaging with a compact Talbot interferometer. *Optics Express* **22,** 547 (2014) (Cited on page 87).

[Yaroshenko, 2015] Yaroshenko, A. *et al.* Improved In vivo Assessment of Pulmonary Fibrosis in Mice using X-Ray Dark-Field Radiography. *Scientific Reports* **5,** 17492 (2015) (Cited on page 2).

[Ye, 2018] Ye, X., Li, Y., Ai, Y. & Nie, Y. Novel powder packing theory with bimodal particle size distribution-application in superalloy. *Advanced Powder Technology* **29,** 2280–2287 (2018) (Cited on page 48).

[Zan, 2021] Zan, G. *et al.* High-resolution multicontrast tomography with an X-ray microarray anode–structured target source. *Proceedings of the National Academy of Sciences* **118,** e2103126118 (2021) (Cited on page 41).

[Zanette, 2014] Zanette, I. *et al.* Speckle-Based X-Ray Phase-Contrast and Dark-Field Imaging with a Laboratory Source. *Physical Review Letters* **112,** 253903 (2014) (Cited on page 1).

[Zhou, 1995] Zhou, C. & Liu, L. Simple equations for the calculation of a multilevel phase grating for Talbot array illumination. *Optics Communications* **115,** 40–44 (1995) (Cited on page 18).

List of peer-reviewed Publications

Simon Pinzek, Thomas Beckenbach, Manuel Viermetz, Pascal Meyer, Alex Gustschin, Jana Andrejewski, Nikolai Gustschin, Julia Herzen, Joachim Schulz, and Franz Pfeiffer.
Fabrication of x-ray absorption gratings via deep x-ray lithography using a conventional x-ray tube.
Journal of Micro/Nanopatterning, Materials, and Metrology 20(4), 043801 (4 October 2021)

Simon Pinzek, Alex Gustschin, Tobias Neuwirth, Alexander Backs, Michael Schulz, Julia Herzen, and Franz Pfeiffer.
Signal Retrieval from Non-Sinusoidal Intensity Modulations in X-ray and Neutron Interferometry Using Piecewise-Defined Polynomial Function.
Journal of Imaging 7(10), 209 (11 October 2021)

Simon Pinzek, Alex Gustschin, Nikolai Gustschin, Manuel Viermetz, and Franz Pfeiffer.
Fabrication of X-ray absorption gratings by centrifugal deposition of bimodal tungsten particles in high aspect ratio silicon templates.
Scientific Reports 12, 5405 (30 March 2022)

Acknowledgments

During my time at the Chair of Biomedical Physics and for the course of my PhD thesis I received support, assistance, and encouragement from a variety of people. Without them this thesis would not have been possible.

Foremost, I want to thank my doctorate supervisor, Prof. Dr. Franz Pfeiffer, for giving me the opportunity to graduate under his tutelage. Thank you for setting up a framework in which I had all the equipment and support I needed during this time.

I am very grateful to Alex Gustschin for his support and our numerous discussions. Thank you, for sharing your knowledge and helping me with all kinds of problems during my work.

Special thanks go to Dr. Manuel Viermetz for his help with the Belichterbox and his insightful advice especially during the deep X-ray lithography project.

Further, I like to thank Dr. Joachim Schulz and Tom Beckenbach from Microworks GmbH for their support with coated wafers and the substrate development. Thank you Dr. Pascal Meyer from KIT for your assistance in the deep X-ray lithography project.

Thank you, Niko Gustschin, for your help and discussions about the grating characterization.

I also want to thank Dr. Madleen Busse and Dr. Klaus Achterhold. You were always a great help when it came to solving problems in the chemistry and X-ray lab.

A big thank you goes to Alex Gustschin, Dr. Manuel Viermetz, and Dr. Jana Andrejewski for proof-reading this thesis.

Many thanks go to the IT-crew, Dr. Martin Dierolf and Clemens Schmidt, for your support with IT problems.

A big thank you goes to Alen Begic and Niko Gustschin for your help with constructing customized equipment.

I also want to thank Nelly de Leiris and Dr. Klaus Achterhold for their assistance in all the administrative and bureaucratic tasks.

Further, I like to thank all members of the Chair of Biomedical Physics for the great working atmosphere and fun times during breaks, at the seminar days, and other activities.

Finally, I would like to thank my family and friends for their everlasting support throughout the years.